Dimensional tolerance analysis and quality assurance of a particle tracker's support structure

Janne Huotari

School of Engineering

Thesis submitted for examination for the degree of Master of Science in Technology.
Espoo September 7, 2018

Thesis supervisor:

Prof. Kari Tammi (Aalto University)

Thesis advisor:

M.Sc. (Eng.) Antti Onnela (CERN)

Aalto University
School of Engineering

Aalto University, P.O. BOX 11000, 00076
AALTO
www.aalto.fi

Abstract of master's thesis

Author Janne Huotari

Title of thesis Dimensional tolerance analysis and quality assurance of a particle tracker's sub-detector

Master programme Mechanical engineering **Code** ENG25

Thesis supervisor Prof. Kari Tammi

Thesis advisor(s) M.Sc. (Eng.) Antti Onnela

Date 07.09.2018 **Number of pages** 93+6 **Language** English

Abstract

Particle detectors are some of the largest and most complicated devices ever built, that are used to study the smallest building blocks of our universe. Design and construction can take years and engineers and physicists have to guarantee that the detectors finally operate as required. The Large Hadron Collider (LHC) at CERN is being updated to operate at higher luminosities. Consequently, many of the detectors that study the collisions produced by the LHC are being upgraded. In this thesis, an abstracted feature based model is presented for allocating geometric tolerances for a novel support structure of the future tracking detector of the Compact Muon Solenoid (CMS) experiment. This new tracking detector will have a unique section where silicon sensors are mounted in different angular orientations, providing unparalleled track reconstruction efficiency while lowering costs tremendously. The tolerance analysis is based on the functional requirement of hermeticity in the CMS tracker: silicon sensors within each of the tracker's layers must overlap slightly so that particles cannot traverse a layer without hitting at least one active sensor surface. Imprecisions in the tracker's real construction geometry cause the sensors to deviate from their nominal positions. This may generate gaps through which particles can traverse without hitting a sensor. Because the CMS tracker is a first-time-right production, with limited or even no possibilities for corrections in the mechanical construction, the composed model of the tolerances is based on worst-case analysis.

The second part of this thesis is dedicated to quality assurance; the simulated geometric tolerances are utilized to develop accuracy requirements for dimensional measurements**.** Dimensional measurement plans are presented for the various assembly stages of the studied sub-detector. The chosen measurement methods utilize either a coordinate measurement machine (CMM) when the geometry and dimensions allow it, or photogrammetry. In case of photogrammetry, detailed descriptions are provided as where to position photogrammetric targets to achieve the required measurement accuracies.

As a result, it is shown that an abstracted feature based model is suitable for analyzing tolerances of the CMS trackers support structures. Such model can also be integrated into existing software at CERN, to allocate tolerances for other support structures. Additionally, comprehensive dimensional measurement plans have been developed for the quality assurance of the sub-detector.

Keywords CERN, CMS, Particle detector, Tracker, Tolerance analysis, Tolerance synthesis, Dimensional measurement, Photogrammetry, Sensitivity analysis

Aalto University
School of Engineering

Aalto University, P.O. BOX 11000, 00076
AALTO
www.aalto.fi

Diplomityön tiivistelmä

Tekijä Janne Huotari	
Työn nimi Hiukkasilmaisimen tukirakenteen toleranssianalyysi ja laadunvarmistus	
Koulutusohjelma Mechanical engineering	**Koodi** ENG25
Vastuuopettaja Prof. Kari Tammi	
Työn ohjaaja DI Antti Onnela	
Päivämäärä 07.09.2018 **Sivumäärä** 93+6	**Kieli** Englanti

Abstract

Hiukkasilmaisimet ovat yksiä suurimmista ja monimutkaisimmista laitteista joita on koskaan rakennettu. Niitä käytetään tutkimaan universumimme pienimpiä ja perustavanlaatuisimpia palasia. Hiukkasilmaisimien rakentaminen vie usein vuosia, ja niinpä niitä rakentavien insinöörien ja fyysikoiden tulee olla varmoja, että ne toimivat ennalta määritetyllä tavalla valmistuttuaan. CERN:issä sijaitsevaa suurta hadronitörmäytintä valmistellaan uudistukseen, jonka jälkeen se toimii korkeammalla luminositeetillä. Tästä johtuen useat ilmaisimet jotka tutkivat törmäyttimen tuottamia törmäyksiä uudistetaan myös. Tässä työssä esitellään abstrakteihin piirteisiin perustuva malli, jonka avulla asetetaan toleransseja kompaktin myonisolenoidin uuden jäljittimen tukirakenteisiin. Mallin toleranssianalyysi pohjautuu jäljittimen hermeettisyyteen liittyvään toiminnalliseen vaatimukseen: jäljittimen kerroksissa olevien piisensoreiden tulee limittyä hieman päällekkäin, jotta partikkelit eivät pääse kulkeutumaan kerroksen läpi osumatta ainakin yhden piisensorin aktiiviseen pintaan. Tukirakenteen toleranssit aiheuttavat näiden sensoreiden paikaan poikkeavuutta niiden nominaalisesta sijainnista, jolloin kerroksiin voi syntyä rakoja joista partikkelit pääsevät läpi. Koska uusi jäljitin rakennetaan vain kerran, toleranssianalyysimalli ratkaisee toleranssit pahimman mahdollisen skenaarion menetelmällä.

Työn toisessa osassa hyödynnetään laskettuja toleransseja määrittelemällä niiden perusteella tarkkuusvaatimukset tukirakenteen dimensionaaliselle mittaukselle. Dimensionaalisen mittauksen suunnitelmat esitellään jäljittimelle sen kokoamisen eri vaiheissa. Valitut mittaustavat käyttävät hyödyksi joko koordinaattimittauskonetta, tai fotogrammetriaa. Fotogrammetrian tapauksessa keskitytään fotogrammetristen maalien paikkoihin, jotta mittauksen tarkkuusvaatimukset toteutuisivat.

Työn tuloksena näytetään, että esitelty abstrakteihin piirteisiin perustuva malli soveltuu kompaktin myonisolenoidin jäljittimen tukirakenteiden toleranssisynteesiin. Malli voidaan myös integroida jo CERN:issä käytössä oleviin ohjelmiin, jolloin toleranssit voi asetta muillekin tukirakenteille kuin tässä työssä tutkitulle. Tukirakenteelle lasketut toleranssit esitellään taulukkomuodossa. Lisäksi, työssä suunniteltiin kattavat dimensionaalisen mittauksen menetelmät tutkittavan tukirakenteen laadun varmistamiseksi.

Keywords CERN, CMS, Hiukkasilmaisin, Hiukkasjälki-ilmaisin, Toleranssianalyysi, Toleranssisynteesi, Dimensionaalinen mittaus, Fotogrammetria, Herkkyysanalyysi

Acknowledgements

Foremost, I would like to thank the advisor of my thesis, Antti Onnela, for his inexhaustible guidance in tracker mechanics related subjects. His ability to point me in the right direction, and synthesize complicated matters into simpler form have been great assets in writing this thesis. I would also like to extend my thanks to Professor Kari Tammi for introducing me to this challenging topic and for his invaluable guidance in both thesis and career related subjects. Special thanks also go to the great people working at CERN, especially to Kamil Cichy, who introduced me to the complex mechanics of the TBPS support structure and who was always ready to answer my questions, and to Gabrielle Hugo, who gave me valuable assistance in developing the abstracted feature based model. A thank you goes to Jari Vepsälainen as well for his great support on sensitivity analysis related matters. I would also like to thank the Helsinki Institute of Physics for their financial support, without which I could not have focused my time entirely on the completion of this thesis.

I am also grateful to my girlfriend, my family and my friends for their support. I especially appreciated the weekly get-togethers at the Otsonlahti sauna that allowed me to take my mind off thesis –related subjects, and the unforgettable events organized by my close friends in the nation leading athletic team “CG”.

Table of contents

List of abbreviations

ABBREVIATION	MEANING
CMS	Compact Muon Solenoid
TBPS	Tracker barrel with pixel-strip sensors, a sub-detector of the future CMS Tracker
TB2S	Tracker barrel with two strip sensors, a sub-detector of the future CMS Tracker
CF	Carbon fiber
CFRP	Carbon fiber reinforced polymer
CERN	European Council for Nuclear Research
LHC	Large Hadron Collider
IP	Interaction point
CMM	Coordinate measurement machine
CAD	Computer assisted design
CAT	Computer assisted tolerancing
PS	Pixel-strip, a module type of the future CMS Tracker

1 Introduction

A substantial amount of new physics studies are centered on the research of our universe's smallest building blocks: the elementary particles. According to the standard model, these particles make up all matter and mediate the four fundamental forces. The study of them involves first generating elementary particles by colliding larger entities, such as protons, together nearly at the speed of light and then detecting the produced elementary particles with particle detectors. Many years of engineering work is required to build these detectors, and they have to work as designed on the first iteration. This calls for a thorough quality assurance of all systems in the detectors. In this thesis, the geometrical requirements of a future sub-detector of the Compact Muon Solenoid (CMS) experiment is analyzed, and its mechanical construction tolerances are allocated. A detailed dimensional measurement plan is also devised for that sub-detector.

1.1 CERN

CERN (Conseil Européen pour la Recherche Nucléaire) was founded in 1954 and its original purpose was to conduct research on the atomic nuclei. Today, the main area of research at CERN is to study the subatomic particles and their interactions, to figure out the underlying laws of nature that shape our universe. CERN has currently 22 member states and it has grown to become the largest high-energy physics laboratory in the world. The CERN's facilities are located near Geneva, and span across the border between Switzerland and France.

To study the particle interactions, scientists must accelerate particles nearly to the speed of light, and then collide them together or to a stationary target. The CERN laboratory houses several particle accelerators, of which the most notable is the 27 km long LHC (Large Hadron Collider). Currently, most of the research at CERN is focused on experiments with the LHC. To measure the particle collisions, scientists use specialized detectors to measure, record and analyze data about the subatomic particles.

The core of the physics research at CERN is made up of "experiments". Today there are 25 individual, active experiments at CERN. Each experiment typically has a particle detector system that is designed, constructed and operated by a scientific collaboration. Such collaborations usually have members also from countries that are not members of CERN. The two largest experiment collaborations and detectors at CERN are the CMS (Compact Muon Solenoid) and ATLAS. These are so-called general-purpose detectors, capable of investigating a large variety of physics.

1.2 Particle Physics

In the 19th century, the discovery of the atom led scientists first to believe that they had found the elementary particle that makes up all matter. However, this view was quickly denoted by research that implied that even the atoms were composed of smaller particles, such as the electron. In the middle of the 20th century, high-energy collisions revealed a staggering amount of new particles, which were eventually explained to be composites of a smaller number of elementary particles described by the standard model.

The standard model is a theory that classifies the known elementary particles, as well as explains three of the four fundamental forces: weak, strong and electromagnetic interactions. Gravity has remained unexplained. In the standard model, particles are divided into two categories: the fermions that form all matter and the bosons that act as force carriers that mediate the fundamental forces. Of these, the existence of the graviton that mediates gravity is only theorized. According to the current understanding, the elementary particles classified by the standard model are the fundamental building blocks of our universe; they are not divisible or composed of other particles. The standard model has been remarkably successful in predicting phenomena and particles, later confirmed by scientific experiments.

However, the standard model is not perfect and certain inconsistencies exist especially between it and general relativity. Other notable mysteries include why there is more matter than antimatter and the properties of dark matter and dark energy. At CERN, these mysteries are studied to develop the standard model further, as well as to develop new physics beyond the standard model.

1.3 CMS Experiment

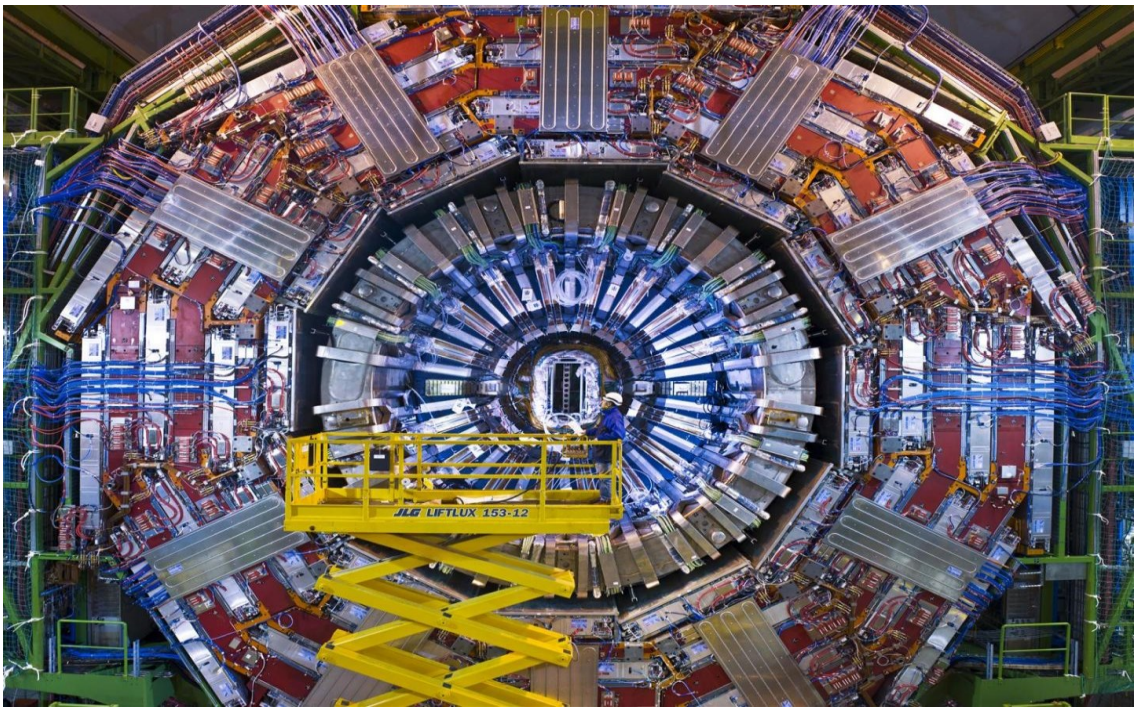

Figure 1. View to the inner parts of the CMS detector. [45]

The CMS experiment is focused around the general-purpose CMS detector that is built around the LHC beam-line (see Figure 1). The detector is a forward and backward symmetrical cylindrical apparatus. In the center of the detector, protons are collided together at such high energies that energy transforms into mass and sprays particles in all directions around the collision point. The trajectories and the energy of these particles are measured by successive layers inside the detector, as shown in Figure 2. The tracking detectors and the calorimeters are located inside a large and strong superconducting solenoid magnet that bends the trajectories of the particles with a 3.8 T magnetic field.

Bending the trajectories allows physicists to identify the charge of the particles, as well as to measure their momentum. Muon chambers, located outside of the magnet, complement the detector assembly.

The innermost part of the detector, the tracker, is designed to be as transparent as possible to all particles while the calorimeters measure and stop all particles except high-energy muons that reach the outermost detector layers, the muon chambers. Neutrinos pass undetected through all layers.

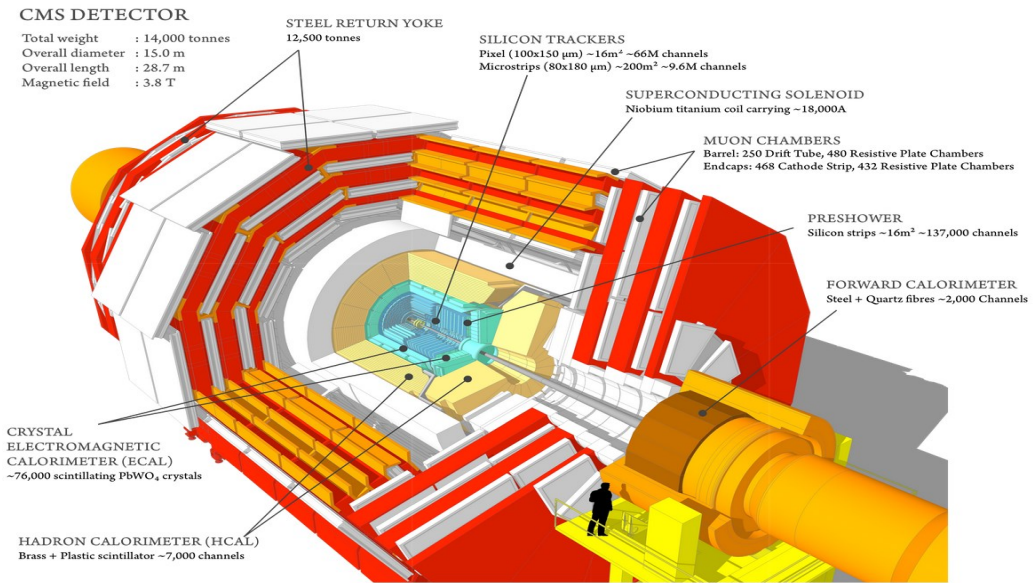

Figure 2. The CMS detector. [46]

This thesis focuses on the planned upgrade of the silicon tracker, and more specifically, on a sub-section called the TBPS (Tracker Barrel with PS modules, see Figure 3). In this section of the detector, silicon modules are arranged in a cylinder-like formation. The silicon sensors themselves are a collection of miniscule electrical channels. When a particle flies through a silicon module, it leaves electric charges. These charges are measured and allow to record where the particles have traversed, and track the paths of the particles.

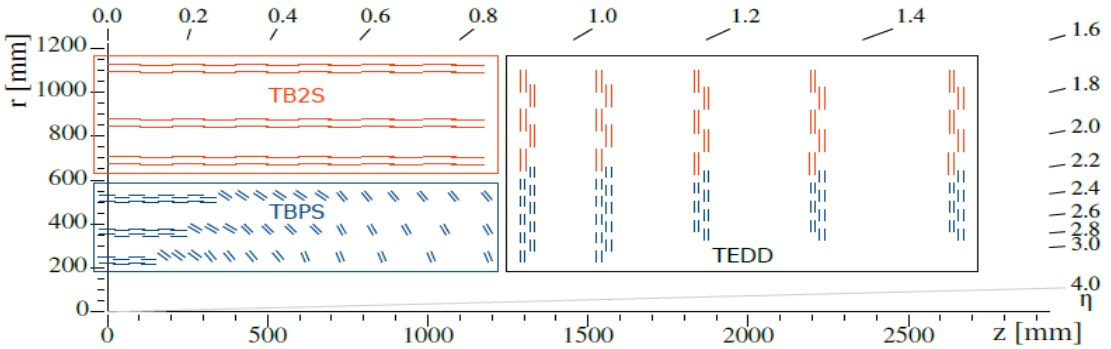

Figure 3. Sketch of one quarter of the outer tracker. The blue and red lines represent individual silicon modules. The proton-proton collisions occur at approximately z=0, r=0. [20]

It is essential for track reconstruction that the modules are arranged such, that a particle cannot traverse a detector layer without passing through at least one of the silicon sensors. This is commonly referred to as tracker hermeticity. This hermeticity

requirement is the functional requirement on which this thesis is based on: allocating tolerances for the support structures to position the silicon modules.

The outer tracker shown in Figure 3 is part of a so-called high-luminosity LHC upgrade, in which various parts of the LHC accelerator and detectors are upgraded or replaced. The high-luminosity upgrade of the LHC will result in more proton-proton collisions, producing more particles to be detected and more radiation to cope with. The upgrades are planned to take place in 2025.

1.4 Research problem

Efficient track reconstruction necessitates that the tracker's hermeticity requirements are met, while the amount of material in the tracker is minimized. Any material in the tracking volume increases probability of particle interactions and therefore reduces the measurement performance of the tracker itself as well as of the calorimeters and muon chambers located around the tracker.

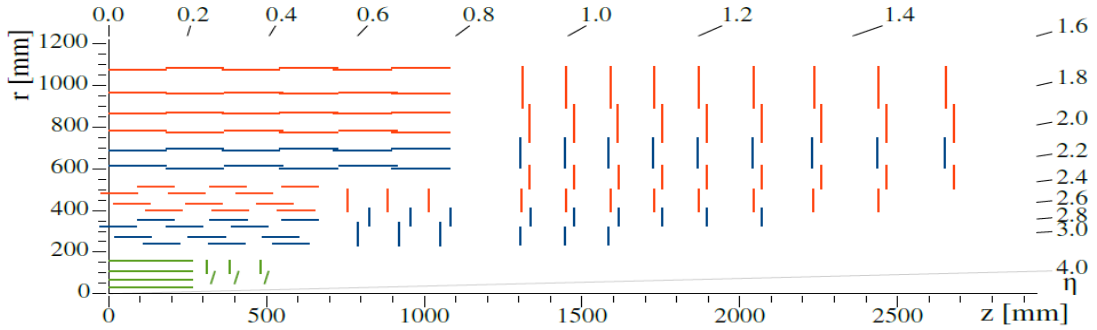

Figure 4. Sketch of one quarter of the tracking system currently used in the CMS detector. The inner tracker is also shown in green. [20]

Figure 4 shows the layout of the tracking system currently used in the CMS detector. Comparing it to the tracking system under development (see Figure 3), we can see that the most evident difference is in the region labeled TBPS, (Tracker Barrel with Pixel-Strip detector modules). In this region, the sensors are placed at various tilted orientations, rather than the usual vertical / horizontal orientations. This tilted arrangement maximizes the space coverage of the sensors to capture particles originating from the beams' interaction region. Therefore, this arrangement reduces the total amount of sensors in that region, and hence, saves costs, reduces services for the sensors and decreases the amount of support structure material.

However, such tilted arrangement turns out to be complicated to design and construct and this is in fact the first time that such a novel tracker geometry is being realized. Without previous knowledge on best practices, it is evident that an analysis needs to be carried out on how various imperfections in the tracker's support structure affect the sensors positions. Due the 3-dimensional nature of the tilted arrangement, the detector hermeticity is more complex to understand and study than in more 2-dimensional arrangements with the traditional horizontal / vertical sensor orientations. The planned mechanical support structure for the tilted sensor modules is discussed in more detail in section 3.2.

1.5 Goal

When the support structure for the new tracker is prototyped and finally built, the designers must know the accuracy needed in each of the parts and sub-assemblies. Estimating these accuracies by guesses, or worse, by demanding that the parts be as accurate as possible is neither cost, nor time efficient. It can also result in an unexpected loss of hermeticity, as some critical geometry effects may be overlooked. The aim of this thesis is to provide justified inputs for the precision requirement to be applied to the tilted sections of the TBPS by simulating the tolerances in an abstracted feature based model. The model will be constructed in such a way, that similar methods can also be utilized to allocate tolerances for structures other than the TBPS.

However, allocation of the tolerances is not enough. The structure's quality should also be assured afterwards to ensure that it conforms to the allocated tolerances. For this purpose, a detailed dimensional measurement plan will also be presented for the TBPS and its sub-sections.

1.6 Scope

This thesis focuses on the quality aspects of the TBPS sub-detector in the outer tracker of the CMS. The TBPS consists of tilted sensor module sections, and flat sections with sensors in the traditional barrel arrangement. The latter is not part of this analysis, as the focus is on the tilted sections. Furthermore, analysis of other CMS sub-detectors will not be carried out in this thesis.

Allocation of dimensional tolerances would arguably benefit from including dimensional changes due to thermal effects in the calculation of tolerances. However, the effect of such thermal effects was estimated to be low due to the structural material of the TBPS (carbon fibre reinforced polymer, CFRP) and as such, their effect is ruled out of this analysis. Furthermore, this thesis will not analyze all individual tolerances in the support structure, but rather allocate the tolerances for the sensor positions and extend those to the support structure features that affect the sensors positions. The particle trajectories are also modelled as straight, even though in reality they are curved by the 3.8 T magnetic field. This simplifies the model substantially while affecting the uncertainty of results only marginally.

1.7 Outline

In chapter 2 a literature review is presented on the current state-of-the-art tolerance analysis methods, and a suitable method is chosen for the analysis of the TBPS tilted sections. This is followed by the tolerance analysis of the support structures in chapter 3 Section 3.1 gives a more detailed overview of the silicon modules, while section 3.2 discusses the TBPS and its mechanical structures. The previously mentioned hermeticity requirement is thoroughly assessed in section 3.3, while the rest of the chapter deals with the actual tolerance analysis. Chapter 4 describes the dimensional measurement of the TBPS, starting by a brief literature review of large-scale metrology in section 4.1 and a description of solutions available at CERN in section 4.2. The following sections give a detailed description of how to dimensionally measure the TBPS at various assembly stages.

2 Geometric tolerancing

Geometric tolerancing of products is the process of specifying how much geometric dimensions of the product may vary. The goal of this process is to optimize the trade-off between manufacturing costs and product quality; tight tolerances usually equal high manufacturing costs, and loose tolerances result in decreased quality of the product and a high scrap-rate. As such, efficient tolerancing of products can even be a competitive edge in the marketplace.

The process of allocating tolerances begins by identifying a geometric functional requirement (or requirements) of the product. For example, this can be the clearance between an engine piston and a cylinder block piston hole in a motor as illustrated in Figure 5.

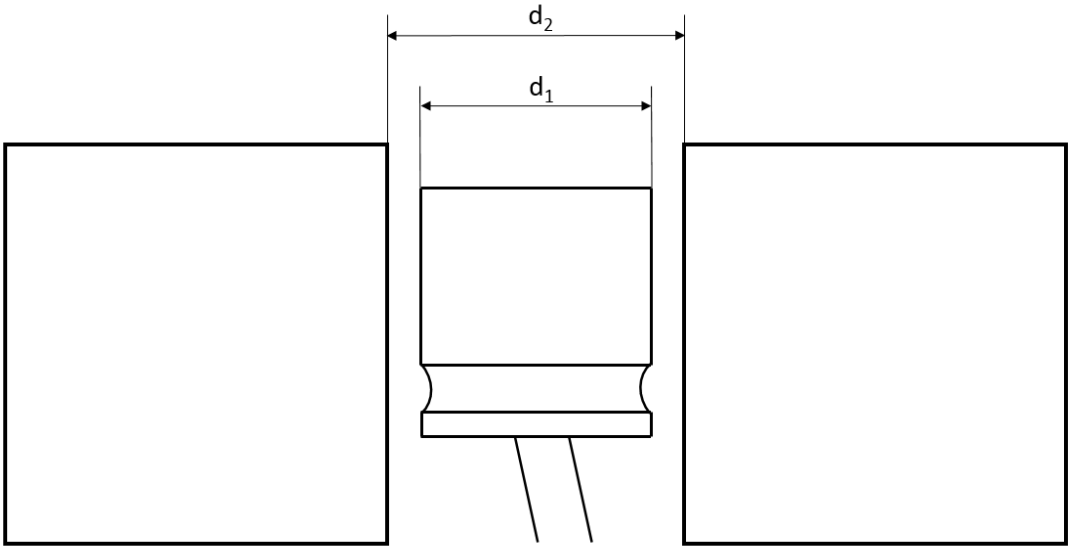

Figure 5. Clearance between an engine piston and a cylinder block. d_1 = diameter of the piston and d_2 = diameter of the cylinder hole in the engine block. The clearance (Y) between the piston and the engine block is $Y = d_2 - d_1$.

After a geometric functional requirement has been identified, the process continues by the identification of product dimensions that make up that functional requirement. For example in Figure 5, the cylinder diameter d_1 and engine block cylinder hole diameter d_2 are the dimensions on which the cylinder clearance depends on. In this case, we can easily formulate an equation that links the functional requirement (clearance, Y) to the manufacturing dimensions of the assembly (diameters, d_1 and d_2):

$$Y = d_2 - d_1.$$

Such equations are commonly called assembly functions, and their result the assembly resultant. These functions can be utilized with methods described in chapter 2.1 to allocate tolerances to the manufacturing dimensions; provided that a functional tolerance for the assembly resultant is known.

However, in real-world cases the main issue is usually the formulation of the assembly function. This can often be difficult or even impossible for the product designer if only

generic geometrical methods are utilized, such as in the piston – cylinder block example. A lot of research has been conducted to develop mathematical models for this task, but none of them is uniformly accepted. These models will be described in chapter 2.2.

The need for a comprehensive and uniformly accepted model is highlighted by the competitive gain that efficient tolerancing can attain, but also because geometric tolerancing is a field where the work of design engineers and manufacturing engineers can collide, resulting in counterproductive arguments. Design engineers typically prefer tight tolerances so that their designs functional requirements are guaranteed to be fulfilled, while manufacturing engineers opt for loose tolerances to reduce manufacturing costs. This confrontation may be further aggravated by choosing tolerances by rules of thumb, with no comprehensive analytical reasoning behind the choices. [1]

Tolerances in general are expressed in drawings by two methods: conventional tolerancing and geometric tolerancing. In conventional tolerancing, tolerances specified are understood as allowing dimensional variation of a part only in the direction of the dimension for which the tolerance is specified. An example of conventional tolerancing is shown in Figure 6.

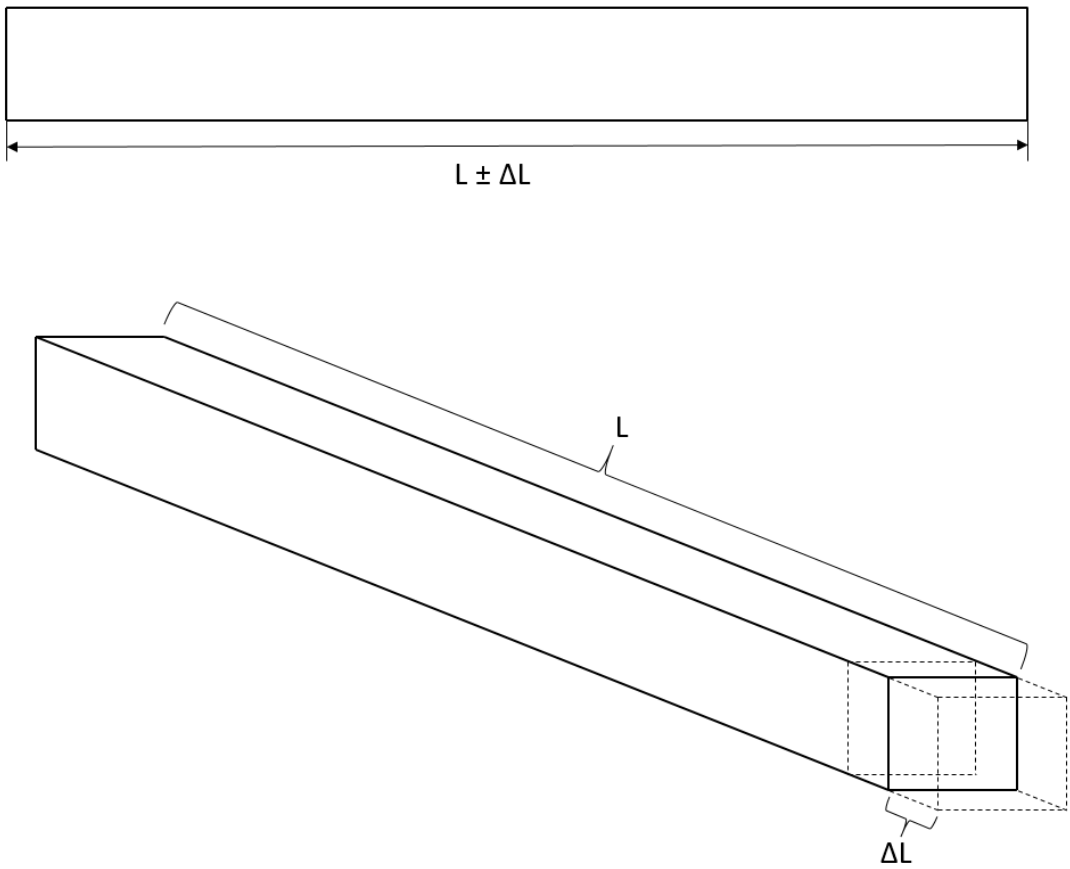

Figure 6. Conventional tolerancing. Rod nominal length L is associated with tolerance ΔL that can either extend or reduce L. The upper image shows how the tolerance would be displayed in an engineering drawing, and the lower image displays the effect of that tolerance. The dashed line section includes all the possible locations that the end of the rod can take.

Conversely, geometric tolerancing takes into account the inevitable form and rotational alignments that product features have. An example of geometric tolerancing, parallelism, is shown in Figure 7. There are multiple different methods of specifying geometric tolerances, but listing and explaining all of them is outside the scope of this thesis. The reader is referred to standards [2] and [3] for their explanations.

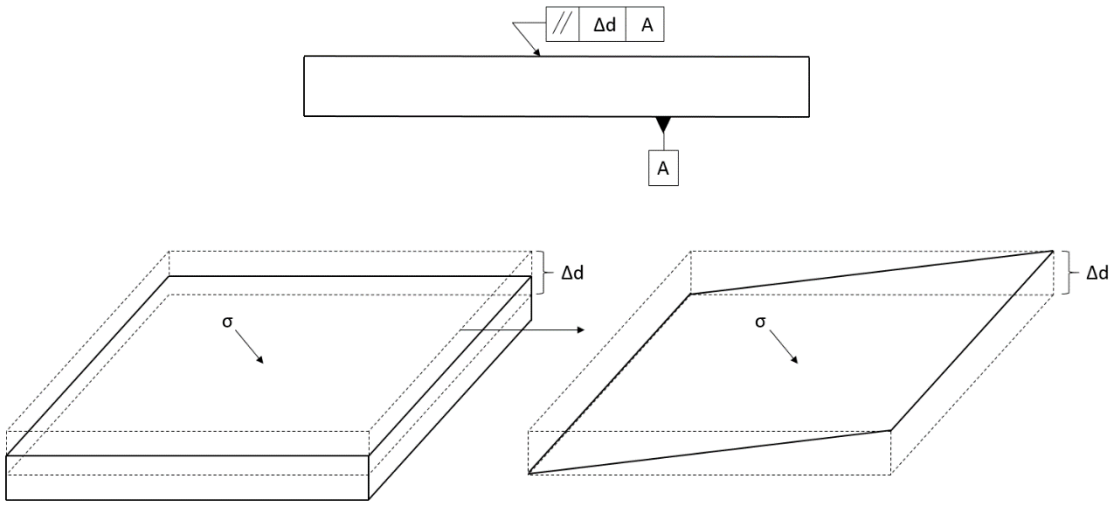

Figure 7. Geometric tolerancing. A parallelism tolerance is indicated for the upper plane (σ) of the part, with the lower plane as its reference. The upper plane (σ) of the part must exist between two virtual planes that are parallel to the reference plane (lower plane of the part), with the specified distance Δd between them. The upper image shows how the tolerance is displayed in an engineering drawing, and the lower image displays the effect of that tolerance. The lower right-hand image presents that plane σ can have angular displacement within the restrictions of the specified dimension Δd. Note that a parallelism tolerance does not place a restriction on how far plane σ is from the reference plane.

The principles employed in the use of conventional and geometric tolerancing are defined by the ASME [2] and ISO [3] standards that deal with tolerancing. An example of such a principle is the independency principle in the ISO standard: if multiple tolerances are allocated to a single feature on a part, the tolerances must hold true when inspected independently from one another. For example, this could be a conventional distance tolerance and a geometric parallelism tolerance on a feature. Another important rule is the datum precedence: the plane, line or point marked as a reference for a geometric tolerance should be considered perfect for measuring the geometric tolerance. As the formulation of these principles is equivocal, a comprehensive mathematical model that conforms to them is very hard to design.

In this chapter, tolerance analysis methods are first described generally. Secondly, the major proposed methods for formulating assembly functions are described, and lastly, these methods are compared.

2.1 Tolerance analysis

The term “tolerance analysis” is sometimes associated with the entire process from formulating the assembly function and deciphering individual tolerances by applying it analytically [4], and sometimes as just the process of analyzing the assembly function [1]. In this thesis, the former meaning of the term is used.

As mentioned before, the anterior part of tolerance analysis (formulation of the assembly function) is arguably the more time-consuming part of the analysis and the one on which no agreed upon method exists. However, mostly agreed upon methodology has been applied to the posterior part of the analysis (analysis of the assembly function). These methods will be discussed in this chapter, along with general concepts related to the methods for formulating the assembly function.

An established assembly function can be evaluated with various methods of which the simplest is the worst-case method (equation 1). In this method, the manufacturing tolerances are chosen so that their cumulative effect, when the tolerances are in their worst-case extremities, does not exceed the assembly tolerance. As can be expected, using the worst-case method results in very tight tolerances and a high manufacturing cost. On the other hand, this method produces a theoretical assembly yield rate of 100%. [1]

The root-sum square method (equation 2) assumes that all the manufacturing tolerances are normally distributed with the mean values being the nominal values of the dimensions the tolerances are associated with. While the worst-case method was based on the cynical assumption that tolerances are constantly at their worst possible extremities, the root-sum square methods assumption of normal tolerance distribution is idealistic: the method results in looser tolerances than the designer intends to achieve the wanted assembly yield-rate. The worst-case and root-sum square methods are not realistic representations of tolerance accumulation, but they have been used quite extensively due to their simplicity. The natural successor to these two methods is to take the average between the two (equation 3). This method produces results that are better matched with reality, but lacks mathematical basis for a more comprehensive representation. [1]

The estimated mean shift method (equation 4) allows for a more realistic representation of the underlying manufacturing processes that result in manufacturing tolerances. It contains both the worst-case and root-sum square methods, but allows for shifting the mean of the normally distributed tolerances, mimicking the actual manufacturing processes more realistically. This of course necessitates that data are available that characterizes the manufacturing processes in terms of their performance distribution. [1]

$$\sum_{i=1}^{n_k} \delta_{i_d} \leq \Delta Y_k \tag{1}$$

$$\sqrt{\sum_{i=1}^{n_k} \delta_{i_d}^2} \leq \Delta Y_k \tag{2}$$

$$\frac{1}{2}\left[\sum_{i=1}^{n_k}\delta_{i_d}+\sqrt{\sum_{i=1}^{n_k}\delta_{i_d}^2}\right]\leq \Delta Y_k \tag{3}$$

$$\sum_{i=1}^{n_k} m_i\delta_{i_d}+\frac{Z}{3}\sqrt{\sum_{i=1}^{n_k}(1-m_i)^2\delta_{i_d}^2}\leq \Delta Y_k \tag{4}$$

Where δ_{i_d} are the manufacturing tolerances associated with the assembly function, n_k is the number of manufacturing dimensions associated with the *k*th assembly function and ΔY_k the allowed variation in the resulting functional dimension, or assembly tolerance. m_i are the mean shift factors of the manufacturing tolerances and Z a variable that can be chosen according to the demanded yield rate. Typically, $Z = 3$, which corresponds to a yield of 99,73%. In the case of non-linear assembly functions, the manufacturing tolerances are multiplied by their sensitivities (partial derivatives) [5]. [1]

More sophisticated methods exist as well that provide means for describing the mean, variance, skewness and kurtosis of the tolerance distributions. However, these methods require that highly accurate manufacturing process information is available, which is not the case in the development of a particle tracker support structure. Thus, the methods are not described here and the reader is referred to [5] for their descriptions.

So how does one decipher individual tolerance values from the aforementioned equations? The simplest way would be to decide that all manufacturing tolerance magnitudes be equal. This however, is hardly ever applicable. If the assembly function is relatively simple and linear, as in the piston – engine block example, the tolerances can be adjusted according to the magnitudes of the manufacturing dimensions with which they are associated. Another way would be to adjust the tolerances based on the manufacturing process with which the dimension is realized; an assembly of a cast part and a machined part would generally benefit from allocating looser tolerances on the cast part than on the machined part.

If the assembly function is non-linear and (or) complex, the tolerances can be adjusted based on the assembly resultants sensitivity to each tolerance. This sensitivity can be solved by first linearizing the assembly function by its variables mean values using Taylor's series expansion and then solving the tolerance sensitivities from their partial derivatives. Another method is to use Monte-Carlo simulation and variance based methods. When the adjustment factors are solved, the tolerance magnitudes can be solved by perturbation of the assembly function: an individual tolerance is incrementally raised until the assembly tolerance is reached, then that tolerance adjusted with the corresponding factor, implemented into the assembly function and the process repeated for each individual tolerance. [6]

As mentioned before, the complicated part of tolerance analysis is usually not the analysis of the assembly function, but rather the formulation of the assembly function. Methods designed for this purpose are described next.

2.2 Tolerance analysis methods

Various authors have proposed distinct methods for formulating the assembly function. The methods can be roughly separated into two categories: tolerance zone based models and other models. The suitability of a tolerance analysis method is usually evaluated by how well it conforms to the ISO and ASME standards, its applicability to be analyzed with the methods described in the previous section, how well the method integrates into a computer assisted design (CAD) or computer assisted tolerancing (CAT) environment and how easy the method is to use.

2.2.1 Tolerance charts

Out of the models described in this chapter, tolerance charts are perhaps the most simple. In a way, tolerance charts can be interpreted as a manual tool for composing an assembly function for worst-case analysis. Other analytical methods are not applicable to tolerance charts. Even though the method is arguably unsuited for comprehensive tolerance analysis, it has been used extensively by designers and draftsmen due to its simplicity. [6]

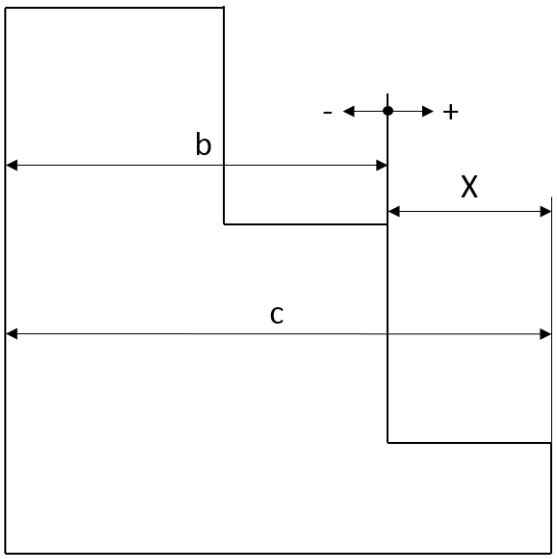

Figure 8. Example of evaluating a parts tolerance stack-up conditions using tolerance charts. X is the assembly resultant.

Consider a part as shown in Figure 8. The process of using a tolerance chart to identify various tolerance stack-up conditions in the part begins by locating an one dimensional coordinate system at the left side of the assembly resultant for an analysis carried out for horizontal dimensions (as in Figure 8). If the analyzed dimensions are vertical, the coordinate system is located at the bottom end of the corresponding assembly resultant. The positive direction of the coordinate system is specified to be on the assembly resultant's side. [6]

After the coordinate system has been located on the engineering drawing, the dimensions that align with the coordinate system are traversed starting from the origin of

the coordinate system. In the example in Figure 8, we can traverse the dimensions either as:

$$-b + c - X = 0$$

or

$$X - c + b = 0.$$

Both of these equations produce the same stack-up condition:

$$X = c - b.$$

After the stack-up condition(s) has been identified, tolerances associated with the dimensions are filled to a tolerance chart (Table 1) conforming to the following rules:

1. if the dimension has a positive sign, that dimensions maximum value (according to its tolerance) is inputted into the max column and its minimum value to the min column,
2. if the dimension has a negative sign, that dimensions maximum value is inputted into the min column and its minimum value to the max column,
3. all the inputted dimensions minimums and maximums are assigned a sign depending on the sign of the dimension in the stack-up condition. In the example of Figure 8, all minimums and maximums of dimension c are assigned a positive sign, and the minimums and maximums of b a negative sign),
4. on the last column, the difference between the dimensions in that row are inputted ($U_n = V_{n1} - V_{n2}$).

On the last row of the chart, the values of the columns are summed together. The sums of the min and max columns correspond to the two worst-case results. If the sign of the sum is negative, it implies clearance in an assembly analysis, or that the analyzed feature would not exist in a part analysis. A positive sign implies interference in an assembly analysis, or that the analyzed feature exists in a part analysis. The sum of the last column is used for checking the validity of the analysis: its value should correspond with the sum of all the tolerances in the analyzed stack-up condition. [6]

Table 1. Tolerance chart. [6]

Stack Contributor	Max Column		Min Column		Δ
	Sign	Value	Sign	Value	
1		V_{11}		V_{12}	U_1
…		..		..	..
N		V_{n1}		V_{n2}	U_n
Sum		$\sum_{i=1}^{n} V_{i1}$		$\sum_{i=1}^{n} V_{i2}$	$\sum_{i=1}^{n} U_i$

As can be expected, this process is quite cumbersome to carry out for complex stack-up conditions. This is particularly true when geometric tolerances have to be accounted for, which can be done by using special rules for each geometric tolerance. For this purpose, the process of tolerance charting has been automated. [7]

While automation solves the inconveniency of manually charting the tolerances, the method does suffer fundamentally from an essential issue: as the tolerances are analyzed only in one direction at a time, the process fails to account for variation in other directions that can (and usually do) have an impact on the assembly resultant. On the other hand, the tolerance chart method does benefit from its simplicity and relative ease of use. [6], [7]

2.2.2 Parametric tolerance analysis

Parametric tolerance analysis takes advantage of the explicit equations that can be generated from dimensions and constraints applied in the design of a CAD model. These equations fundamentally describe the assembly function to which analytical methods can be applied. The drawback is that the parametric equations are point-to-point based, while conforming to the ISO and ASME standards requires that a method rather be tolerance zone-based so that the method conforms to the datum precedence rule and that all geometric tolerances can be expressed. Nevertheless, parametric tolerance analysis is the method that the major CAT and CAD software use, either directly based on the CAD model or indirectly by first constructing an abstracted model based on the CAD model. [6], [8]

The two major CAT software currently available are the 3DCS Variation Analyst [9] by DCS and the CETOL 6σ [10] by Sigmetrix. The recent trend seems to be the integration of these tools into more inclusive design software, such as in the case of the eTol-Mate by Tecnomatix, now marketed as a comprehensive manufacturing design tool by Siemens [11].

In parametric tolerance analysis, the acquired assembly function is either linearized or then used directly for Monte-Carlo simulations. The latter method is quite resource-heavy when performed on a CAD model, because changing a dimension in the dimension-constraint chain of a parametric model requires that the underlying equation be "rolled back" to the changed dimension and then re-solved. Because of this, the more common approach is to import the CAD model into a CAT environment, where an abstract representation of the CAD model is created by the user. This is the method used in the described software as well. [8]

Results obtained from parametrical tolerance analysis are the list of contributors, sensitivities, percentage contributions and solutions to analysis methods described in 2.1 (both worst-case and statistical analysis). This applies to both the linearization based parametric tolerance analysis and to the alternative method based on Monte-Carlo simulation. [8]

2.2.3 Abstract feature based models

In an abstract feature based model, features are represented as elementary shapes, which are points, lines, planes and cylinders (see Figure 9), and interaction between the features as generic mathematical formulas, such as distance and angle between points,

lines and planes. The result is computationally efficient, so that Monte-Carlo simulations and perturbation can be used to analyze the tolerances. [6], [8]

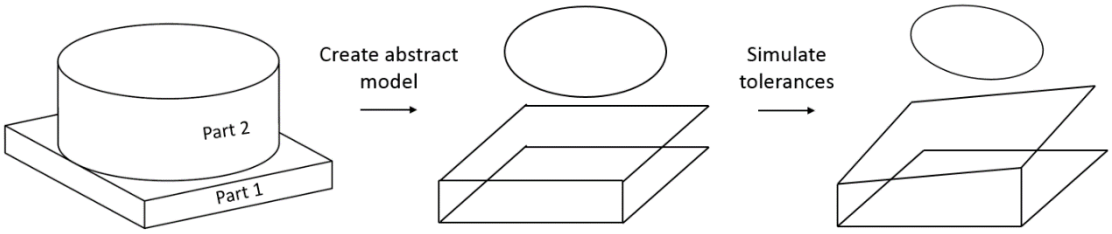

Figure 9. Abstract model creation from CAD model.

Criticism of parametric tolerance analysis and abstract feature based models includes the aforementioned failure to conform to the ISO and ASME standards and the need for expertise in model creation. Because planes are expressed either with parametric equations that describe the features vertex points, or with elementary shape equations, form tolerances cannot be accounted for. As mentioned before, the methods do not conform to the datum precedence rule described by the standards. [6], [8], [12]

Furthermore, the process of creating an abstract model is quite cumbersome for the designer and requires expertise. This is further complicated by the fact that parametric model porting file-formats (usually STEP) do not translate dimensional or tolerance information from the CAD environment to the CAT environment. This means that the designer has to specify all of the dimensions and tolerances of a product separately in the latter environment. The quality of results relies heavily on the expertise of the designer, which is a problem. [6], [8]

However, parametric tolerance analysis and abstract feature based models are developed based on the matured CAD environments. This makes integrating them to the available CAD tools easy, which in turn makes the methods highly accessible for designers. Despite its drawbacks, parametric tolerance analysis is a powerful tool for producing accurate results, if the user has the necessary expertise to use it properly.

2.2.4 Vector loop (kinematic) model

Based on previous work in developing kinematic models for moving assemblies and kinematic joint definitions, Chase et al. [5] devised a vector loop model for assembly function construction. In the model, component dimensions and kinematically variable dimensions are represented as vectors that join together to develop stack-up conditions of those dimensions. Assembly joints are described with traditional kinematic joints, which allow certain degrees of freedom for movement.

Such an approach benefits from the slight alleviation of stack-up condition identification and formulation, and from that well-known kinematic practices can be applied to the vector loop. The method is also more computationally efficient than parametric tolerance analysis described before. This is because only the relevant sources

of variation are included. An example of vector loop creation is illustrated here, based on the example given in [5].

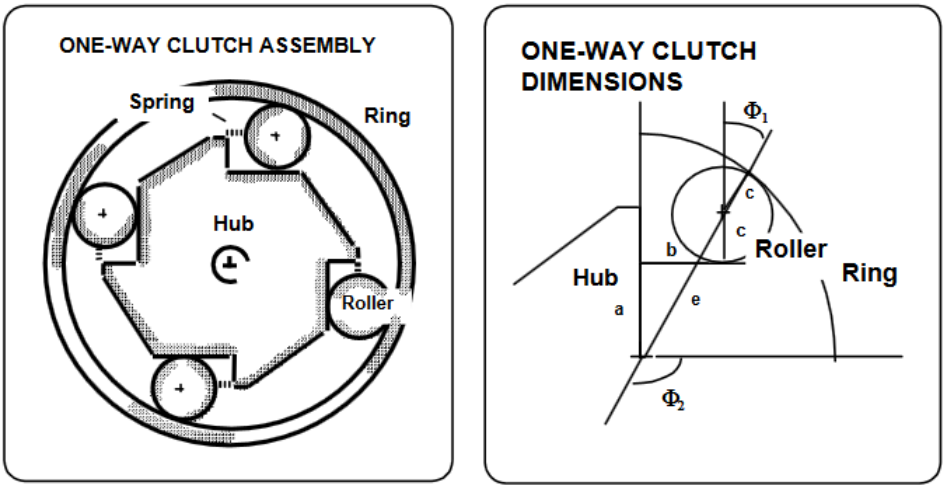

Figure 10. One-way clutch assembly and its relevant dimensions. [5]

A generic one-way clutch assembly is shown in Figure 10. If the outer ring rotates clockwise, the rollers on the end of the springs lock between the hub and the outer ring, rotating the hub clockwise as well. In counterclockwise rotation, the rollers slip towards the spring, and the hub does not rotate.

The relevant dimensions related to the operation of the clutch are displayed on the right-hand picture of Figure 10. A functional requirement can be identified for the pressure angle ϕ_1: if the angle is too large, the clutch will not lock and if it is too small, the clutch will not unlock. The vector loop representation of the relevant dimensions can be displayed as shown in Figure 11.

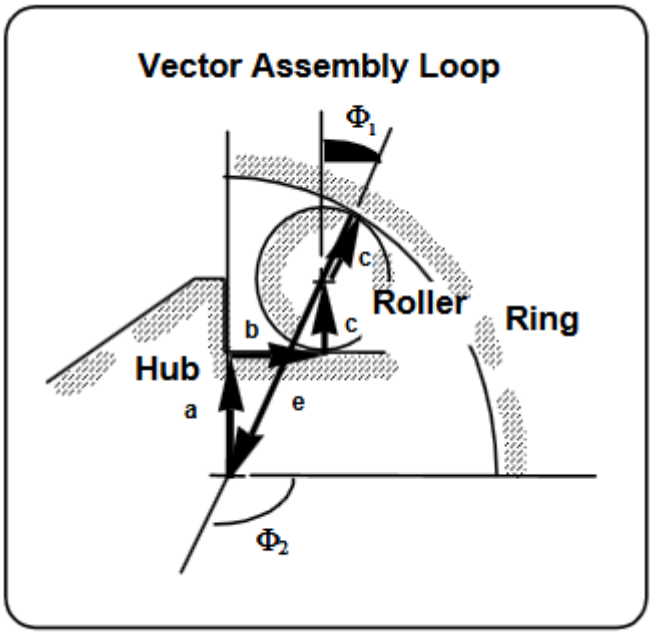

Figure 11. Vector loop representation of the one-way clutch assembly. [5]

Summing the vector components in the x, y and rotational directions gives us three equations of the form:

$$H_x = \sum_{i=1}^{n} L_i \cos\left(\sum_{j=1}^{i} \varphi_j\right) = 0,$$

$$\mathrm{H_y} = \sum_{\mathrm{i=1}}^{\mathrm{n}} \mathrm{L_i} \sin\left(\sum_{\mathrm{j=1}}^{\mathrm{i}} \varphi_{\mathrm{j}}\right) = 0,$$

$$H_\varphi = \sum_{i=1}^{n} \varphi_j = 0° \; or \; 360°.$$

Note that vector rotational components φ_j are the relative rotational dimensions between two successive vectors, rather than rotational dimensions that are referenced to some global point. This allows rotational shifts to propagate through the model realistically. In the example of Figure 11, these equations become:

$$H_x = b + c * \cos(90° + \varphi_1) + e * \cos(270° + \varphi_1) = 0,$$

$$H_y = a + c + c * \sin(90° + \varphi_1) + e * \sin(270° + \varphi_1) = 0,$$

$$H_\theta = 90° - 90° + 90° + \varphi_1 + 180° + \varphi_2 = 0,$$

from which $\varphi_1$can be solved in terms of the known dimensions a, c and e. [5]

In the case of three-dimensional tolerance analysis, the vector loop model becomes slightly more complicated. The vector projections can still be expressed in x, y and z similarly as in the two-dimensional case, but vector rotations can only be expressed with rotational matrices. Gao et al. [13] apply the following convention to construct the assembly function.

For each joint in the assembly that joins two vectors in the vector loop, the relative rotation between the vectors can be expressed with three rotational matrices about the x, y and z-axes, and the length of the next vector as a translational matrix (T):

$$[R_x] = \begin{bmatrix} 1 & 0 & 0 & 0 \\ 0 & cos\phi_x & -sin\phi_x & 0 \\ 0 & sin\phi_x & cos\phi_x & 0 \\ 0 & 0 & 0 & 1 \end{bmatrix},$$

$$[R_x] = \begin{bmatrix} cos\phi_y & 0 & sin\phi_y & 0 \\ 0 & 1 & 0 & 0 \\ -sin\phi_y & 0 & cos\phi_y & 0 \\ 0 & 0 & 0 & 1 \end{bmatrix},$$

$$[R_x] = \begin{bmatrix} cos\phi_z & -sin\phi_z & 0 & 0 \\ sin\phi_z & cos\phi_z & 0 & 0 \\ 0 & 0 & 1 & 0 \\ 0 & 0 & 0 & 1 \end{bmatrix},$$

$$[T] = \begin{bmatrix} 1 & 0 & 0 & L \\ 0 & 1 & 0 & 0 \\ 0 & 0 & 1 & 0 \\ 0 & 0 & 0 & 1 \end{bmatrix}.$$

Using this convention, the assembly function can be written as the product of all these matrices derived from the joints:

$$[R_1][T_1][R_2][T_2] \dots [R_n][T_n][R_f] = [I],$$

where $[R_i]$ is the product of rotation matrices at joint i, $[T_i]$ is the translational matrix at joint i, $[R_f]$ is a rotational matrix resultant of the final vector that closes the loop and $[I]$ the identity matrix. [13]

Geometric tolerances can be incorporated in the method by transforming them into rotational (and possibly translational) matrices at the joint, and then added to the matrix representation of the assembly function as separate entities at the joints. [14]

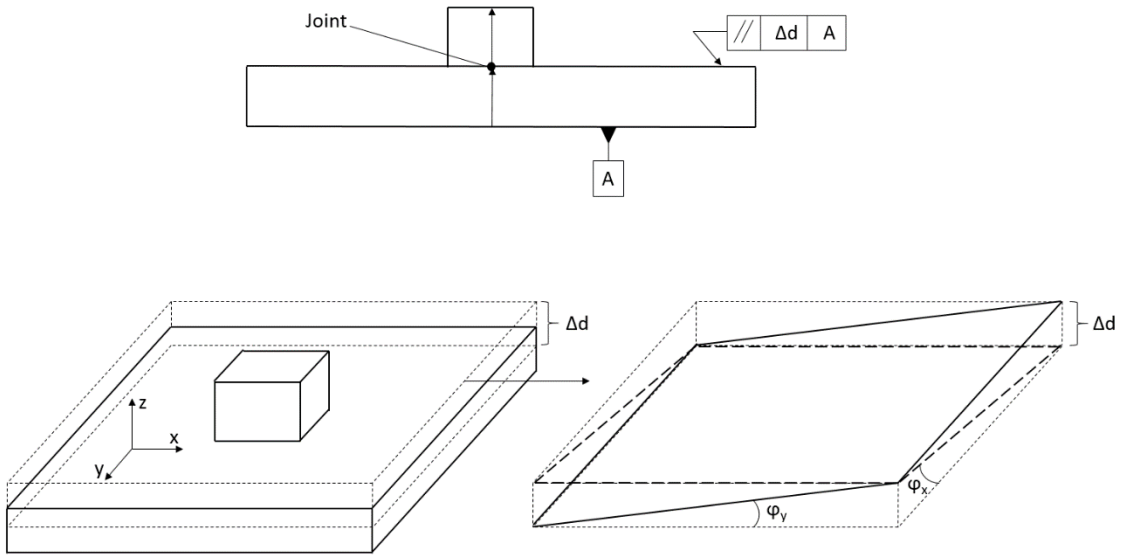

Figure 12. Geometric tolerance translation to joint translation and rotations.

Figure 12 demonstrates how a parallelism tolerance can be translated to its rotational and translational effects on the displayed joint, where φ_x and φ_y are the rotational components that can be directly inserted into the joints rotational matrices, and Δd the translational component, which can be inserted to the joints translational matrix. In such a configuration, the assembly function would be of the form:

$$[R_1][T_1] \dots [R_i][T_i][R_o][R_{gi}][T_{gi}][R_{-0}] \dots [R_n][T_n][R_f] = [I],$$

where $[R_i]$ and $[T_i]$ are the rotational and translational matrices associated with joint i that are a result of conventional tolerances and $[R_{gi}]$ and $[T_{gi}]$ the rotational and translational matrices associated with joint i that result from a geometric tolerance affecting that joint. $[R_o]$ is a rotational matrix that rotates the joints local coordinate reference system to align with the coordinate system of the geometric tolerances reference plane and $[R_{-o}]$ its reverse counterpart. This is to conform to the independency principle described above, by dealing with the geometric and conventional tolerances separately in the assembly function. [14]

The vector loop model has been criticized for its complexity [6] and non-conformance to the standards [12], [15]. In [15], the vector loop model was found to overestimate the effect of tolerances, when both conventional and geometric tolerances were applied to a

single feature. This was accounted to the method of including geometric tolerances in the model, as the procedure does not actually fully conform to the independency principle.

Consider a feature associated with a conventional tolerance and a parallelism tolerance. Because the parallelism tolerance contains a translational component, that is added to the assembly function. Now, the conventional tolerance was already included in the assembly function, and it essentially sets a limit on the translational variation component of the parallelism tolerance. This is not accounted for in the vector loop model, so it overestimates the assembly resultant when features are associated with multiple tolerances. This can be alleviated by acknowledging the issue and inducing proper error budgeting.

Furthermore, similarly to the creation of an abstract model in parametric tolerancing, the creation of a vector loop requires explicit expertise from the designer. This is not ideal. Automating the process in a CAD environment, as hinted at by Chase et al. [5], would solve this issue, but currently no well-known tools exist based on this method.

2.2.5 Tolerance map

A tolerance map is a hypothetical volume of points that relates to a features tolerance zone by areal coordinates. Stack-up conditions can be evaluated in assemblies by creating tolerance maps for each feature, adding them together with Minkowski sum, and then analyzing the resulting volume of points. Tolerance maps are arguably more complex to formulate than the methods described previously. The reason for these efforts is to develop a mathematical model, based on multi-variate representation of tolerance zones that describes conventional and geometric tolerance accumulation and interaction accurately while still conforming to the ISO and ASME standards. [8] [12] [16]

The formulation of a tolerance map for a round surface is shown in this section, based on the example of [12]. Consider the end of a rod shown in Figure 13, where a conventional tolerance of size t is imposed on the end of the rod. This essentially means that the plane at the end of the rod must reside in a tolerance zone restricted by the geometry of the rod and planes σ_1 and σ_2. However, that plane is free to assume any

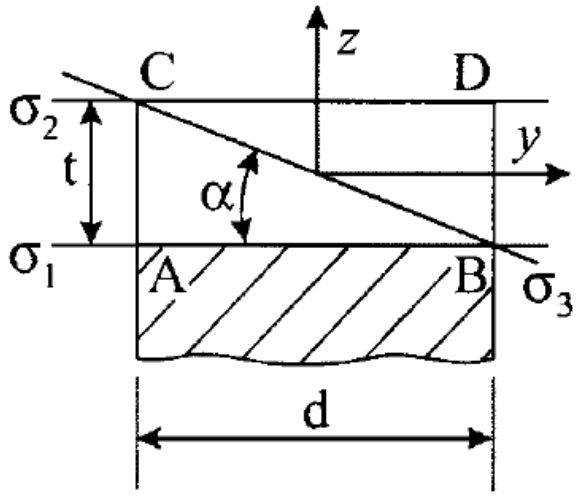

Figure 13. Tolerance zone on the end of a round rod. [12]

angular orientation in three dimensions, as long as it resides inside the region between planes σ_1 and σ_2. [12]

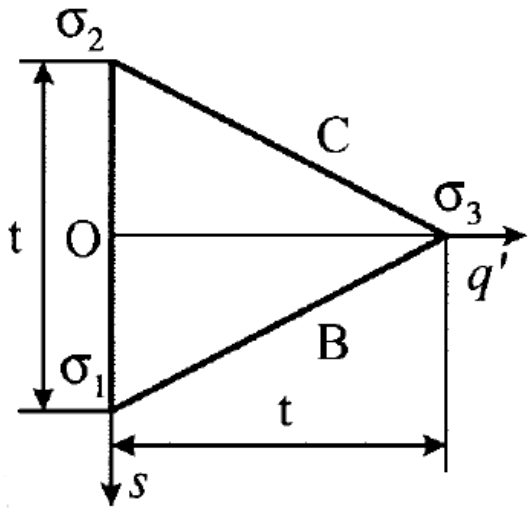

Figure 14. Point map that represents half the planes in one diametral section of the tolerance-zone. [12]

Now, we can translate planes σ_1, σ_2 and σ_3 to areal coordinate points that form a triangle shaped point map as illustrated in Figure 14. In this point map, planes in the tolerance-zone are represented as points. In Figure 14, points on the line between σ_1 and σ_3 represent all the planes that are perpendicular to the x-axis in Figure 13, and travel through point B. Conversely, points between σ_2 and σ_3 represent all the planes that are parallel to the x-axis, and travel through point C. Finally, points between σ_1 and σ_2 represent the planes that are perpendicular to the z-axis, and between the planes σ_1 and σ_2. [12]

As mentioned, the point map in Figure 14 represents half of the planes in the diametral section in Figure 13. To illustrate the planes that are parallel to the x-axis and travel through points A and D in Figure 13, we can mirror the point map in respect to the line between points σ_1 and σ_2 in Figure 14, and name the plane that travels through points A and D as σ_7. In fact, to account for all the possible planes in three dimensions, the point map in Figure 14 can be swept a full turn about the line between σ_1 and σ_2. This generates the tolerance map of the end of the rod in Figure 13 (see Figure 15). In this tolerance map, any possible orientation and location that the plane at the end of the rod can take can be illustrated as a point (σ) that resides within the tolerance map. [12]

In a tolerance map, the angular variations of a plane are decoupled from translational variations in the tolerance zone. Moving along the s axis of a tolerance map implies translational displacement in the tolerance zone. Conversely, moving along the p' and q' axes of the tolerance map imply plane angular displacement around the y and x axes. This decoupling allows the creation of tolerance maps for part features that are constrained by both conventional and geometric tolerances. For example, in the case of a conventional tolerance and a parallelism tolerance, the tolerance maps points σ_3, σ_4, σ_7 and σ_8 in Figure 15 would be moved closer to the origin. [12]

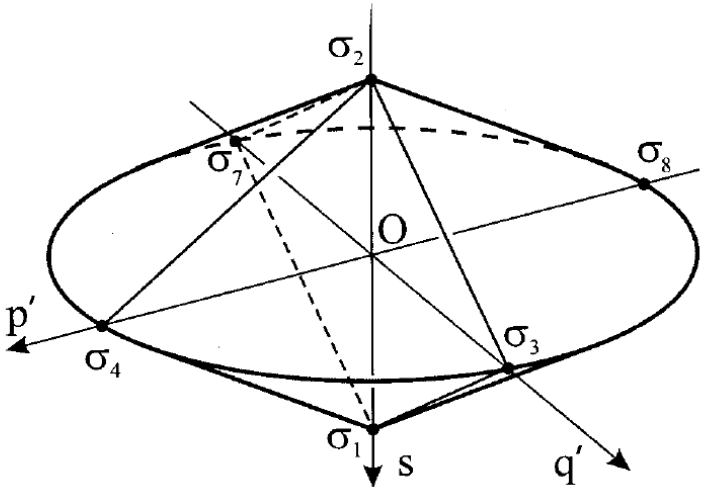

Figure 15. Tolerance map of a rods end with a conventional tolerance. [12]

To analyze stack-up conditions, all involved features are represented as tolerance maps; along with the functional requirement. Tolerance map of the functional requirement is usually called the functional tolerance map. The tolerance maps of the affecting features are then combined using the Minkowski sum to form an accumulation map. The Minkowski sum is a vector sum of all points in a tolerance map with the points of the next tolerance map [6]. This accumulation map can then be fitted inside the functional tolerance map. Optimal tolerances can be selected by varying the accumulation maps size so that it fills the functional tolerance map to the greatest extent. [12]

2.2.6 Jacobian-based model

A chain of dimensions that vary according to tolerances associated with them is closely related to kinematic chains familiar in robotics. The vector loop model developed by Chase et al. [5] was based on such a comparison, but other models have been developed as well. Lafond and Laperrière [17] suggested a Jacobian-based modelling method, somewhat similar to the kinematic model described earlier.

In the Jacobian-based model, the chain of dimensions that affects the functional requirement of an assembly is first identified. Part specific functional elements and kinematic pairs of parts are included in the chain separately, but treated as topologically the same (see Figure 17). [17]

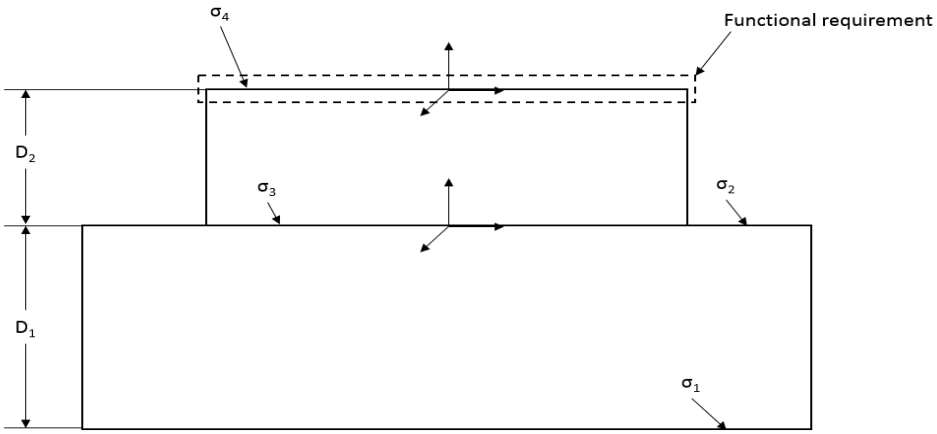

Figure 17. Dimensional chain identification in Jacobian-based model. A functional requirement is associated with the plane σ_4. This functional requirement is dependent on the functional elements of the separate parts (spatial relationship between planes σ_1-σ_2 and σ_3-σ_4) as well as the kinematic pair between σ_2 and σ_3.

After the functional elements and kinematic pairs of the dimensional chain have been identified, six virtual joints are associated with each of them to account for the possible six degrees of freedom in which the dimension or kinematic pair may change (see Figure 16). [17]

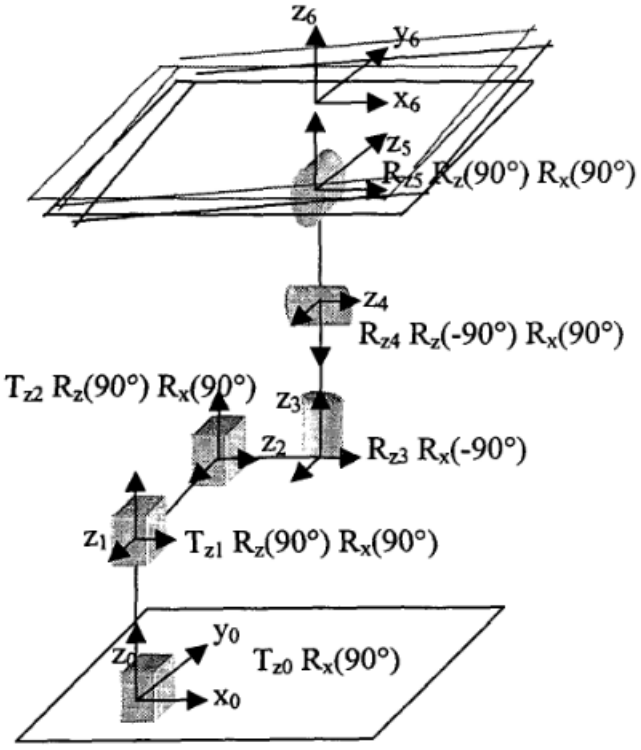

Figure 16. Virtual joints and coordinate frames in a functional element relationship between two planes of a part.

The relative position of the upper plane in respect to the lower plane in Figure 16 can be expressed with the homogenous 4x4-transformation matrix of the form:

$$T_0^6 = \begin{bmatrix} S(\Omega_3^4)C(\Omega_4^5)C(\Omega_5^6) + C(\Omega_3^4)S(\Omega_5^6) & S(\Omega_3^4)C(\Omega_4^5) & S(\Omega_3^4)C(\Omega_4^5)S(\Omega_5^6) - C(\Omega_3^4)C(\Omega_5^6) & D_2^3 \\ S(\Omega_3^4)S(\Omega_5^6) - C(\Omega_3^4)C(\Omega_4^5)C(\Omega_5^6) & -C(\Omega_3^4)S(\Omega_4^5) & -C(\Omega_3^4)C(\Omega_4^5)S(\Omega_5^6) - S(\Omega_3^4)C(\Omega_5^6) & -D_1^2 \\ -S(\Omega_4^5)C(\Omega_5^6) & C(\Omega_4^5) & -S(\Omega_4^5)S(\Omega_5^6) & D_0^1 \\ 0 & 0 & 0 & 1 \end{bmatrix},$$

where S and C represent sine and cosine, D_i^j the linear translation between frame i and j and Ω_i^j the rotational change between frame i and j [17].

Next, the small dispersions in the functional elements need to be associated with the translations of the functional requirement. This can be done by calculating the Jacobian matrixes associated with the transformation matrixes of each functional element, and multiplying them with vectors of the small dispersions:

$$\begin{bmatrix} \delta\vec{s} \\ \delta\vec{\alpha} \end{bmatrix} = [J_1 \quad J_2 \quad J_3 \quad J_4 \quad J_5 \quad J_6]_{FE_1} \dots [J_1 \quad J_2 \quad J_3 \quad J_4 \quad J_5 \quad J_6]_{FE_n} * \begin{bmatrix} \vec{\delta}_{FE\,1} \\ . \\ . \\ . \\ \vec{\delta}_{FE\,n} \end{bmatrix}.$$

$\delta\vec{s}$ and $\delta\vec{\alpha}$ are 3-vectors of the functional requirements translations and rotations, $[J_1 \quad . \quad . \quad . \quad J_6]_{FE_i}$ is a 6x6 Jacobian matrix associated with the *i*:th functional elements transformation matrix and $\vec{\delta}_{FE\,i}$ is a 6-vector of small dispersions of the *i*:th functional element. [17]

The Jacobian-based model has been previously implemented into CAT environments, although today the available software providers have moved on to parametric tolerance analysis because of its similarity to parametric modelling. The Jacobian-based model is also limited in that it cannot analyze complex network structures and transforming a tolerance on a drawing to a 6-vector of small dispersions requires expertise from the designer. However, the model does support both worst-case and statistical analysis and the individual tolerances are easily associated with the translations of the functional requirement because of the nature of the Jacobian matrixes. [17], [18]

2.3 Comparison of models

Table 2 shows a comparison between the analyzed tolerance methods. Tolerance charts and parametric analysis methods (mostly based on abstracted features) are the most widespread of the methods. This is because of the simplicity of the tolerance charts, and because the parametric methods are easy to integrate into CAD environments. [8]

Tolerance map is a rather new and promising method for tolerance analysis. It is the only "sophisticated" method, which can consider all geometric tolerances and conforms fully to the ISO and ASME standards. There are some efforts ongoing for integrating tolerance maps into a computer-aided environment. The vector loop and Jacobian-based models have not been integrated into any widely used CAD or CAT environments and thus, are not used extensively. [19]

Table 2. Comparison between the analyzed tolerance analysis methods.

	Dimensions	Scope of analysis	Tolerance types	Standard conformity	Automation	Ease of use
Tolerance Charts	1-D	worst-case only	dimensional & all geometric	full	manual / interactive	easy / hard
Parametric CATs	3-D	worst-case + statistical	dimensional & some geometric	partial	interactive	easy
Abstracted feature based CATs	3-D	worst-case + statistical	dimensional & some geometric	partial	interactive	medium
Vector loop	3-D	worst-case + statistical	dimensional & some geometric	partial	manual	hard
Tolerance map	3-D	worst-case + statistical	dimensional & all geometric	full	automated	easy / hard
Jacobian-based model	3-D	worst-case + statistical	dimensional & some geometric	partial	interactive	hard

As for the tolerance analysis of the TBPS support structure, a hybrid between the abstracted feature based model and vector-loop model was identified as the most suitable. The use of tolerance charts can be ruled out because it can only analyze the structures in one dimension at a time. The Jacobian-based approach would have been too cumbersome to perform manually for the support structure. Tolerance map remains a theoretical model for singular simple features, because a software has not been developed that utilizes it. Parametric tolerance analysis would have been a possible option if a suitable software were available. However, this approach would have relied on a known functional tolerance in the assembly, which in this case is the positional tolerance of the sensor modules, a quantity not known beforehand.

The abstracted feature based method used is described in the following chapters. Rather than forming the abstracted features based on a CAD model, the model was constructed by expressing sensor planes and particle trajectory lines in a 2-D / 3-D space. This approach was possible, because the trackers functional requirements were easily expressed with these abstract features and linked to the displacements of the sensors in the support structure. However, no statistical analysis of tolerances is possible with such a method because no tolerance chain is established. The vector-loop hybrid aspect of the model comes from the representation of particle trajectories as lines or vectors in space.

On the other hand, the lack of statistical analysis is not a concern because the tracker is a first-time-right production (built only once), so worst-case analysis is more suitable anyways. The next chapters will explain the construction of the model in detail, and how it was used for a tolerance synthesis.

3 TBPS tolerance synthesis

This chapter explains how the abstracted feature based model is created, and how it is used to allocate tolerances within the TBPS support structure. Section 3.1 describes the concept and mechanics of the silicon detector modules used in the TBPS. In section 3.2, the various coordinate systems of TBPS and individual modules are explained, as they are used extensively further on. Section 3.3 explains how the functional requirement of hermeticity poses limits on module displacements and finally, the following two sections explain how the functional requirements are interpreted to construct the model that is then used to allocate the tolerances for the TBPS structures.

3.1 Detector modules

One of the main functional requirements of the tracker's mechanics is to ensure hermeticity in the tracker's layers. This essentially comes down to properly positioning particle detector modules in the tracker volume. To understand how variation in the module positions affects tracking performance, it is essential to understand certain aspects of the modules themselves. For this purpose, an overview of basic mechanics is given related to the specific modules used in the TBPS. A concept called stub finding is also introduced, as it is quite essential to understand when we move on to describe the tracker hermeticity. This chapter ends by describing the geometry of the silicon sensors used in the modules.

3.1.1 Overview

The detector modules used in the TBPS section of the future CMS tracker are so called PS (pixel-strip) modules. The name originates from two types of silicon sensors used in

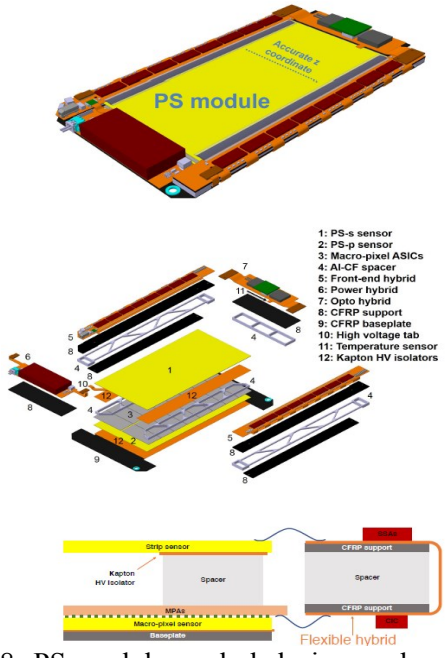

Figure 18. PS module exploded view and cross-section. The strips of the strip sensor are aligned along the line marked as "accurate z coordinate". [1]

the module: a strip sensor and a macro-pixel sensor as are shown in Figure 18. The strip sensor is located on the front-side of the module and is further on referred to as the front-sensor of a module.

Conversely, the macro-pixel sensor is located at the lower part of the module and is referred to as the back-sensor of a module. The two sensors are separated by spacers made of aluminum/carbon-fiber composite material that serves as a medium for heat transfer, and to provide an accurate mechanical gap between the two sensors. The PS modules come in three variants: 1.6 mm, 2.6 mm and 4.0 mm of spacing between the sensors. The spacing is specified between the sensors centers of gravity as shown in Figure 19. All of these three variants are used in the TBPS tilted section. [20]

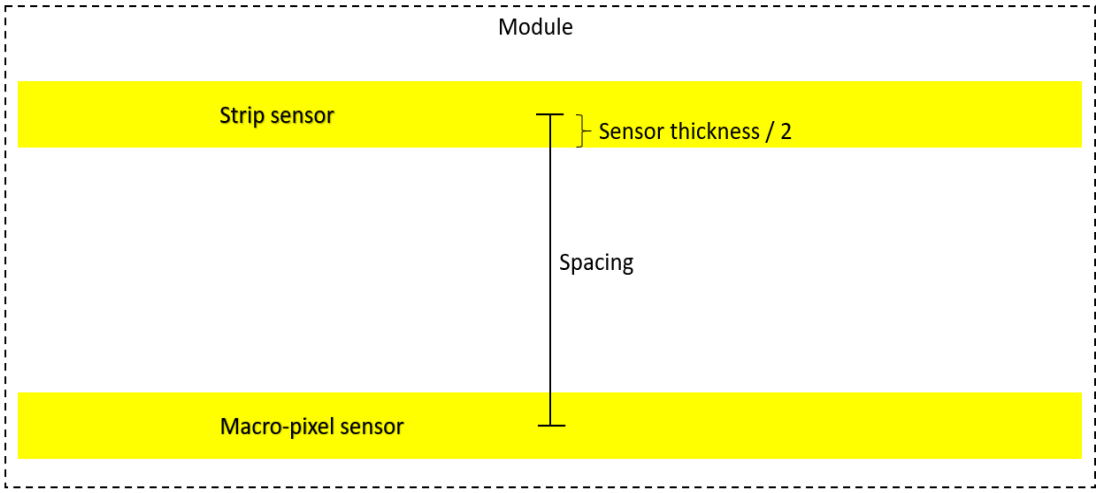

Figure 19. Cross-sectional illustration of the spacing between the two sensors of a PS module.

3.1.2 Stub finding

The reason for having two closely spaced sensors in a single module is to enable so-called stub finding. For physics studies, high momentum particles are searched while lowest momentum particles shall be rejected. Stub finding enables the detectors to disqualify hits

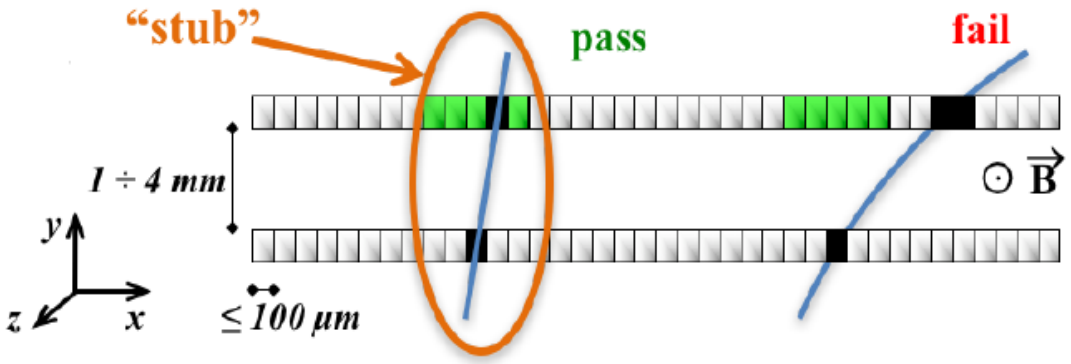

Figure 20. Stub finding principle in a module cross-sectional view. Trajectories of particles with low transverse momentum get bent more by the 3.8 T magnetic field, and fail to pass through the geometrical filter established between the superposed sensors. The pair of two successful hits make up a "stub" of a particle trajectory. [1]

of particles with low momentum. Stub finding also assists in the reconstruction of tracks, as the stubs contain easily distinguishable information of particle trajectory directions. The stub finding principle is illustrated in Figure 20. [20]

3.1.3 Sensor geometry

The sensors are encircled at their outer edges by a so-called bias ring, which is at ground potential. This bias ring is not an active hit-detecting element area, and as such must be excluded from the outer dimensions of the sensors in the analysis. We are primarily interested in the actual active area of the sensors as only those contribute to the tracker hermeticity that is discussed later in chapter 3.3. The sensor's physical (outer) dimensions and the dimensions of the active area are listed in Table 3.

Table 3. PS module sensors' physical (outer) dimensions and dimensions of the active areas. PS-s refers to the strip sensor of a PS module, and PS-p to the macro-pixel sensor. [1]

Sensor Name	Outer [µm]		Active [µm]	
	Width	Length	Width	Length
PS-s	98140	49160	96000	46944
PS-p	98740	49160	96000	46944

The active thickness of the two type of sensors is 200 µm. The physical thickness of the sensors is still under consideration, 200 µm is the target, but it may be that the sensors will be processed to thicker pieces of silicon. Thicker sensors are easier and cheaper to process, and the increased thickness may also increase the lifetime of the sensor, but more material in the tracker volume is not welcome for physics as it leads to a higher probability of particles interacting with matter. However, the final physical thickness of the sensors is not a relevant parameter for our tolerance analysis as it uses the active thickness as the reference. This is further explained in chapter 3.4.

3.2 Tracker and Module Coordinate Systems

Module displacements in the tracker volume are described further on by using either the modules local coordinate systems, or the trackers global coordinate system. In this section, these two coordinate systems are described.

3.2.1 Tracker Coordinate System and the TBPS geometry

CMS and the CMS tracker adopt a mixed use of Cartesian and cylindrical coordinate systems. The origin of the coordinate systems is in the interaction point (IP) of the LHC beam. The z-axis is along the beam, in counter-clockwise direction of the LHC tunnel and pointing towards the Jura mountain. The positive x-axis points towards the center of the LHC, and the positive y-axis upwards.

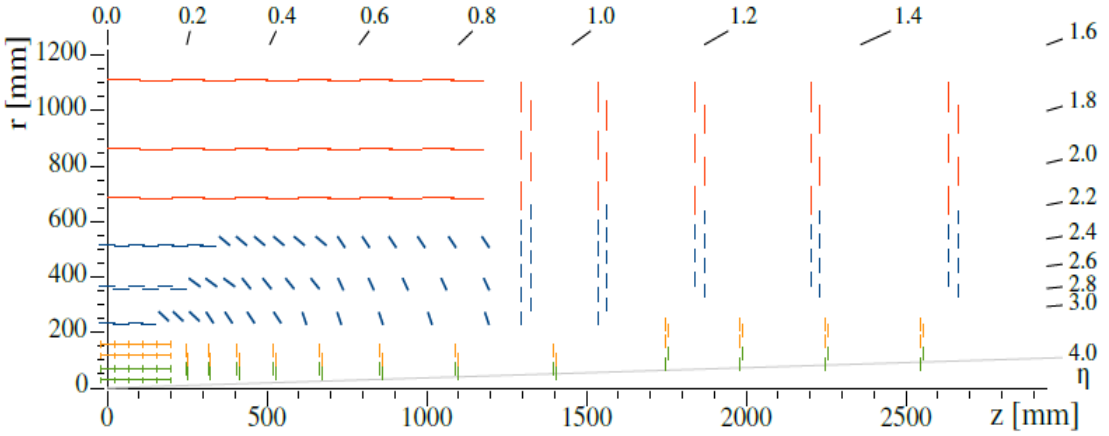

Figure 21. One quarter of the tracker in r-z view. Colored lines indicate individual modules. [1]

The LHC tunnel and the beam are slightly inclined from the true horizontal plane and CMS follows that inclined plane. Consequently, the z-axis of CMS is inclined by 1.23 %, sloping upwards in the positive z direction. Correspondingly, the y-axis is inclined by 1.23 % from the true vertical direction. The radial coordinate in the x-y plane is denoted as r (see Figure 21), and the azimuthal angle φ is measured from the positive x-axis in the x-y plane. In the figure, the TBPS section contains the (blue) modules from approximately 200 to- 600 mm in r, and from 0 to- 1250 mm in z. See Figure 22 for a complete overview of the TBPS and its tilted sections. A single ring assembly can be seen in Figure 24.

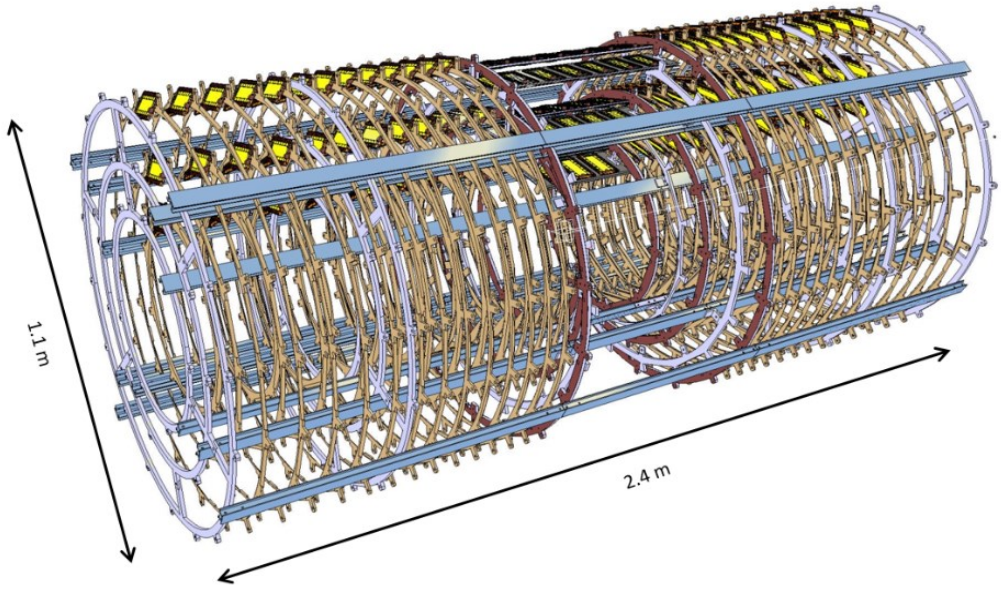

Figure 22. TBPS section of the CMS Tracker. [43]

There are eight ring variants in the tilted section: three types of rings with different module tilt angles in both layers 1 and 2, and two types of rings with different module tilt angles in layer 3. The first layer of the TBPS can be seen in Figure 23.

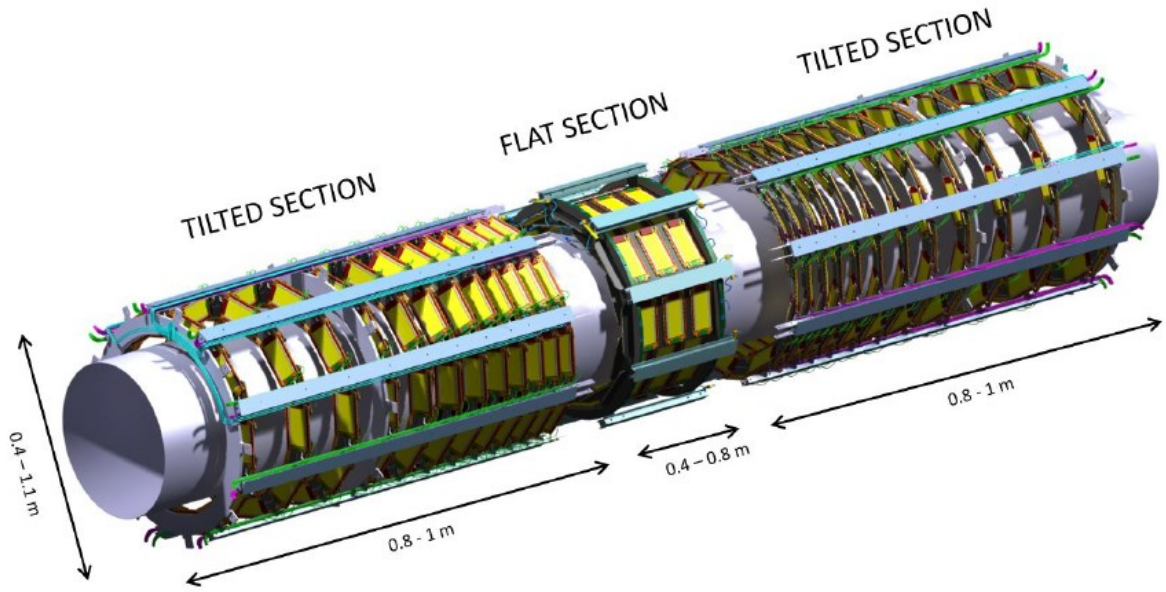

Figure 23. One layer of the TBPS section. Each of the three layers of the TBPS contain a central flat section, with modules fixed horizontally, and two tilted sections with modules inclined. [20]

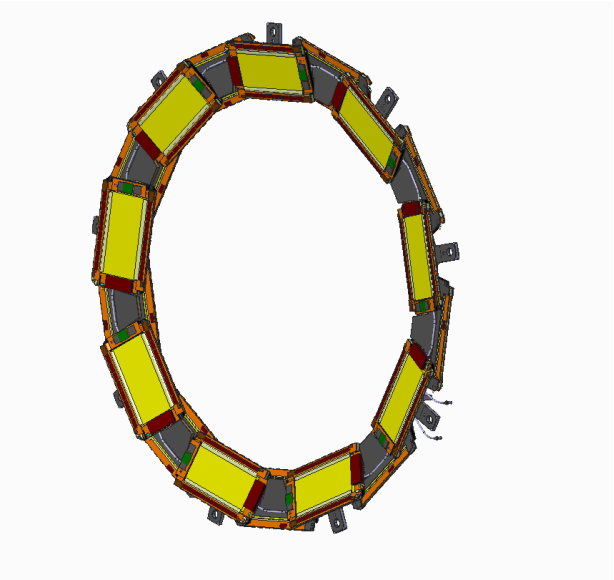

Figure 24. A ring of detector modules in the TBPS tilted section. Detector modules are attached on both sides of the ring support structure.

3.2.2 Module Coordinate System

Further along, we will discuss module's positions and their translational and rotational dimensions and their shifts. Dimensions are specified in the trackers global coordinate system described above, and in the modules local coordinate system. It is important to make a distinction between dimensions related to these two coordinate systems. Translational and rotational dimensions in a modules local coordinate system are described in Figure 25.

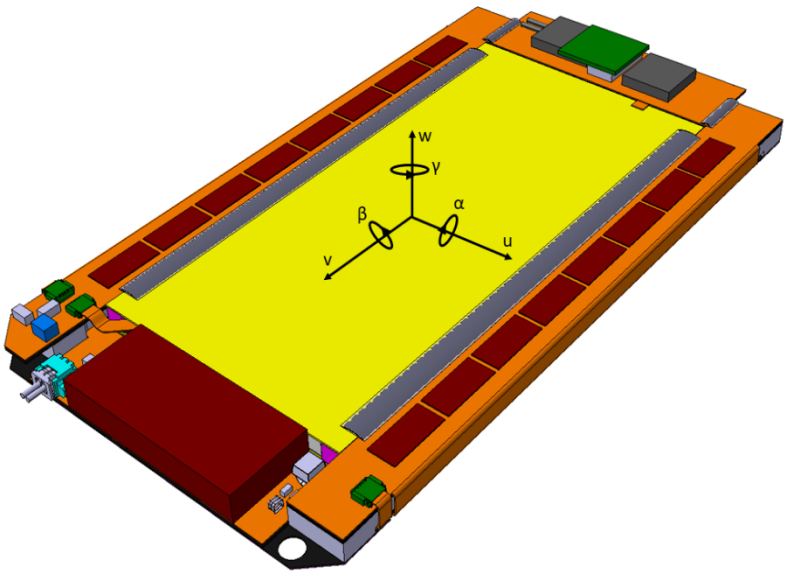

Figure 25. Module local coordinate system. The origin is specified at the center of a module, between the sensors. v-axis points towards the modules power hybrid, perpendicular to the orientation of the strips, u-axis is perpendicular to the v-axis, and points along the orientation of the strips. w-axis is perpendicular to both these axes, with the positive direction towards the strip sensor. Rotations around these axes are specified as α, β and γ as shown.

3.3 Tracker Hermeticity

For an efficient track reconstruction, the individual layers of detector modules must guarantee that particles passing them hit at least one of the active sensor areas on the modules. In addition, stub finding must be achieved so the hermeticity requirement actually dictates that a particle must hit both sensors of at least one of the modules in a layer.

To achieve this, the modules are arranged in layers such that the active areas of neighboring modules overlap each other (see Figure 27, Figure 28 and Figure 29). Furthermore, the proton-proton collisions do not occur at one single point along the beam-line, but rather form a normal distribution of possible collision points with the mean position being the interaction point (IP) as shown in Figure 26. The tracker shall be placed so that its geometrical center coincides with the IP.

The distribution along the z-axis (beam-line) is approximately 100 mm in both the positive and negative directions of the axis. However, retaining hermeticity for collisions in ±70 mm region has been set as the functional requirement of the tracker. The hermeticity requirement effectively translates into two overlap scenarios for the modules: z-coverage and φ-overlap. Both of these are discussed in more detail below.

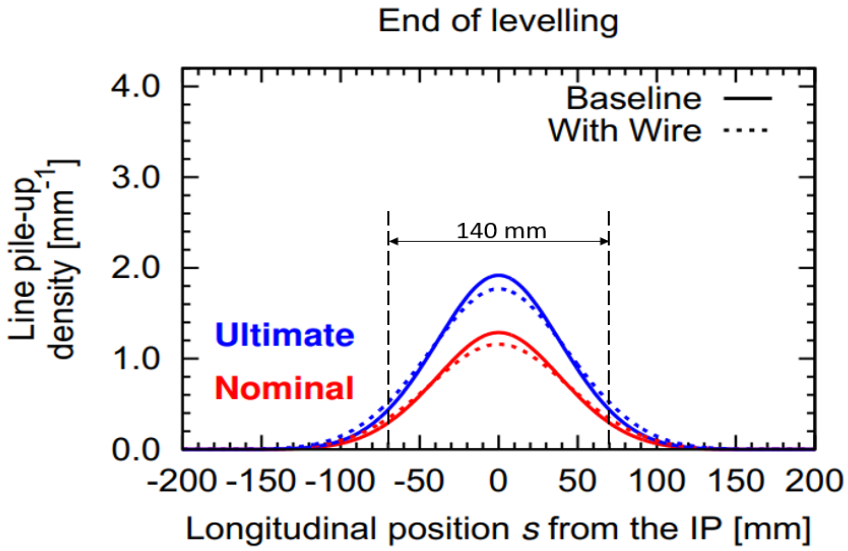

Figure 26. Distribution of interaction points along the z-axis. [47]

3.3.1 Z-coverage

The z-coverage requirement of 70 mm yields the maximum z-directional distances between the TBPS rings. Module positions in r and their tilt angles also have an effect on z-coverage. Due to the angle of particle trajectories in the y-z plane, the distance needs to be smaller at small z positions than between rings located at larger z positions. As such, the rings are arranged so that the distance between them increases incrementally along the z-axis to match with the needed space coverage.

The z-coverage also results in a dimension called z-overlap for the modules, as shown in Figure 27. This dimension describes a region on the successive modules where a particle is guaranteed to hit at least two modules within a layer.

The z-overlap and the z-coverage are values that depend on the positional relationship of two successive rings. Thus, their values differ according to the ring and layer under analysis.

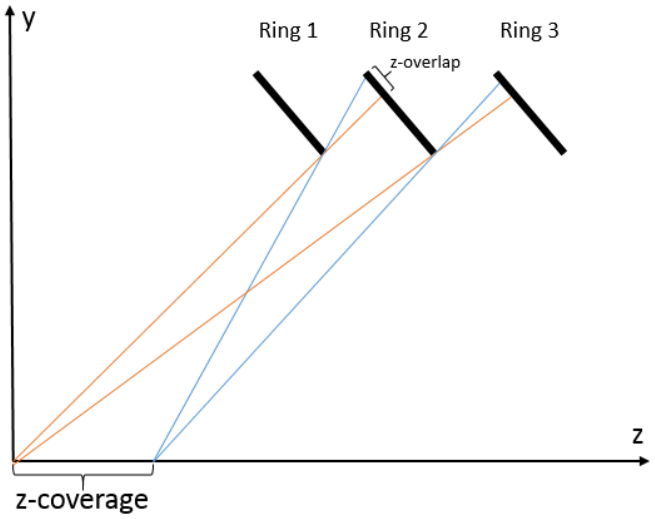

Figure 27. Module overlap in the y-z plane. Notice that the overlap exists for the range of z-coverage. Straight tracks generated by collisions at the interaction point (z = 0) are displayed by orange lines, and particles from a collision at z = z-coverage by blue lines.

The hermeticity of the tracker is affected by z-coverage and z-overlap. However, the design requirement of z-coverage has been set at ± 70 mm and providing better coverage would offer only marginal benefits for the hermeticity while such increased coverage would unavoidably lead to needing more modules, hence more mass, for the same overall space coverage. In addition to the hermeticity, the z-overlap is also important for the tracker's software calibration and alignment algorithms that use tracks that hit successive modules in the same layer. Such overlapping hits help to constrain and validate the layers' final geometry. [21]

Each TBPS layer (Figure 23) contains 12 tilted rings at each end. This configuration results in nominal z-coverages listed in Table 4 and Table 5. The modules on the two sides of each ring are at different radial positions. Hence, z-coverage is displayed for the inner and outer modules.

Table 4. Outer module's z-coverage for each ring of the TBPS tilted section and for the three layers. Note that z-coverage is specified between rings, and in the table the given coverage refers to the value between ring i and i-1. The value given for ring 1 indicates the coverage between the end modules in the TBPS flat section and the modules in the ring 1.

Outer z-coverage (ring i & i-1) [mm]												
Ring	1	2	3	4	5	6	7	8	9	10	11	12
Layer 1	64.59	94.98	100.01	118.83	119.73	120.39	121.00	125.30	128.16	131.38	150.40	174.67
Layer 2	82.10	89.24	99.67	96.61	94.49	98.90	102.46	98.44	99.66	103.90	106.45	117.67
Layer 3	65.60	68.73	70.22	69.63	73.16	75.57	76.93	70.45	70.49	74.89	77.03	79.11

Table 5. Inner module's z-coverage in TBPS tilted section.

Inner z-coverage (ring i & i-1) [mm]												
Ring	1	2	3	4	5	6	7	8	9	10	11	12
Layer 1	131.72	90.55	97.688	147.13	116.96	120.07	123.60	172.80	128.85	134.82	156.74	184.36
Layer 2	191.85	88.93	100.83	153.72	94.42	100.34	105.58	150.94	101.14	107.17	111.78	125.14
Layer 3	246.42	67.99	70.68	71.41	76.25	80.09	174.19	71.55	72.80	78.44	81.96	85.52

The variation in module position in z and r are a result of variation in the manufacturing and assembly of the individual rings, as well as the variation in placing the rings within a layer. As can be seen in Table 4 and Table 5, the nominal z-coverage is close to (or under) the required 70 mm between the flat section and the first rings of the tilted section in all three layers when the outer modules are inspected. Furthermore, in layer 3 the z-coverages are close to their limit or under it throughout the rings. To reach a full match with the 70 mm target a 13th ring would be necessary on layer 3, but this would lead to a huge complication in the cabling on that layer as the cabling multiplicity is 12.

In addition to the z-coverage requirement depicted in Figure 27, the more stringent requirement of coverage for module stub finding must also be retained, as explained in 3.1.2 .

3.3.2 φ-overlap

In layer 1, the modules on the rings are positioned at an azimuthal angle of φ=20° from each other. This angle is approximately 13.8° in layer 2, and 10° in layer 3. The edges of the modules overlap each other in φ as shown in Figure 28 and Figure 29.

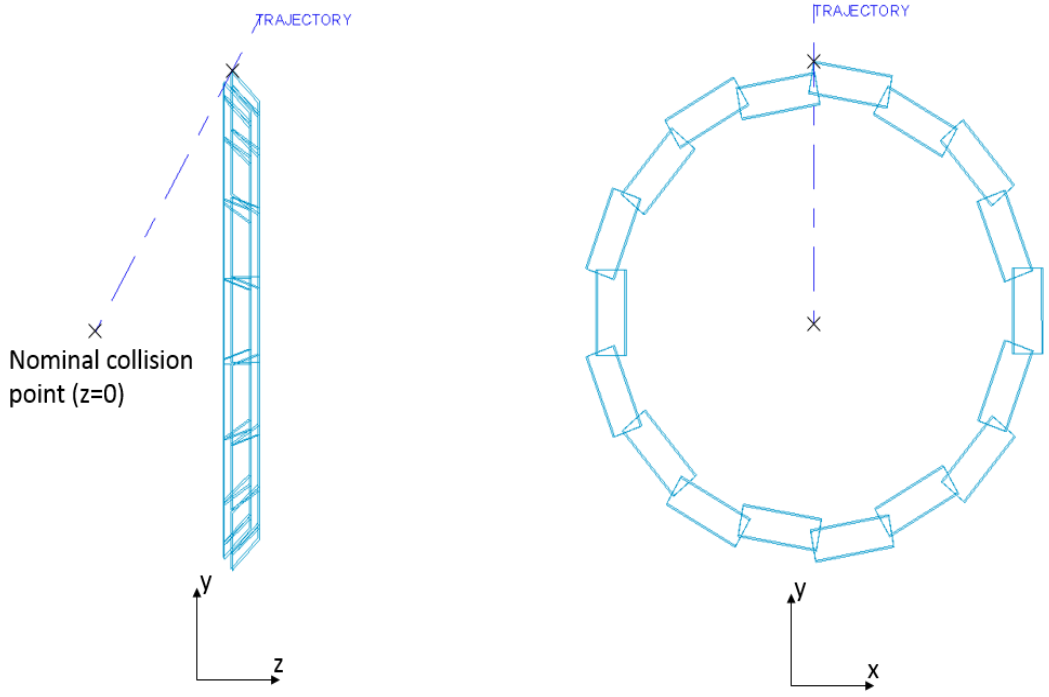

Figure 28. TBPS ring sensor display with a trajectory towards the φ-overlap region.

φ-overlap is a quantity that is defined for actual trajectories. Because of this, it cannot be depicted in any of the coordinate system planes that are shown in Figure 28. Rather, we have to display the ring in a plane that is normal to a particle trajectory to get a more realistic view of the φ-overlap region (see Figure 29). It is essential to first define a trajectory that would correspond to the "worst-case" in terms of φ-overlap. An example of such a trajectory is shown in Figure 28.

Z-overlap affects the sensors on their higher (and lower) r edges, and essentially guarantees that a particle will hit a module in a layer if it traverses towards this region (the particle will hit a module on a ring i-1 if i is the ring analyzed). This affects φ-overlap such that the actual φ-overlap value is not measured at the corners of the sensors, but it can rather be measured from a region at smaller r, the value of which depends on the magnitude of z-overlap on the module. This topic is covered more thoroughly in section 3.5, and in Figure 28 and Figure 29.

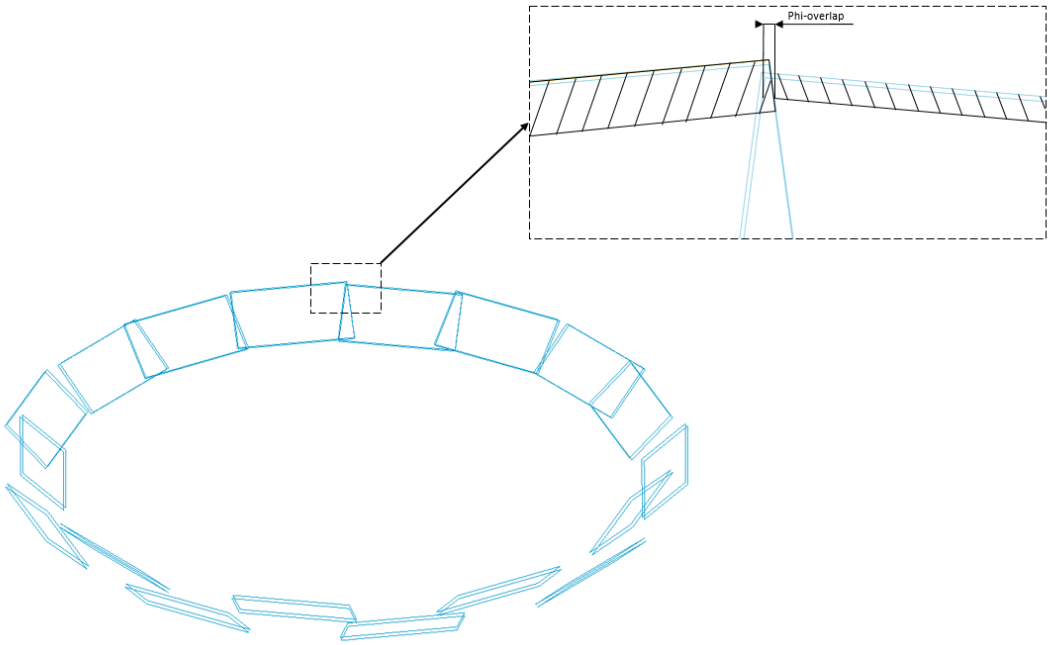

Figure 29. View along the trajectory shown in Figure 28. Hatch-filled areas on the detailed view represent the z-overlap areas of the modules. The φ-overlap is not measured at the very corner of the sensor, but rather at the location where the z-overlap ends.

In the next chapter, we analyze the sensitivities of the overlap scenarios to variations in module positions, and allocate tolerances for module positional shifts based on the sensitivity analysis. Z-coverage is analyzed in terms of its sensitivity to ring translational variation in z and r, and rotational variation of the tilt angle. φ-overlap sensitivity is determined by the effect of variations in all six degrees of freedom (x, y, z and revolutions around these axes).

3.4 Tolerance allocation based on z-coverage and z-overlap

We can express z-coverage mathematically by figuring out a line, which represents a particle trajectory that just fulfills the stub finding requirement (hit in both sensors of a module) as described above. We can then solve the z-value where this line intersects with the z-axis, giving us the z-coverage between the two modules. For example, in Figure 30, such trajectory is depicted by a line that crosses points 1 and 4.

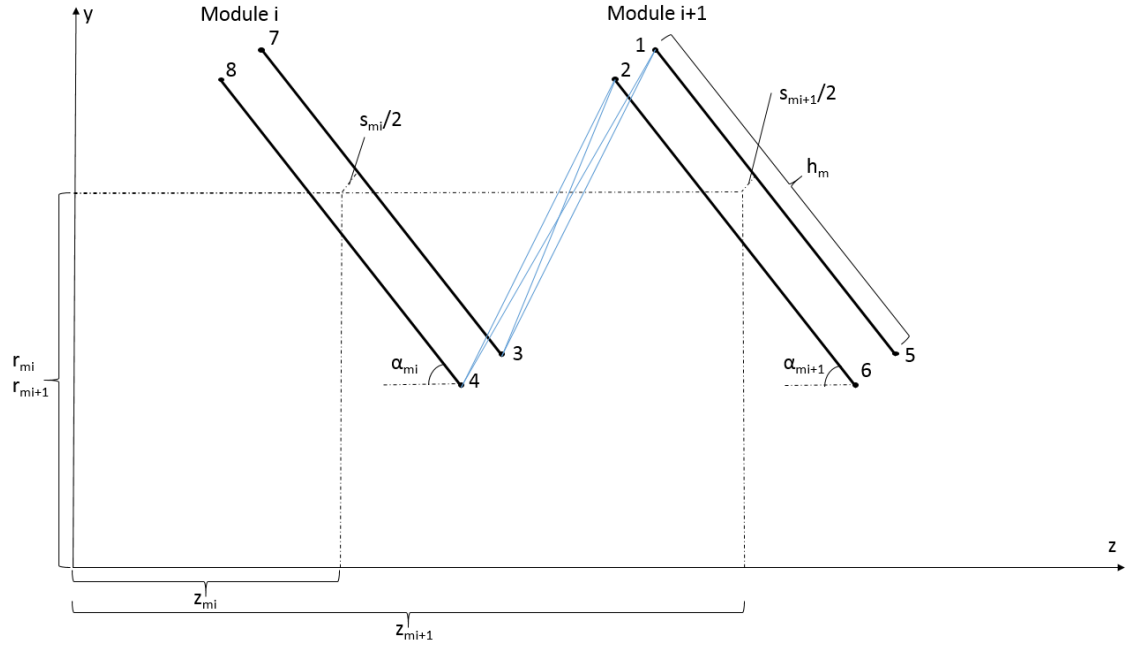

Figure 30. Schematic view of z-coverage between two modules located in two successive TBPS rings. Each black line depicts a sensor. Particle trajectories must hit both sensors on a module to enable stub finding. r_m = module position in y, z_m = module position in z, α_m = module tilt angle & s_m = module sensor spacing.

The possible trajectories are lines that traverse through points 1-3, 1-4, 2-3 or 2-4 (blue lines in Figure 30). For each module pair, these four lines are expressed mathematically, along with lines that correspond to the sensors (lines from point 1 to 5 and so on…). The trajectory lines and sensor lines intersections are then calculated, and the line that fulfills the stub finding requirement is chosen. See Appendix A for a more detailed mathematical explanation.

3.4.1 Sensitivity analysis

Sensitivity analysis is the study of how variation in a model's output varies with input variation. It can be utilized for several different purposes, but the goal of the analysis in this section is to evaluate how much the variations of each module positional values (here referred to as "dimensions" that are z, r and tilt angle) contribute to the end z-coverage between modules. [22]

The correlation is calculated using the Pearson's linear correlation coefficient:

$$rho_{X,Y} = \frac{\sum_{i=1}^{n}(X_i - \bar{X})(Y_i - \bar{Y})}{\{\sum_{i=1}^{n}(X_i - \bar{X})^2 \ \sum_{j=1}^{n}(Y_i - \bar{Y})^2\}},$$

where X is a column vector of the changes applied to the dimensions in the model, and Y is a column vector of results (z-coverages) with those changes applied. $\bar{X}$ and $\bar{Y}$ correspond to the mean values of these vectors. Rho is a value between -1 and 1 that describes the correlation between vector X and Y, with -1 being perfect negative correlation and 1 being perfect positive correlation. As we are not interested whether the correlation was positive or negative, the absolute value of the result is used.

To achieve reliable results, the correlations have been calculated for each ring from 500 000 different combinations of dimensional changes and results. Pearson's linear correlation coefficient can be used, because correlation between z-coverage and the parameters is linear; see Appendix B for clarification. [23]

As a result, we are primarily interested in finding out which dimensions contribute the most (or least) to z-coverage for each ring. As such, it is reasonable to select the same variation limits for z and r. As the tilt angle cannot be related to those two measures, we must simply choose variation limits that seem reasonable from the higher end of possible variation. For this analysis, variations of ±1 mm were used for module z and r positions, and ±1° for tilt angle variation. The analysis was carried out on the outer modules in rings, as they determine tighter tolerance values than the inner modules, as explained before. The results for each layer are depicted in Figure 31, Figure 32 and Figure 33.

An individual z-coverage value is a result of module positional shifts in two rings. Therefore, the correlation magnitudes depicted for each ring are a result of values associated with two successive rings. Because of this, correlation magnitudes exceed 1 in certain rings.

As can be seen from the results, z-coverage is predominantly determined by the module positions z and r. z variations seem to have a larger effect in rings closer to the interaction point (IP), while variation in r plays the more dominant role in rings that are

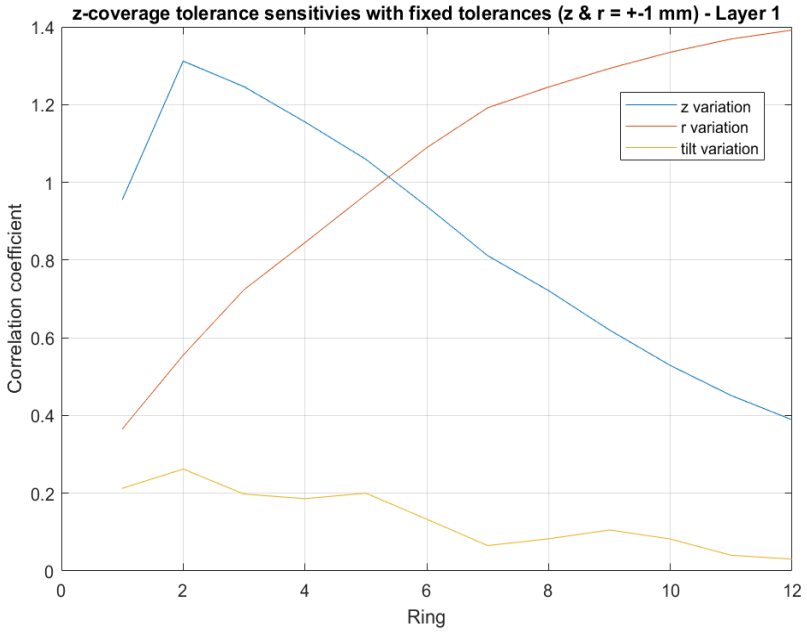

Figure 31. Influence of z, r and tilt variation on z-coverage in layer 1.

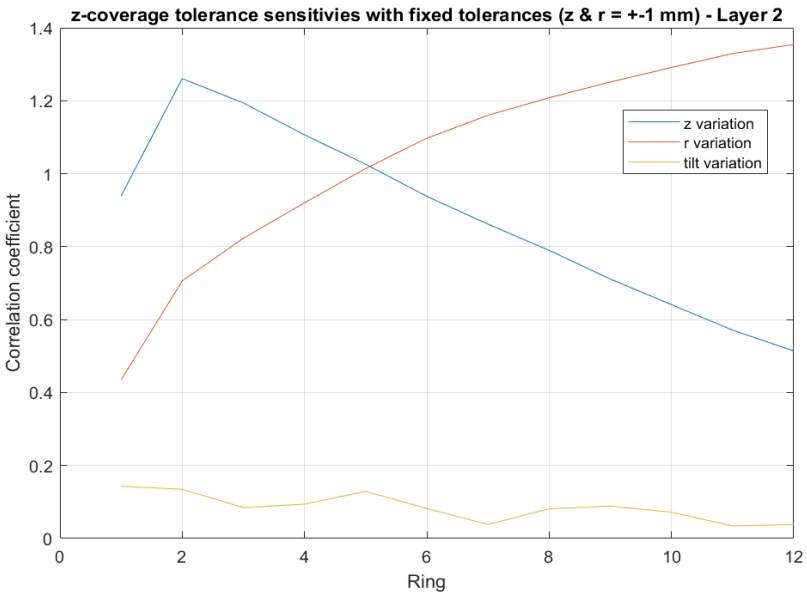

Figure 32. Influence of z, r and tilt variation on z-coverage in layer 2.

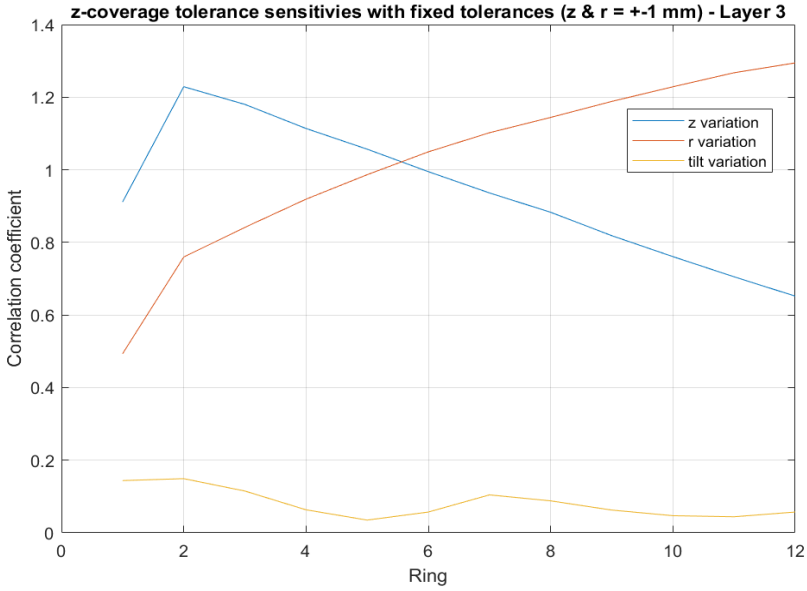

Figure 33. Influence of z, r and tilt variation on z-coverage in layer 3.

located the furthest from the IP. In addition, the ratio of z and r variations influence seems to change quite linearly across a single layer in the tilted section, with both variations having a similar influence in ring 5 of all layers.

The main difference between the layers is that in layer 1, the ratio of z and r variations influence in ring 1 and 12 is higher, while in layer 3 the z-coverage is impacted more evenly by both of these variations across the rings.

The ±1° tilt angle variation has the smallest influence on z-coverage: the influence is at its highest in layer 1, where the correlation coefficient peaks at 0.25. This correlation seems to decrease at higher z values in all layers, with minor increases at rings where the nominal module tilt angle changes.

As this analysis was focused on the tilted section, no dimensional variation was introduced into the modules in the flat section. This results in the seemingly odd behavior of ring 1 in all layers, as the input correlation to the output is calculated only from the dimensional variation of the modules in the tilted ring and the flat section is considered "perfect".

These results are used to synthesize tolerances based on the functional requirement of z-coverage. The directional / angular sensitivity magnitudes dictate the order of perturbation, which is used to synthesize the tolerances. This perturbation -based method is described in detail in the next section.

3.4.2 Tolerance synthesis

Tolerance calculation of the module positions in the abstracted feature model is based on perturbation: the position or orientation of two consecutive modules is incrementally shifted in the model, so that the z-coverage decreases between them. When the z-coverage reaches the functional requirement of 70 mm, the amount of displacement introduced to the position / orientation of the modules is saved, nominal module positions returned to the model and the process restarted between the next modules.

This method results in maximum tolerances for module displacements in the direction / orientation in which they were perturbed. The result corresponds to the assumption that the other dimensions affecting z-coverage are at their nominal values. For example, the perturbation can be started in the z-direction, which results in module positional tolerances in z, with the assumption that r and tilt angle values are at their nominal values. This does not correspond to the reality, because some amount of tolerance must be allowed in all of the directions / orientations that affect the functional requirement.

To account for tolerances in more than only one dimension, the tolerance value achieved initially can be multiplied with an arbitrarily chosen value between 0-1, decreasing the maximum value, and then that value implemented into the model as module positional shifts. This essentially creates some "space" to allocate tolerances in other directions / orientations. The perturbation must be carried out in the order of the tolerance sensitivity magnitudes. This is to achieve reasonable tolerances in all directions. For example, if the perturbation for z-coverage were started with tilt-angle shifts, the end tolerance for tilt-angle would be huge as its correlation coefficient with z-coverage is small. Consequently, the tolerance results in z and r would be miniscule.

Based on the sensitivity analysis, the order of perturbation for z-coverage tolerance synthesis is z, r and finally tilt-angle. The distinction between whether to start the perturbation in z or r is not clear based on their sensitivity magnitudes, but it is reasonable to allow the z tolerances to be higher, because of the way the layers are assembled. However, this does result in quite small tolerances in r in rings where z-coverage was most sensitive to changes in r. This is because the z-tolerance perturbed first "eats" most of the available tolerance space. The perturbation method is illustrated in Figure 34.

In this analysis, the maximum z-tolerances were multiplied by 0.35 and the resulting r-tolerances by 0.6. These values were chosen primarily by trial and error, by looking at the end tolerance results and adjusting the ratios accordingly.

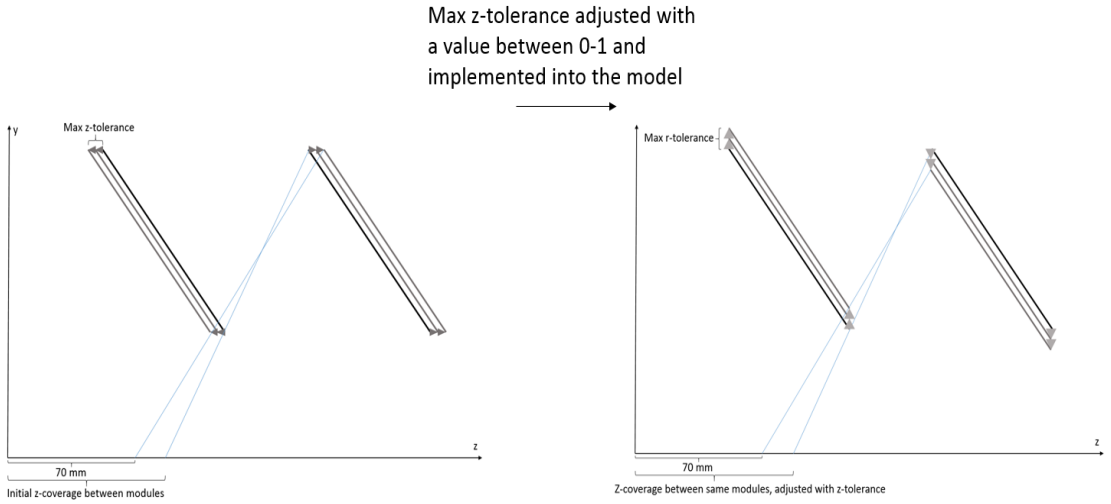

Figure 34. Illustration of the perturbation method. The method would continue with the perturbation of the module tilt-angles.

Individual module translational variation is mostly a result of variation that originates from attaching the rings together, rather than from tolerances associated with assembling the ring itself. As such, if we assume module positional tolerances to be equal to ring positional tolerances, we are uninterested in both the inner and outer module tolerances, just in the one that is smaller. This results in tolerances that are associated with translational positioning of a ring.

The results for z, r and tilt-angle tolerances for each layer are listed in Table 6. For each layer, the inner and outer tolerances were compared, and the one with smaller values selected. See Appendix A for tables with all the individual tolerance values, as well as for a more thorough mathematical explanation of the model.

As can be seen, the positioning tolerances of the first ring are very small across the layers. Furthermore, the translational tolerances of the rings in layer 3 are just few tens of microns in most rings, and even lower than 10 µm in some rings. These values indicate that considerable care has to be taken when attaching the tilted sections to the flat sections, and that layer 3 cannot fulfill the 70 mm coverage requirement with the current geometry.

Tolerances in rings 2-12 in layer 1 are quite large with values exceeding ±1 mm in most cases, and even being as high as 5 mm in a single direction. In fact, successful mechanical assembly of a tilted section is likely to require tighter tolerances than those. That would imply that in the case of rings 2-12 in layer 1, the tolerances should be primarily derived from the mechanical assembly constraints and clearances, rather than the functional “physics” requirements of the tracker.

Table 6. TBPS tilted section ring translational tolerances in z & r and module tilt angle tolerance. Tolerances were calculated with a positional shift increment of 5 μm or rotational shift increment of 0.005 degrees. Note that the scope of this analysis excludes dimensions not related to the TBPS. Thus, certain positional tolerances in the last ring of the tilted section are shown as zero. Values marked as zero in other rings indicate that the tolerance is < 0.005 mm in that ring.

Ring	1	2	3	4	5	6	7	8	9	10	11	12
Ring r & z translational tolerances and module tilt angle tolerances - layer 1												
z-tolerance												
+	0,000	0,599	0,718	0,964	1,435	1,454	1,276	1,405	1,855	1,957	2,417	3,177
-	0,599	0,718	0,964	1,435	1,454	1,276	1,405	1,855	1,957	2,417	3,177	0,000
r-tolerance												
+	1,308	1,161	1,206	1,446	1,197	0,864	0,786	0,867	0,765	0,789	0,873	0,000
-	0,000	1,308	1,161	1,206	1,446	1,197	0,864	0,786	0,867	0,765	0,789	0,873
Tilt angle tolerance												
+	0,425	0,475	0,565	0,525	0,520	0,495	0,570	0,505	0,495	0,495	0,490	0,000
-	0,000	0,425	0,475	0,565	0,525	0,520	0,495	0,570	0,505	0,495	0,495	0,490
Ring r & z translational tolerances and module tilt angle tolerances - layer 2												
z-tolerance												
+	0,369	0,282	0,313	0,340	0,452	0,459	0,553	0,499	0,621	0,709	0,704	0,929
-	0,282	0,313	0,340	0,452	0,459	0,553	0,499	0,621	0,709	0,704	0,929	0,000
r-tolerance												
+	0,519	0,471	0,423	0,477	0,414	0,432	0,339	0,369	0,369	0,321	0,375	0,000
-	0,864	0,519	0,471	0,423	0,477	0,414	0,432	0,339	0,369	0,369	0,321	0,375
Tilt angle tolerance												
+	0,390	0,385	0,495	0,395	0,400	0,405	0,485	0,395	0,400	0,395	0,385	0,000
-	0,605	0,390	0,385	0,495	0,395	0,400	0,405	0,485	0,395	0,400	0,395	0,385
Ring r & z translational tolerances and module tilt angle tolerances - layer 3												
z-tolerance												
+	0,000	0,000	0,005	0,000	0,016	0,058	0,072	0,009	0,009	0,026	0,095	0,121
-	0,000	0,005	0,000	0,016	0,058	0,072	0,009	0,009	0,026	0,095	0,121	0,000
r-tolerance												
+	0,000	0,006	0,000	0,018	0,063	0,066	0,009	0,009	0,021	0,060	0,069	0,000
-	0,000	0,000	0,006	0,000	0,018	0,063	0,066	0,009	0,009	0,021	0,060	0,069
Tilt angle tolerance												
+	0,000	0,070	0,000	0,185	0,235	0,425	0,175	0,150	0,200	0,245	0,250	0,000
-	0,000	0,000	0,070	0,000	0,185	0,235	0,425	0,175	0,150	0,200	0,245	0,250

Tilt angle tolerances are quite stringent in all layers with values in the range of ±0.3 degrees, but they should still be achievable. Figuring out a solution for layer 3 is outside the scope of this analysis, but one option could be to lower the 70 mm coverage

requirement to 65 mm in the case of layer 3. The results in such arrangement are listed in Table 7.

Table 7. Ring r & z translational tolerances and module tilt angle tolerances in layer 3 with z-coverage requirement set to 65 mm.

Ring r & z translational tolerances and module tilt angle tolerances - layer 3 with a z-coverage requirement of 65 mm												
z-tolerance												
+	0,016	0,044	0,061	0,054	0,072	0,109	0,121	0,079	0,079	0,096	0,159	0,186
-	0,044	0,061	0,054	0,072	0,109	0,121	0,079	0,079	0,096	0,159	0,186	0,000
r-tolerance												
+	0,078	0,093	0,072	0,084	0,114	0,114	0,066	0,060	0,066	0,099	0,105	0,000
-	0,027	0,078	0,093	0,072	0,084	0,114	0,114	0,066	0,060	0,066	0,099	0,105
Tilt angle tolerance												
+	0,225	0,245	0,250	0,260	0,280	0,440	0,255	0,250	0,260	0,285	0,280	0,000
-	0,580	0,225	0,245	0,250	0,260	0,280	0,440	0,255	0,250	0,260	0,285	0,280

As can be seen, translational tolerance values range then from 10 μm to 200 μm. While the values obtained remain still too small in certain rings, this 65 mm example shows how much lowering the z-coverage requirement affects the results.

It is important to keep in mind that the ratios between these tolerance values are based on estimates of what is easy to do and what is not. Once a prototype of the tilted section is realized and measured, this analysis can be adjusted according to the results obtained. For example, translational tolerances in r might be tightened to allow higher tolerances for module tilt angles.

3.5 Tolerance calculation based on φ-overlap

In section 3.3.2 , it was mentioned that z-overlap had an effect on φ-overlap. This is illustrated more clearly in Figure 35, where the z-overlap regions are marked with orange lines. We can consider the sector between the sensor's edge and the orange line to be a zone that does not need to be consider when calculating the φ-overlap. This is because all particles that hit the sensors in those regions have already hit a module in the previous ring. Z-overlap is generally smaller in outer modules, and as such, we apply that overlap value to both of the two consecutive modules (in Figure 35) in the analysis.

This methodology is subject to a simplification regarding z-overlap: the actual z-overlap region is larger than what is depicted in Figure 35. If we imagine the region as a shadow cast by the modules on a previous ring in the layer, one can easily imagine that the shadow should be larger on the ring under inspection than what is depicted in Figure 35. This is illustrated in Figure 36.

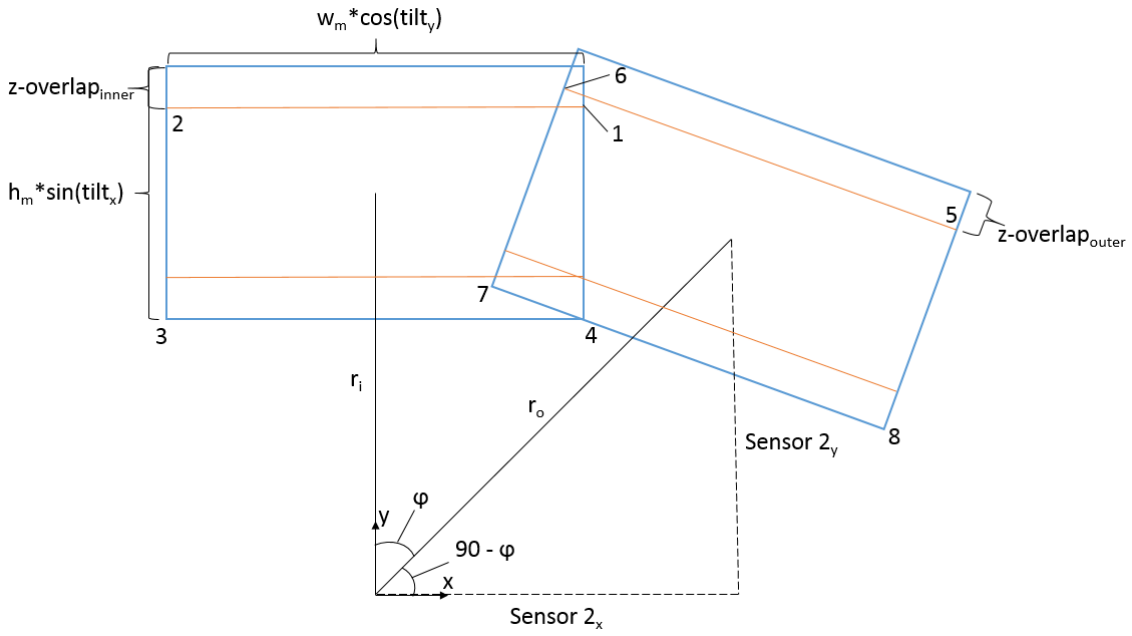

Figure 35. General view of two consecutive modules in a ring. w_m is the width of a sensors active area, h_m the height of a sensors active area, r_i the inner modules position in r, r_o the outer modules position in r, $tilt_x$ the sensors rotation around the x axis (tilt angle) and $tilt_y$ the sensors rotation around the y-axis. Note that proportions are warped for illustration purposes: line r_o is actually perpendicular to lower edge of the outer sensor.

As can be seen, the location where the modeled trajectories intersect these sensors is already covered by z-overlap. This leads to slightly smaller tolerance values regarding φ-overlap than what would be simulated with a perfect model.

The sensors depicted in Figure 35 are the ones on the modules that are further away in z. This means the back-sensor in the left module, and the front-sensor in the right module (in the view of Figure 35, the left module is facing the viewer that looks along the particle tracks, while the module on the right is attached on the back side of the ring, and thus is facing away from the viewer). A particle that is travelling towards the φ-overlap region in Figure 35 is guaranteed to hit the sensors that are at lower z, if they hit the sensors depicted.

There are two options for critical trajectories for calculating φ-overlap. Either a trajectory from the nominal collision position to point 1 in Figure 35, or then a trajectory from the nominal collision position to point 6 in Figure 35. This methodology is subject to the simplification that we only consider trajectories that originate from collisions at the nominal z=0 position on the beam-line. Indeed, with the current geometry, there are rings in the tilted section where φ-overlap is negative for particles that originate from collisions in larger z values, at the outer peripheries of the collision zone.

The φ-overlap is calculated by figuring out the point where a trajectory from the IP to point 6 intersects the plane of the left sensor, or a point where trajectory from the IP to point 1 intersects the plane of the right sensor. The intersection point's distance in the x-direction from a line that represents the edge of a sensor is the φ-overlap.

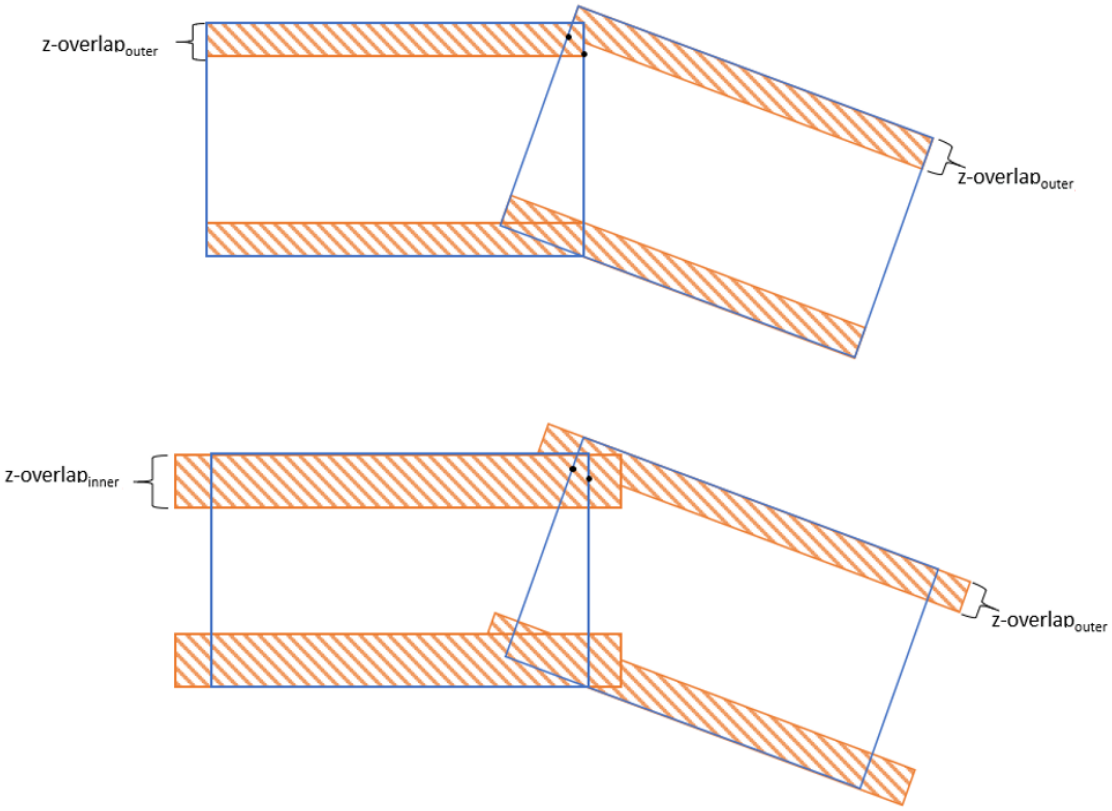

Figure 36. Illustration of how z-overlap is considered in the model (top), and how it would look like in reality (bottom). The locations of points 1 and 6 are depicted as black dots.

This results in two values for the φ-overlap: the one calculated from a trajectory from the IP to point 6, and one that is calculated from a trajectory from the IP to point 1. The smaller of these will be the value for φ-overlap that we use.

The analysis demonstrated here is an example for calculating the φ-overlap magnitude from a trajectory that crosses point 6. The method for a trajectory to point 1 is not demonstrated, as it is virtually the same in terms of methods used.

The analysis begins by figuring out the coordinates of points 1, 2, 4, and 6 in z, x and y (see Appendix B for the description of how the coordinates of the points are formed). After this, we can form a vector from the origin to point 6, and a vector from origin to point 1 which are of the form:

$$l_{0-6} = [t * p6_x, t * p6_y, t * p6_z]$$

We can describe the left sensor as a plane that forms from vectors from point 1 to 2 and from point 1 to 4:

$$l_{1-2} = [p2_x - p1_x, p2_y - p1_y, p2_z - p1_z]$$

$$l_{1-4} = [p4_x - p1_x, p4_y - p1_y, p4_z - p1_z]$$

The cross product of these two vectors will give us the normal vector N of the plane. Thus, the equation of the plane is:

$$N_1(x - p1_x) + N_2(y - p1_y) + N_3(z - p1_z) = 0$$

To this, we can substitute the x, y, and z values from l_{0-6}:

$$x = t * p6_x$$

$$y = t * p6_y$$

$$z = t * p6_z$$

When we solve the equation for t, we can substitute that value to l_{0-6}, which gives us the coordinates of the intersection point. The x-coordinate of the intersection point is then subtracted from $p1_x$.

3.5.1 Sensitivity analysis

The results of the sensitivity analysis regarding φ-overlap are displayed in Figure 38, Figure 39 and Figure 40. Explanations of the variation directions and orientations are displayed in Figure 37.

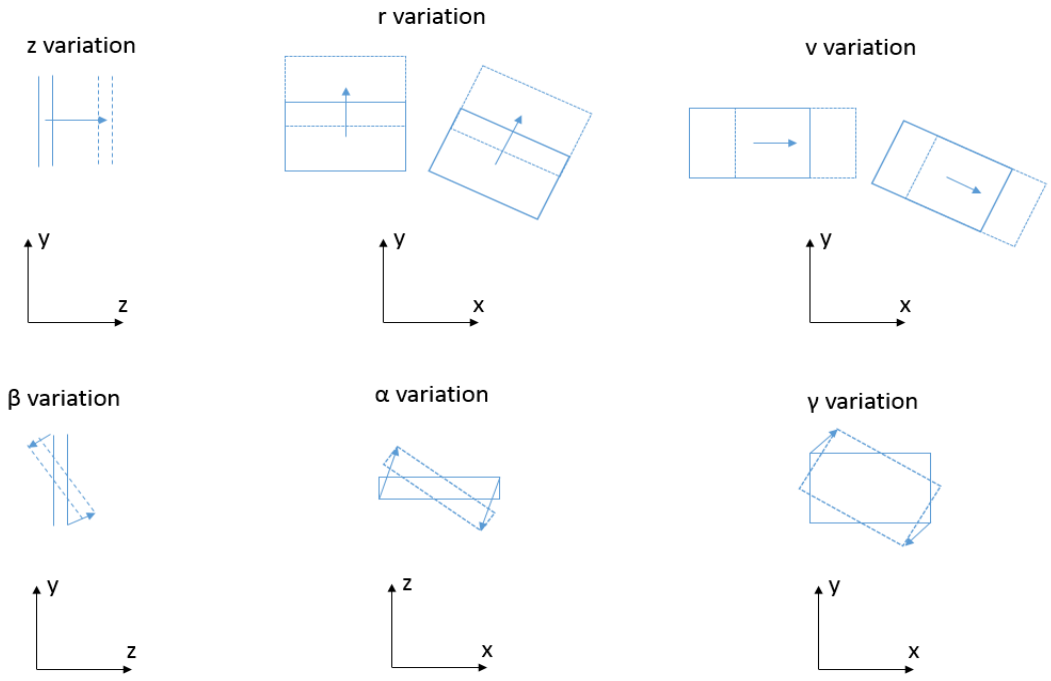

Figure 37. Illustration of the dimensional parameters to which variation is introduced. See chapter 3.2 for and explanation of the coordinate systems.

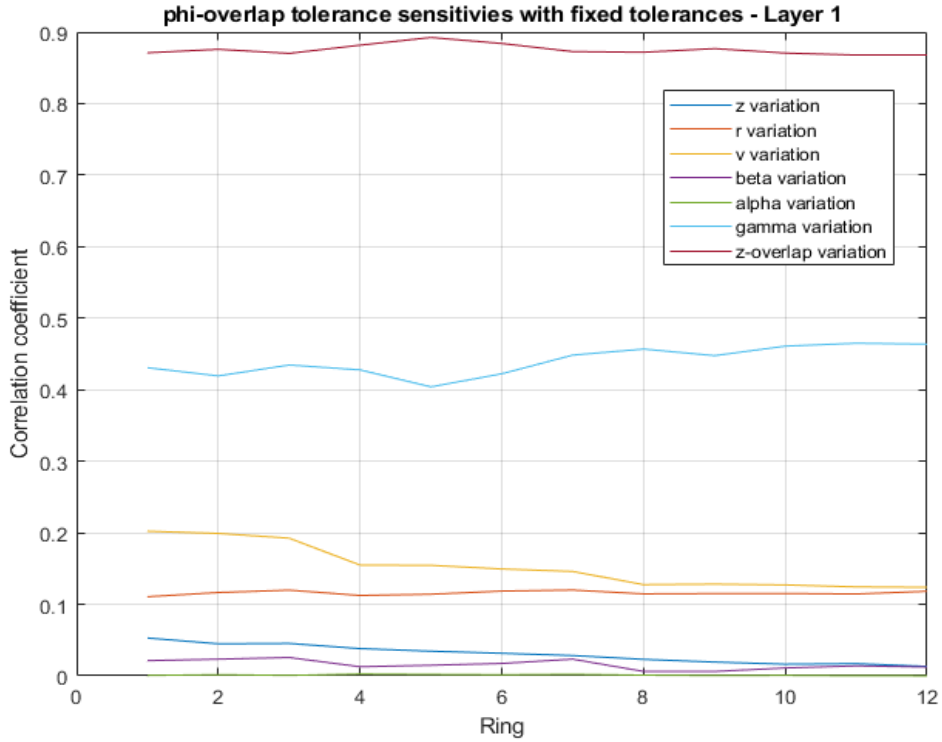

Figure 38. φ-overlap sensitivity analysis in layer 1.

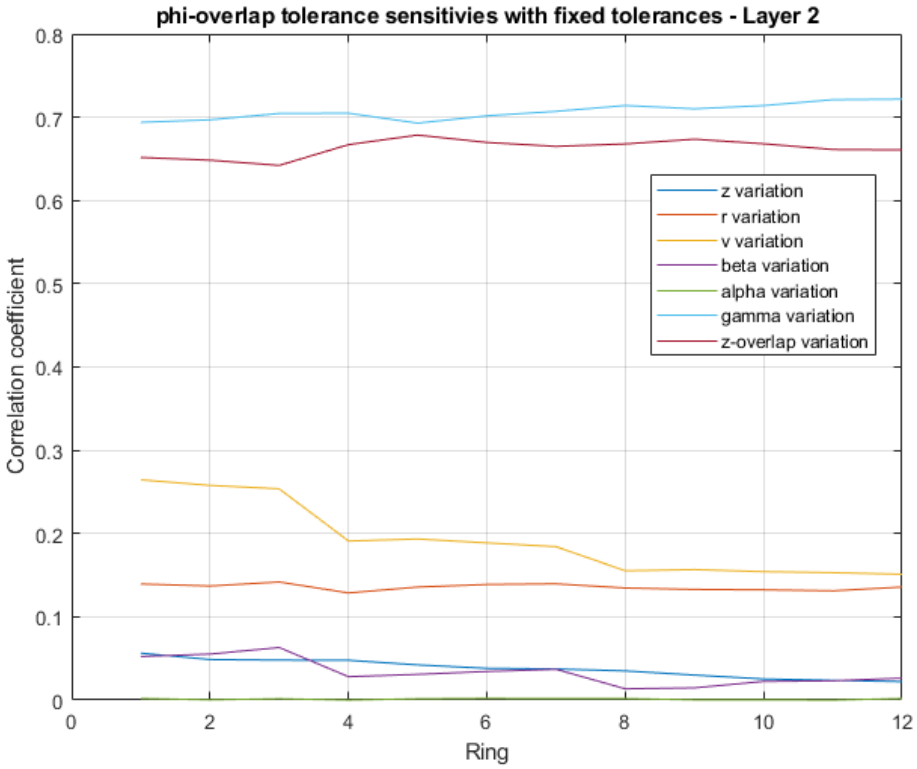

Figure 39. φ-overlap sensitivity analysis in layer 2.

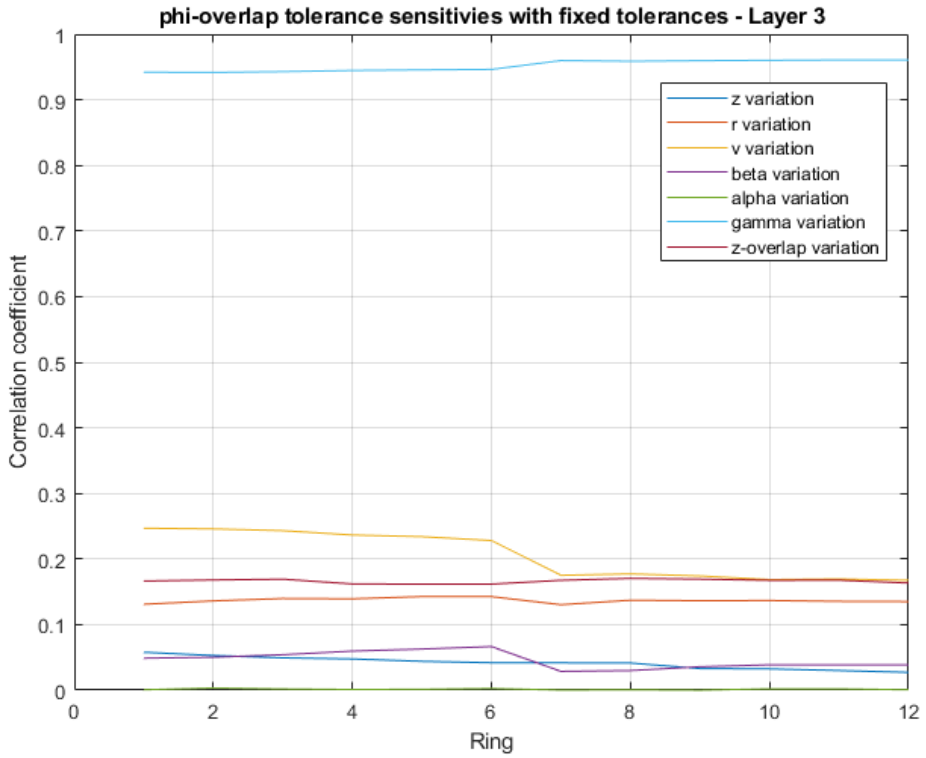

Figure 40. φ-overlap sensitivity analysis in layer 3.

The correlations were calculated again by using Pearson's linear correlation coefficient (see section 3.4.2) with 500 000 combinations of variation and results. The parameters correlation to φ-overlap is linear apart from α variation. However, α variations effect is negligible when run individually; see Appendix B for clarification.

Translational variation of modules in z, v and r was ±400 µm, and the changes were applied to the outer module (module on the right side). All rotational changes were 1°. Variation of z-overlap was ±3 mm in layer 1, ±2 mm for layer 2 and ±0.5 mm for layer 3. The reason for changes in z-overlap variation magnitude is that z-coverage magnitudes also change between the layers. As z-overlap variation is directly related to how close to ±70 mm the z-coverage is in that ring, the variation can be expected to be higher in all of the rings in layer 1 and layer 2 and lower in layer 3. For simplicity, translational and rotational changes were implemented into only one of the sensors (modules).

As can be seen from the results, the variations affecting φ-overlap are quite similar across the layers, except for z-overlap variation and rotational variation around the w-axis in module local coordinate system (γ). γ variation seems to be the dominant factor affecting φ-overlap in all layers. Z-overlap seems like a major contributor in layer 1, but this is because the magnitude of the dimension is allowed to vary in the limits given by z-coverage related tolerances. The purpose of depicting the results in such a way is to give an idea of how much z-overlap affects φ-overlap.

As mentioned, φ-overlap is mostly a result of variation in a modules rotational alignment around the modules w-axis (γ). This is followed by translational variations in r and v, that both contribute a similar amount with a correlation factor of 0.15 – 0.25

depending on the layer. Translational variation in z and rotational variation around the v-axis (β) contribute a small amount, with a correlation factor of about 0.05. Rotational alignment around the u-axis (α) has the smallest correlation coefficient. This is because α correlation to φ-overlap is non-linear, but when inspected individually, it can be concluded that its effect is marginal and can thus be ruled out of the tolerance synthesis.

The variation sensitivities appear to be mostly static across the layers, with major changes between the sensitivities occurring only between modules 3 – 4 and 7 – 8 in layers 1 and 2, and between modules 6 – 7 in layer 3. This seems to be a result of the modules tilt angles changing between those rings and indeed, with higher nominal tilt angle values, φ-overlap is more sensitive to changes in the tilt angle. This is reasonable as higher tilt angle values increase the magnitude of the trigonometric functions associated with them, which in turn increase their influence on φ-overlap.

So what do these results mean in practice? When designing the rings and the modules positions on them further, one should be especially careful in achieving a high precision in the module's γ orientation (see Figure 37 for clarification of which dimension this refers to). Furthermore, when assuring the quality of the rings by measurements, the most important value to check is the modules deviation in γ from the nominal value. Module positions in r and v are also critical.

In addition, the sensitivity analysis results of layer 1 indicate that z-overlap has a large impact on φ-overlap. This means that if z-overlap were allowed to vary greatly in layer 1 as would be allowed by the z-coverage requirement, unnecessarily tight tolerances would then need to be imposed on the positioning of modules on rings, to ensure the φ-overlap.

3.5.2 Tolerance synthesis

As mentioned above, certain simplifications have been made in regards of the mathematical model used to calculate the φ-overlap. These simplifications were chosen such that they would not have a major effect on the sensitivity analysis of the tolerances, but they do have a slight effect on actual tolerance estimation. In addition, for simplicity, the tolerances depicted in this section are calculated in a similar manner as with tolerances based on the z-coverage and z-overlap (chapter 3.4.2 except the dimensional changes have been applied to only one of the modules: the module on the right side (outer module). The tolerances are then divided by two to account for the tolerances related to the inner (left) module.

Z-overlap has been implemented into the calculation by first calculating the worst-case z-overlap from z-coverage related tolerances. This value is then used to figure out the dimensional tolerances related to φ-overlap. Rotational alignment around the module u-axis (α variation) is neglected because its effect was deemed marginal.

Tolerance values have been calculated for module γ-position first, which were then multiplied by a given ratio and applied to the calculation of the next tolerance value: translational alignment in the v-axis in module local coordinate system (similarly as in 3.4.2). This is carried on in the order of parameter correlation magnitude, with the magnitudes of the ratios being 0.7 for z and r and 0.5 for v, β and γ. The results are depicted in Table 8.

As can be seen, the translational tolerances are in the range of a few hundred micrometers and the rotational tolerances range from 0.1 ° degrees to 1 ° degrees. These results are an example of a tolerance configuration that should guarantee a positive φ-overlap for all rings throughout the layers when z-overlap is assumed to be at its worst-case magnitudes, except for the ones that had a negative φ-overlap to begin with. However, φ-overlap is positive only for particles that originate from the nominal collision point.

Table 8. Tolerances derived from φ-overlap requirements. Increment of shifts was 2.5 µm. z-overlap was assumed to be at its worst-case value. Rings that have zero tolerances related to their modules positioning, indicate that φ-overlap is negative in those rings with nominal module positions, when the z-overlap is at its worst-case value.

Ring	1	2	3	4	5	6	7	8	9	10	11	12
Module dimensional tolerances layer 1 [±mm/deg]												
z	0,603	0,056	0,008	0,142	0,115	0,074	0,019	0,202	0,480	0,088	0,028	0,000
r	0,712	0,160	0,019	0,314	0,261	0,138	0,031	0,188	0,192	0,103	0,025	0,000
v	0,160	0,129	0,017	0,154	0,268	0,149	0,034	0,234	0,243	0,134	0,034	0,000
β	0,327	0,320	0,036	1,055	0,887	0,374	0,070	3,143	6,862	0,632	0,112	0,000
γ	0,644	0,272	0,033	0,374	0,431	0,230	0,050	0,295	0,306	0,165	0,040	0,000
Module dimensional tolerances layer 2 [±mm/deg]												
z	0,085	0,058	0,030	0,072	0,109	0,085	0,049	0,064	0,073	0,039	0,000	0,000
r	0,235	0,144	0,067	0,177	0,242	0,167	0,085	0,116	0,112	0,053	0,000	0,000
v	0,166	0,108	0,053	0,164	0,231	0,167	0,088	0,136	0,134	0,064	0,000	0,000
β	0,291	0,170	0,077	0,379	0,493	0,310	0,146	0,549	0,450	0,174	0,000	0,000
γ	0,306	0,191	0,089	0,214	0,308	0,214	0,109	0,142	0,140	0,065	0,000	0,000
Module dimensional tolerances layer 3 [±mm/deg]												
z	0,176	0,152	0,142	0,127	0,112	0,093	0,142	0,175	0,168	0,158	0,144	0,137
r	0,531	0,423	0,360	0,297	0,241	0,186	0,320	0,361	0,312	0,266	0,221	0,193
v	0,246	0,311	0,276	0,237	0,200	0,159	0,321	0,366	0,324	0,284	0,243	0,216
β	0,684	0,525	0,433	0,347	0,274	0,205	0,819	0,859	0,677	0,536	0,420	0,347
γ	0,416	0,412	0,358	0,300	0,247	0,191	0,300	0,347	0,302	0,259	0,216	0,189

As the values above correspond to a scenario where z-overlap is at its worst, it is also worth to analyze the situation where z-overlap is at its nominal value. After all, the

tolerances that result in the values of z-overlap can be assumed to roughly follow a normal distribution. The tolerance scenario in such a setup with the same ratios and increment magnitude as in the previous setup can be seen in Table 9.

Table 9. φ-overlap related tolerances with nominal z-overlap values.

Ring	1	2	3	4	5	6	7	8	9	10	11	12
Module dimensional tolerances layer 1 [±mm/deg]												
z	0,603	0,162	0,134	0,261	0,486	0,244	0,219	1,261	2,401	2,995	4,204	5,889
r	0,712	0,486	0,338	0,719	0,796	0,595	0,368	0,551	0,577	0,446	0,382	0,361
v	0,160	0,374	0,281	0,538	0,758	0,602	0,396	0,589	0,687	0,549	0,481	0,459
β	0,327	1,175	0,725	5,115	12,338	2,743	1,098	8,276	12,678	14,292	16,431	18,492
γ	0,644	0,866	0,619	1,104	1,444	1,077	0,660	0,878	0,992	0,760	0,652	0,618
Module dimensional tolerances layer 2 [±mm/deg]												
z	0,116	0,107	0,082	0,137	0,179	0,158	0,146	0,095	0,145	0,143	0,110	0,104
r	0,324	0,265	0,186	0,345	0,406	0,315	0,257	0,251	0,265	0,207	0,135	0,114
v	0,226	0,196	0,144	0,315	0,379	0,307	0,261	0,288	0,308	0,246	0,165	0,141
β	0,410	0,329	0,222	0,802	0,898	0,628	0,478	1,803	1,311	0,793	0,437	0,334
γ	0,429	0,364	0,260	0,437	0,537	0,418	0,346	0,320	0,345	0,269	0,174	0,149
Module dimensional tolerances layer 3 [±mm/deg]												
z	0,176	0,152	0,143	0,127	0,115	0,102	0,153	0,177	0,169	0,162	0,158	0,156
r	0,531	0,423	0,361	0,297	0,246	0,204	0,349	0,364	0,314	0,274	0,245	0,221
v	0,246	0,311	0,277	0,237	0,204	0,176	0,340	0,369	0,327	0,292	0,266	0,246
β	0,684	0,525	0,435	0,347	0,282	0,228	0,900	0,870	0,684	0,554	0,466	0,400
γ	0,416	0,412	0,359	0,300	0,253	0,212	0,325	0,351	0,305	0,266	0,240	0,218

The most notable difference can be seen in layer 1, with layer 2 also demonstrating some effects. When manufacturing and assembling the rings, these results can be used to check whether the achieved accuracy falls somewhere between these two scenarios, or close to them.

The tolerances depicted in this φ-overlap section correspond to tolerances that are associated with individual ring assemblies (specifically mounting precision of modules on a single ring). As such, the precision of the assembly can be expected to be higher than in the case of a whole tilted sections assembly, which is the case for the z-coverage (section 3.4.2 Nevertheless, the magnitudes of the tolerances obtained for the φ-overlap are quite low which means that the rings of the tilted section need to be made in high precision.

3.6 Tolerance allocation

As mentioned in 3.2.1 , there are eight different variants of TBPS ring structures. Thus, tolerances should be allocated to these eight variants rather than having distinct tolerances for each of the 72 individual rings. The tolerance values associated with each ring type and the ring's variant class distributions are displayed in Table 10 below.

Table 10. TBPS tilted section ring variants and tolerances associated with them. The degree value in ring variation names indicates the nominal tilt angle of the modules in that ring.

Layer 1 - 47°				
Module positioning tolerances		Ring positioning tolerances		
z[mm] ±	0,134	z[mm]	+	0,000
r[mm] ±	0,338		-	0,599
v[mm] ±	0,160	r[mm]	+	1,161
β[deg] ±	0,327		-	0,000
γ[deg] ±	0,619			

Layer 1 - 60°				
Module positioning tolerances		Ring positioning tolerances		
z[mm] ±	0,219	z[mm]	+	0,964
r[mm] ±	0,368		-	1,276
v[mm] ±	0,396	r[mm]	+	0,786
β[deg] ±	0,500		-	0,864
γ[deg] ±	0,660			

Layer 1 - 74°				
Module positioning tolerances		Ring positioning tolerances		
z[mm] ±	1,261	z[mm]	+	1,405
r[mm] ±	0,361		-	1,855
v[mm] ±	0,459	r[mm]	+	0,765
β[deg] ±	0,490		-	0,765
γ[deg] ±	0,618			

Layer 2 - 40°				
Module positioning tolerances		Ring positioning tolerances		
z[mm] ±	0,082	z[mm]	+	0,282
r[mm] ±	0,186		-	0,282
v[mm] ±	0,144	r[mm]	+	0,423
β[deg] ±	0,222		-	0,471
γ[deg] ±	0,260			

Layer 2 – 55°				
Module positioning tolerances		Ring positioning tolerances		
z[mm] ±	0,137	z[mm]	+	0,340
r[mm] ±	0,257		-	0,452
v[mm] ±	0,261	r[mm]	+	0,339
β[deg] ±	0,395		-	0,414
γ[deg] ±	0,346			

Layer 2 - 68°				
Module positioning tolerances		Ring positioning tolerances		
z[mm] ±	0,095	z[mm]	+	0,499
r[mm] ±	0,114		-	0,621
v[mm] ±	0,141	r[mm]	+	0,321
β[deg] ±	0,334		-	0,321
γ[deg] ±	0,149			

Layer 3 – 44°				
Module positioning tolerances		Ring positioning tolerances		
z[mm] ±	0,102	z[mm]	+	0,016
r[mm] ±	0,204		-	0,044
v[mm] ±	0,176	r[mm]	+	0,072
β[deg] ±	0,228		-	0,027
γ[deg] ±	0,212			

Layer 3 - 60°				
Module positioning tolerances		Ring positioning tolerances		
z[mm] ±	0,153	z[mm]	+	0,079
r[mm] ±	0,221		-	0,079
v[mm] ±	0,246	r[mm]	+	0,060
β[deg] ±	0,250		-	0,060
γ[deg] ±	0,218			

The z, r, v and γ tolerances have been selected from the φ-overlap tolerance scenarios shown in chapter 3.5.2 . Conversely, ring positional tolerances were selected from z-coverage tolerance scenarios based on chapter 3.4.2 . β tolerance was selected from these two scenarios, by choosing the one that was smaller for each ring type. Module positional tolerances were selected from the tolerance scenarios where z-overlap was assumed to be at its nominal value in modules (Table 9). Ring positional tolerances in layer 3 were selected from the scenario where z-coverage requirement was set to be 65 mm (Table 7).

In this chapter, tolerance values in Table 10 are utilized to allocate actual tolerance values to the manufacturing drawing of ring "layer 1 - 47°", which is the ring closest to the IP in the first layer. All other rings follow the same logic as applied here.

3.6.1 Tolerance allocation of ring variant "layer 1 – 47 °"

The most important dimensional relationship in the rings is between insert holes used to attach the modules onto the rings, and reference ear holes used for attaching the rings to a layer (see Figure 41). Together, these dictate the final positions of the modules in a TBPS layer.

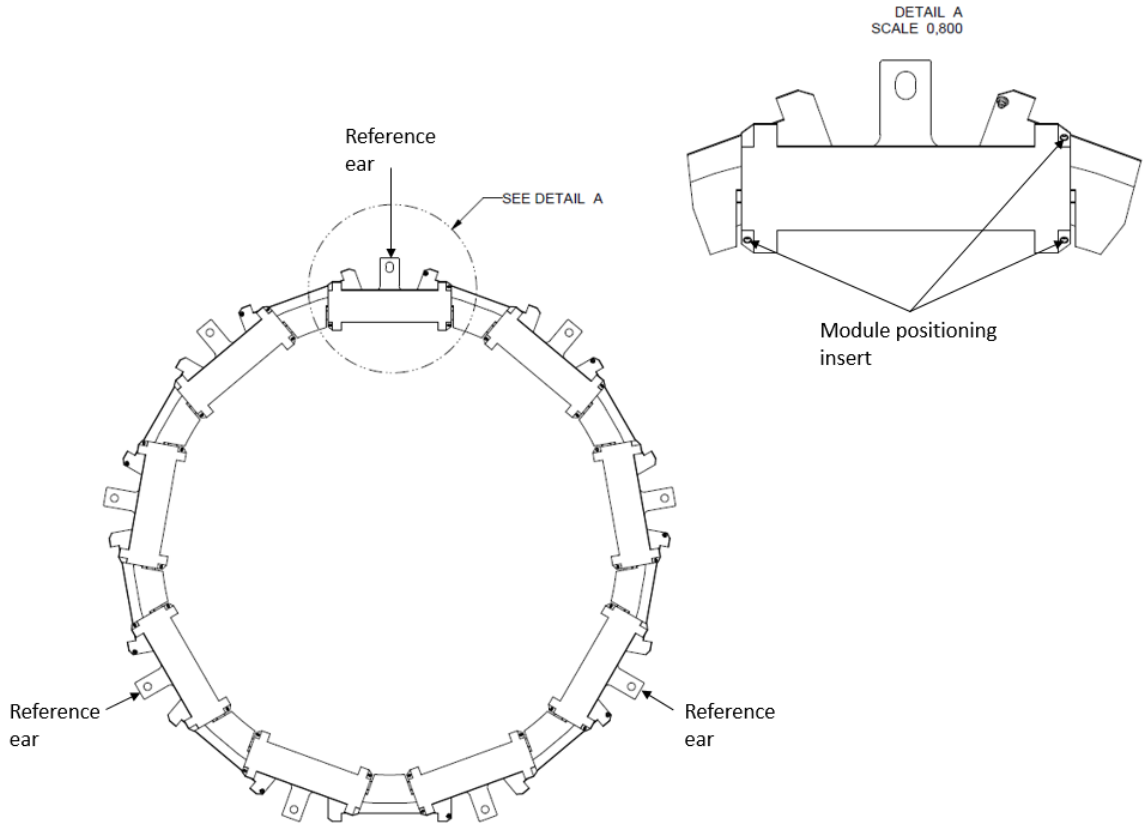

Figure 41. Ring reference ears and module positioning inserts.

Table 11. 47 ° ring tolerances.

Layer 1 - 47°				
Module positioning tolerances		**Ring positioning tolerances**		
z[mm] ±	0,134	**z[mm]**	+	0,000
r[mm] ±	0,338		-	0,599
v[mm] ±	0,160	**r[mm]**	+	1,161
β[deg] ±	0,327		-	0,000
γ[deg] ±	0,619			

The objective of the tolerance allocation is to specify that the module positioning inserts are located according to the tolerances depicted in Table 11, in respect to holes in the reference ears. The z and r tolerances of modules in a ring must be chosen carefully so that large enough values are left for positioning the ring in a layer.

The intersection between the flat TBPS section and the first tilted layer has a z-coverage value below 70 mm with nominal module positions. Because of this, the positive ring positioning tolerance in z and the negative ring positioning tolerance in r are 0. Moving the first ring in the layer closer to the flat section would dissolve this issue.

However, this analysis is performed with the nominal module positions derived from the current geometry of the tracker, so such adjustments are not realized. Rather, the 0 tolerances are accounted for by placing stringent tolerance requirements for module positions in a ring.

The modules are fixed on cooling plates (see Figure 41) which are manufactured before the ring is assembled. As the positioning tolerances of the insert holes on these plates already necessitate that a module can physically be fixed on them, we do not need to specify positional tolerances for each separate insert hole in the ring. Rather, we can specify a module reference center from these inserts, as shown in Figure 42, which we use for allocating positional tolerances for the modules on a ring.

To simplify the representation of the tolerances, we can also indicate a reference center for the ring, measured as the center of a circle formed by the holes in the reference ears as shown in Figure 42.

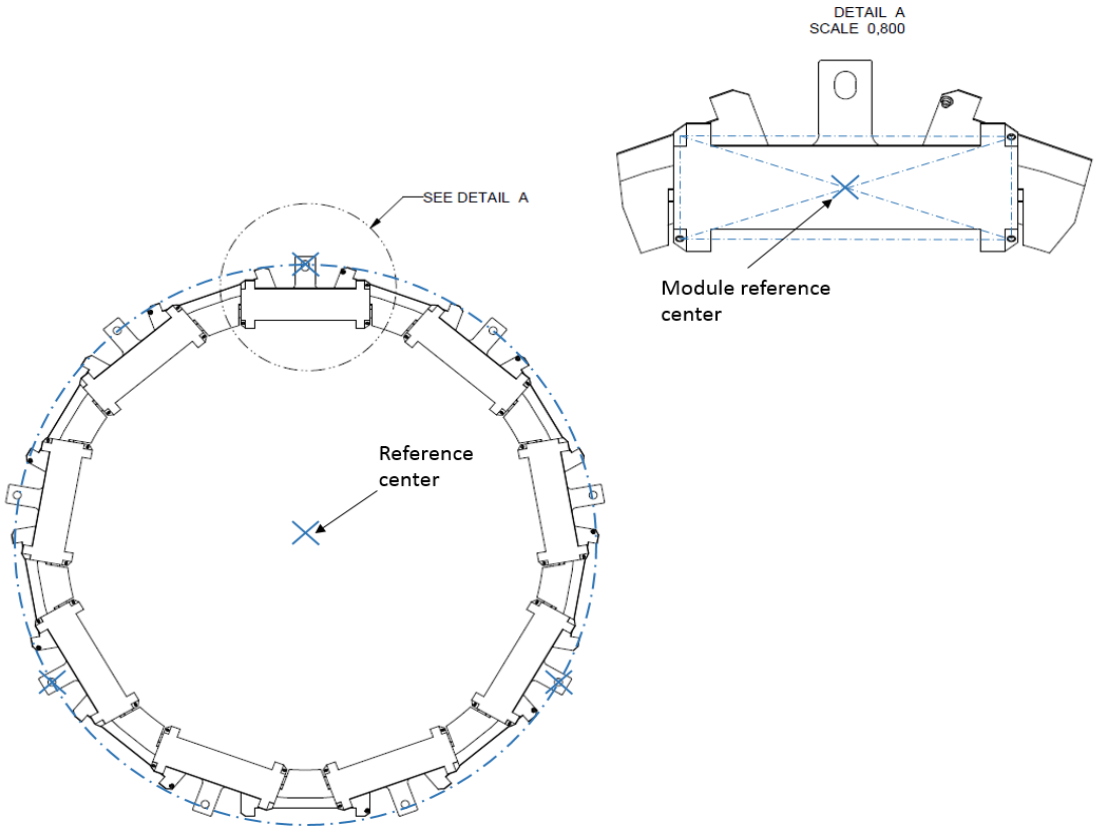

Figure 42. Ring references used for tolerance allocation.

By using these reference points, we can allocate tolerances to the nominal module positions as shown in Figure 43. Outer and inner module positions in r along with the associated tolerance can be depicted from the reference center to the module reference centers. In Figure 43 detail A, module positioning in v is depicted as the distance between the module reference centers of two successive cooling plates. In the same detailed view, γ is measured as the angle between lines formed by two of the lower (in the figure) module inserts in consecutive cooling plates.

Details B and C show module positioning in z, measured as the distance between the reference center and module reference centers in the plane of the view. Module β is depicted as the angle between the plane of the cooling plate, and the plane of the ring element. Dimensions and tolerances shown in Figure 43 apply to all of the cooling plates in a circular pattern.

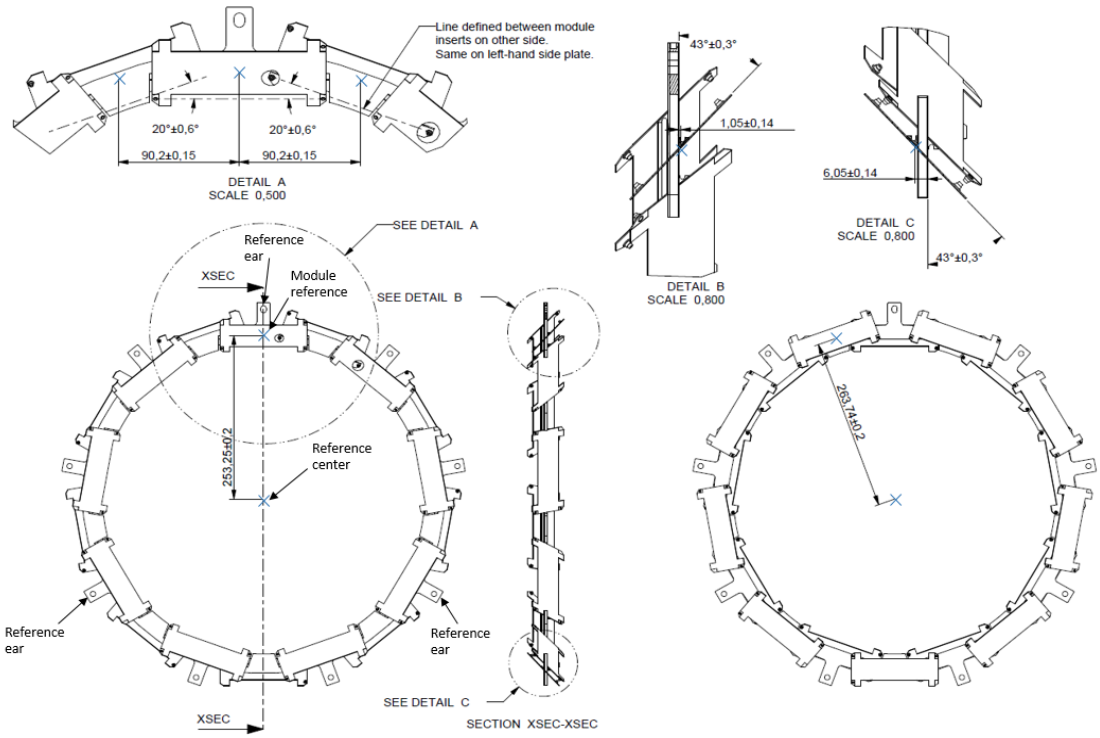

Figure 43. Manufacturing tolerances for a 47 ° ring.

4 Dimensional measurement of the TBPS

The high intrinsic resolution of the silicon detector modules (10 – 30 μm) demands that the actual position of the modules in space should be known with an accuracy significantly better than the resolution. Although modern probing coordinate measurement machines (CMM) can reach such accuracies [24], it is either unpractical or impossible to measure the module positions in a full TBPS assembly with a probing CMM. This is due to the relatively large size of the TBPS, and because in the TBPS assembly many of the modules will be unreachable by a CMM probe. [21], [25], [26]

To overcome this, the final calibration of the detector module positional data is achieved by alignment algorithms. These algorithms use actual tracking data from the detector to adjust the information of module positions. The initial alignment is done with high momentum tracks originating from cosmic rays, with the solenoid magnet off. These tracks are valuable for the initial alignment, because their reconstruction is easier due to their practically straight trajectory.

The reconstruction residuals, which is the difference between reconstructed track and recorded hit position, are used to optimize the module positions so that the hits correspond with the tracks [26]. The final alignment is done with tracks originating from LHC collisions with the solenoid magnet on. The methodology involved, and the actual algorithms are quite complex and as such, outside the scope of this analysis. The reader is referred to [21], [25] and [26] for more information.

Previous experience has shown that track-based alignment algorithms have the capability of increasing the accuracy of positional data from mechanical constraints by at least an order of magnitude [26]. During the alignment of the existing CMS tracker, misalignment simulations were carried out and their effect on the convergence of the alignment algorithms was studied. The applied magnitude of the misalignments was ±100 – 300 μm from the nominal position for individual modules, and according to the simulations, the algorithms converged well with such offsests. [26], [27]

Positional tolerances in the TBPS are in a similar range as the misalignment magnitudes used in the alignment algorithms' convergence simulations. We can therefore conclude that tracker alignment does not set an accuracy requirement for the dimensional measurement of the TBPS. Rather, the accuracy requirements originate directly from the positional tolerances of the modules derived from the hermeticity requirement.

However, the software alignment of the tracker is faster if the initial module positions are known with a high accuracy. Because the dimensional measurement will be carried out either way for quality assurance, the results should be passed on to the alignment team. [28]

The goal of this section is to analyze the requirements and restrictions of TBPS dimensional measurement, and how existing measurement methods fulfill them. The analysis is carried out separately for the complete TBPS, a single layer of the tilted section and a single ring of the TBPS. This chapter will begin with a literature review of large-scale metrology methods in section 4.1, which is followed by a survey of available measurement methods at CERN (section 4.2). The latter section is based on conversations

with the groups at CERN responsible for the devices, and presentations prepared by them. Section 4.3 will give a quick overview of measurement method selection criteria in general, and the following chapters will describe the dimensional measurement plans designed in this thesis.

4.1 Large-scale measurement methods

Large-scale metrology is usually associated with objects where linear dimensions range from 1 m – 100 m. The characteristic problem for such systems is the demanding relationship between the large dimensions of the object, and small tolerances that demand high accuracies from measurement systems. The measurement systems also need to be highly reliable, as the objects are usually a part of first-time-right production. This chapter will give a brief overview of the state-of-the-art of large-scale measurement systems. [29]

Schmitt et al. [29] divide large-scale measurement systems into two categories as in Figure 44: centralized systems and distributed systems. The main distinction between the two is that in centralized systems the coordinates of a point can be obtained from a single measuring unit, while in distributed systems the coordinates are calculated from multiple measuring units. The systems can also be separated into two categories based on their way of operation: serial kinematic systems and optical systems.

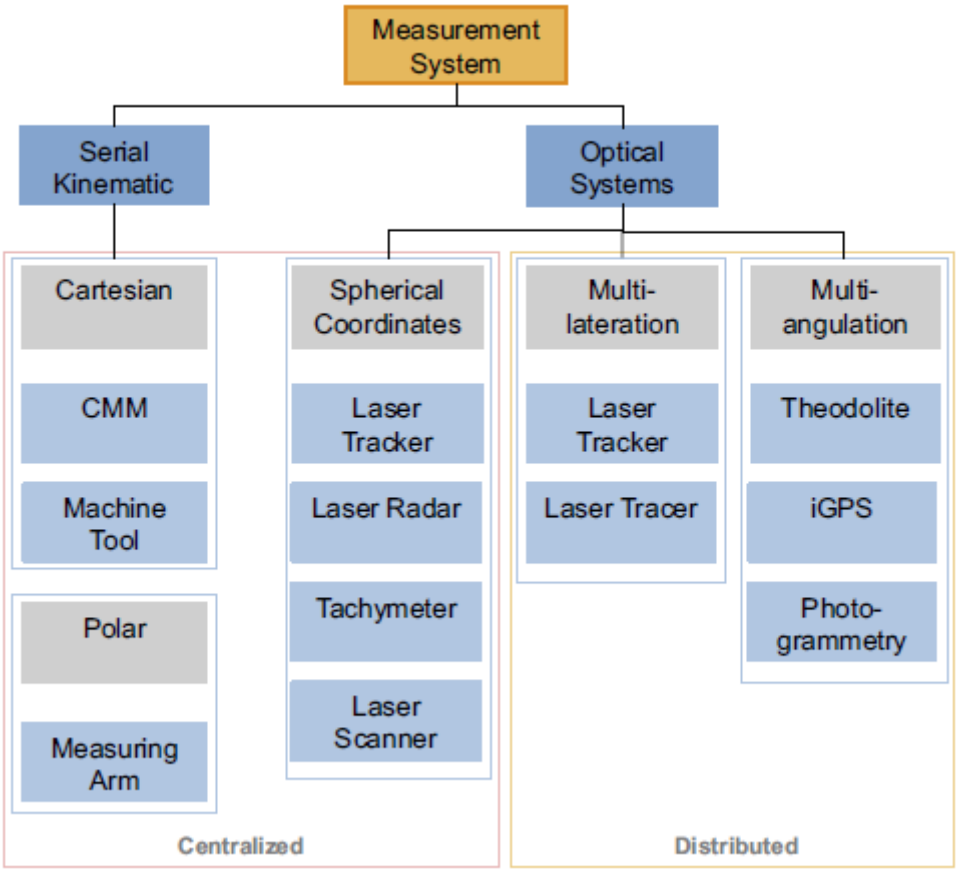

Figure 44. Classification of large-scale metrology systems. [11]

4.1.1 Serial kinematic systems

Traditional probing coordinate measurement machines (CMM) are widely used for the measurement of small to medium sized objects when high accuracy and reliability are needed. However, variants for large objects also exist that can operate in a measuring area of multiple meters, with maximum permissible errors of 5.5 µm + 6 * L/1000 µm /m (L = measuring distance in meters). One such CMM is depicted in Figure 45. The probe of a CMM can also be replaced with a non-contact head, such as a laser scanner. This allows the system to measure hard-to-access features as well as to provide high measurement point densities for freeform shapes. [30], [31]

Figure 45. Leitz PMM-G by Hexagon. Measuring range up to 7 m x 4 m x 3 m in xyz. [48]

While large-scale CMMs can operate in large measuring ranges and achieve extraordinary accuracies, they are usually custom-built for the product-line, immobile and very expensive. This can be countered somewhat by utilizing measuring arms, which operate similarly to industrial robots. The downside of this is that they are less accurate than CMMs. [29]

4.1.2 Laser based systems

Laser trackers are typically interferometric distance measurement devices. Their main functionality is to track moving targets, such as the probe of a CMM. The laser guiding system is equipped with angular sensors, such as rotary encoders, that allow the system to calculate the positions of measurement points in spherical polar coordinates once the system has been calibrated. A recent development in laser trackers is to replace the interferometric distance measurement device with an absolute distance measurement device, which makes calibrating the system easier. This is because interferometric measurements are relative, and thus require the use of a retroreflector at a known distance for calibration. [29]

Furthermore, recent developments have resulted in a new kind of system closely related to laser trackers: the laser tracer. A laser tracer uses interferometric distance measurement, where the interferometer is mounted on a gimbal-mount that moves around a precisely manufactured sphere. The idea is to eliminate errors caused by mechanical deviations, by having the interferometers mirror (sphere) stationary and not connected to any mechanical functionality. The laser tracer has no angular measurement of the laser guiding system, and as such relies on multilateration algorithms to calculate the coordinates of measurement points. The error of such systems can be as low as 0.2 µm + L*0.3 µm / m (L = measuring distance in meters). Laser tracers are mainly used for the calibration and tracking of CMM and machine tools. Such a system is depicted in Figure 46. [29] [32]

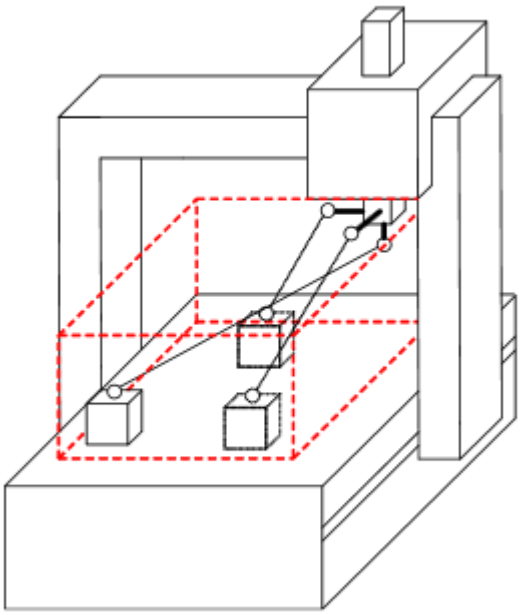

Figure 46. Multi-angulation setup of laser tracers in a machine tool or CMM. [14]

Laser scanners and laser radars are laser-based rangefinders that operate similarly to radio wave radars. Their intrinsic benefit is that they do not necessitate the use of targets on the measurement object; they can even measure points on featureless surfaces. The method for obtaining distance measurements is based on time-of-flight measurement,

phase-shift measurement or triangulation. Both of these systems are notably less accurate than laser trackers. [29]

4.1.3 Optical multi-angulation systems

Optical multi-angulation systems consist of theodolites, iGPS and photogrammetry. A theodolite is an instrument used for measuring angles and typically utilized in geodetic measurements. Taking multiple measurements of a single point from different orientations allows calculation of the points coordinates.

Nikon's iGPS (indoor global positioning system) utilizes theodolites in such a configuration to calculate measurement points coordinates. In this system, the theodolites emit two laser planes that rotate horizontally and an infrared pulse that rotates vertically. These pulses enable the theodolites to decipher the elevation and azimuthal angle of measurement points in respect to themselves. The actual measurement points are photodiodes, and the principle of measurement is based on the sequence of signals that hit them. Such a systems accuracy is approximately 200 µm, and it is usually used to measure the positions of multiple objects across a factory floor. [29], [33]

Photogrammetry relies on multiple pictures of an object that are taken from different positions and orientations. The principle relies on features of interest appearing on at least three pictures, so that coordinates of the feature can be calculated with multi-angulation algorithms. In industrial applications, the features might not be easily distinguishable, so targets or structured light is used instead. In addition, utilizing just three images to determine the coordinates of a point makes the system prone to errors that result from manufacturing tolerances and faults in the camera. This is because information of the orientation of the cameras film and lenses, and their distance from each other, needs to be known beforehand, and is acquired by calibration. [29], [34]

The typical use of photogrammetry for industrial applications consists of taking a large quantity of pictures to account for these errors. In such a setup, the coordinates of points can be iterated using regression analysis. Furthermore, the camera can be calibrated beforehand by utilizing measurands with known positions and orientations. The accuracy of modern photogrammetry setups can reach 3 µm + 7 µm/m (3 sigma). [34], [35]

However, the accuracy of a photogrammetry system depends largely on the measurement setup. Most important factors are the number and position of targets, and how they appear in the images. According to Thomas Luhmann [36], practical experience has shown that photogrammetric systems are typically 3-4 times less accurate than the given sigma value.

Because a photogrammetry setup mainly consists of just a camera, targets and a computer running suitable software, the system is highly portable, expandable and rather cheap. An example of such a setup is shown in Figure 47.

Figure 47. Tools needed for performing measurements by photogrammetry. [17]

4.2 Measurement methods available at CERN

Various measurement methods are available at CERN ranging from accurate serial kinematic systems to optical systems for large-scale metrology. As it is reasonable to select methods that are already available, this chapter will focus on describing the options that the CERN metrology laboratory and the survey team have to offer.

4.2.1 Serial kinematic systems

The CERN metrology laboratory in the EN-MME group offers various state-of-the-art serial kinematic systems for dimensional measurement. While unrivaled in accuracy, the operating volume of these systems is not large enough for measuring the complete TBPS, the tilted sections, or a layer of tilted modules. However, a single TBPS ring structure, which demands the highest measurement accuracy compared to the other assemblies, can fit into the measurement volume of these systems. This makes the metrology laboratory a suitable candidate for measuring the TBPS ring prototypes.

The most accurate system available is the Leitz PMM-C Infinity CMM, which is depicted in Figure 48. The accuracy of this system is 0.3 µm + L / 1000 µm, where L is the measured dimension in mm. The measuring range is 1200 x 1000 x 700 mm in x-y-z. To ensure reliable measurement, the device is housed in a separate temperature controlled room with minimal temperature gradients over time.

Figure 48. Leitz PMM-C Infinity. [39]

While this machines accuracy is unparalleled, the tolerance magnitudes of the TBPS rings do not necessitate the use of such extreme methods. Slightly less accurate systems are housed in the laboratory that is more readily available.

These systems are two Zeiss Prismo Ultra CMMs with different measurement ranges. The smaller one is depicted in Figure 49. The measuring range of this machine is 1600 mmm X 2400 mm X 1000 mm in x-y-z, and the larger counterparts 1600 mm X 3000 mm X 1000 mm in x-y-z. Both of them have an accuracy of 2.0 + L/300 µm, where L is the measured distance in mm. [37]

As mentioned, these machines are more available than the one manufactured by Leitz and achieve accuracies that are decidedly adequate for the measurement of the TBPS rings. Furthermore, the high measuring range allows supporting the rings in a vertical position so that both sides of a ring can be measured without turning the object around and the ring can be measured in its final vertical orientation.

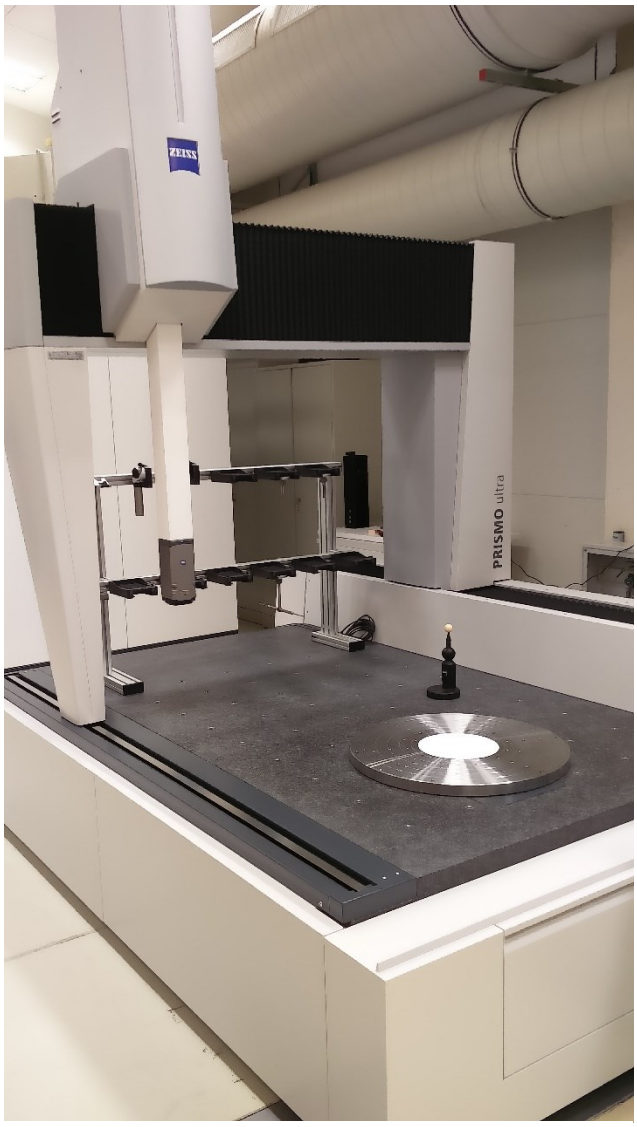

Figure 49. Zeiss PRISMO Ultra.

The metrology laboratory also has a multisensor CMM, ZEISS O-INSPECT shown in Figure 50. While this machine's measuring range (0.8 m x 0.6 m x 0.3 m in x-y-z) is smaller compared to the previously mentioned CMMs, this device also houses a microscope camera and a white light distance sensor. The accuracy of these three systems is 1.9 µm + L / 150 µm, where L is the distance measured in mm. While the measuring range does not allow supporting the rings vertically, the fast measuring time of the camera and the distance sensor can prove useful in the measurement of part planarity. [38]

Figure 50. Zeiss O-INSPECT [20].

While on the subject of systems capable of measuring the rings, it is important to make a distinction between the initial validation of the TBPS ring designs, now being done at CERN, to their final series production. The rings may ultimately be manufactured, and their quality assured, at some location other than CERN. As such, the location where the rings will ultimately be manufactured should have similar capabilities for dimensional measurement as discussed here.

4.2.2 Optical systems

The survey team in the EN-SMM group at CERN offers various optical measurement services. These systems can be used for large-scale metrology, but are not as accurate as the serial kinematic systems described before. This section will cover the available laser tracker, laser scanner and photogrammetry systems briefly.

The available laser tracker is the Leica AT40x. Typical accuracy for the system is 7.5 µm + 3 * L µm, where L is the measured distance in meters. An intrinsic benefit for laser trackers is that they are relatively accurate even when the measurements are performed from a distance. The system in question has an accuracy of roughly 50 µm even from a distance of 10 m. [39]

The drawback is that the trackers have to be mounted on tripods for measurement. This decreases the flexibility of the system, because line-of-sight has to be retained between targets and the instruments, and the setup requires expert assistance for operation.

The Leica HDS6200 laser scanner is a fast long-range measurement system, which produces a large point-cloud of its surroundings (see Figure 51). The system produces 1 million points per second at a range of 80 m and an accuracy of 5 mm. Because of the low accuracy compared to the other options, the laser scanner is mostly used when assembling sub-sections together to form the complete detector. However, the survey team is planning to purchase a laser scanner with an accuracy of 1.5 mm in the near future, which could prove to be beneficial in the quality assurance of certain parts (the CMS outer tracker support tube for example). [39]

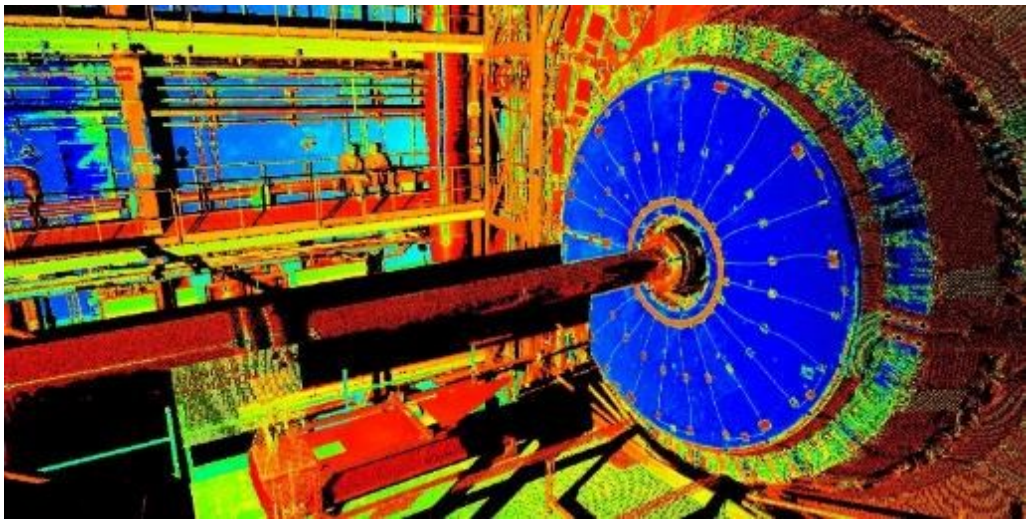

Figure 51. Point cloud of the CMS cavern produced by LEICA HDS6200. [36]

A Nikon D3X camera, AICON 3D Studio –DPA PRO software and a variety of targets are also available for photogrammetry. The purchase of a 50-megapixel camera is planned for the near future, which will allow using small targets (< 1 mm). The system is scalable for different dimensions and easy to use, as long as the target placement has been thoroughly planned. The target positioning affects the systems accuracy as well, which should be in the range of 20 µm – 50 µm with a properly devised setup.

4.3 Dimensional measurement requirements and restrictions

Measurement requirements and restrictions in general can be divided into three distinctive groups: task requirements, part restrictions and environmental restrictions (see Table 12) [40]. In case of the TBPS, accuracy and reliability are the most important factors of task requirements. The number of measurement points and the location of measurement points become important when optical systems have to be considered because of target placement. The number of measurements and measurement time are not strictly restricted.

Table 12. Factors affecting the choice of a measurement method. [19]

Factors affecting the choice of a measurement method				
Group	Task requirements	Part restrictions	Environmental conditions	Other
Factors	Accuracy Reliability Number of points Location of points Number of measurements Measurement time	Dimensions Accessibility Material Stiffness Surface quality	Temperature Vibrations Open air / indoor Available space Air turbulence Ambient lighting Contamination	Price Ease of use

Reliability is essentially a measure of how much redundant information the measurement system has to calculate the taken measurements. The amount of redundancy, and reliability alongside it, can be increased by having more points of measurement, and a higher number of measurements. The location of the measurement points also has an effect. [40]

As for part restrictions, the somewhat large dimensions of the complete TBPS and its layers, and module accessibility are the main restricting factors that have to be taken into consideration. The material, which is mostly carbon fiber reinforced polymer (CFRP), is restrictive in the sense that magnetic targets cannot be used in optical measurements. Stiffness and surface quality are not restrictive, as the assembly has high stiffness by design and the effect of gravity is expected to be small. Furthermore, the surface quality of the CFPR parts does not produce reflections that would interfere with photogrammetric measurements. However, once the detector modules are mounted the shiny surfaces of the silicon sensors are difficult to measure optically.

Environmental conditions such as temperature, available space, ambient lighting and such are important, but not restrictive to the choice of measurement method as they can be tempered to suit the measurement method in this case. Price is a factor that has impact in the case that multiple suitable measurement methods are identified. Ease of use can be significant in cases where measurements have to be performed during the assembly and without measurement specialists.

4.4 Dimensional measurement requirements of a complete TBPS

The most important factors affecting the choice of the measurement method for the complete TBPS assembly are displayed in Table 13. The main assembly steps that result in a complete TBPS are attaching the tilted sections to the flat sections, and attaching the layers together. In 3.4.2 we concluded that the accuracy of the joining of the tilted and flat sections is critical for ensuring hermeticity at the junction.

The positioning of the layers to each other does not have stringent accuracy requirements from the physics. The main thing to assure is that the complete TBPS, with its services (cables and pipes) properly fits into its allocated envelope within the tracker

volume and that the interfaces towards the neighboring sub-detectors (TB2S) and the Inner Tracker are properly located.

Table 13. Factors affecting the choice of measurement method for a complete TBPS assembly. Restrictive factors are shown in bold. Important but non-restrictive factors are displayed in brackets.

Factors affecting the choice of measurement method for a complete TBPS				
Group	Task requirements	Part restrictions	Environmental conditions	Other
Factors	**Accuracy** **Reliability** **Location of points** (Number of points) (Number of measurements)	**Dimensions** **Accessibility** (Material)	(Temperature) (Vibrations) (Available space) (Ambient lighting) (contamination)	(Price) (Ease of use)

4.4.1 Task requirements

The task requirements of a complete TBPS vary depending on if we are assessing the measurement of the complete layers quality, or the quality of the junction between the tilted and flat sections. In the former case, an accuracy of 50-100 µm should suffice. However, in the case of the junction, the tolerances involved range from 10 µm to 200 µm depending on the amount of hermeticity loss that is tolerable in that region. Accounting for the lower end of the tolerance spectrum, the measurement system should ideally have an accuracy of at least 5 µm. However, the actual effect that hermeticity loss has on the performance of the detector is marginal, so an accuracy of 30 µm should be reasonable.

4.4.2 Part restrictions

As can be seen in Figure 52, the complete TBPS is relatively large with a diameter of approximately 1.1 m, and a length of 2.4 m. This imposes a restriction on the measuring range of a dimensional measurement system. Furthermore, the layer structure of the TBPS sets additional requirements for the measurement system. For example, certain conventional CMMs can operate on work-pieces of this size, but the probe of a CMM could not reach the inner layers of the TBPS. These measurement systems are also expensive and usually meant for mass production, as described in 4.1.1 .

Taking the dimensions and accuracy requirements of TBPS into account, as well as the nature of the production (built just once), photogrammetry seems like the best solution. The system is relatively easy to setup, inexpensive, easy to use and accurate enough for the application.

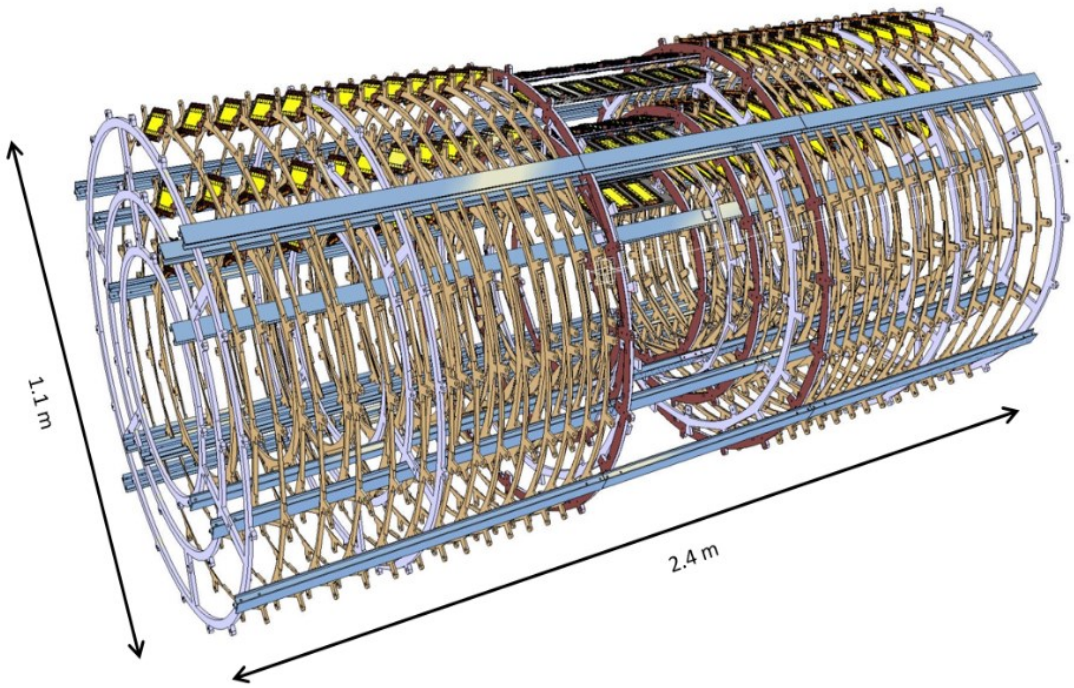

Figure 52. Complete TBPS assembly and its dimensions. The assembly sequence is still under study, the option shown here is to first inset layer 2 into layer 3, and then finally layer 1 into layers 2 & 3 [40]

4.4.3 Measurement setup

The complete TBPS assembly steps are shown in Figure 54 and Figure 53. First, the tilted sections and flat sections of the layers are attached together to form a complete layer. Second, the layers are attached together to form the complete TBPS. Detailed concepts of these steps have not been designed yet. For example, the layers might be joined together in vice versa order than what is shown in Figure 53.

Nevertheless, photogrammetric measurement setups can be analyzed by keeping both assembly variants in mind. If the assembly is done as shown in Figure 53, the image acquisition must be performed inside the assembly, with targets facing inside as well. On the other hand, if the layers are assembled on top of each other, the images can be taken around the object with targets facing outwards, similar as in the measurement setup for a single layer described in 4.5.3 This option, therefore, appears more attractive.

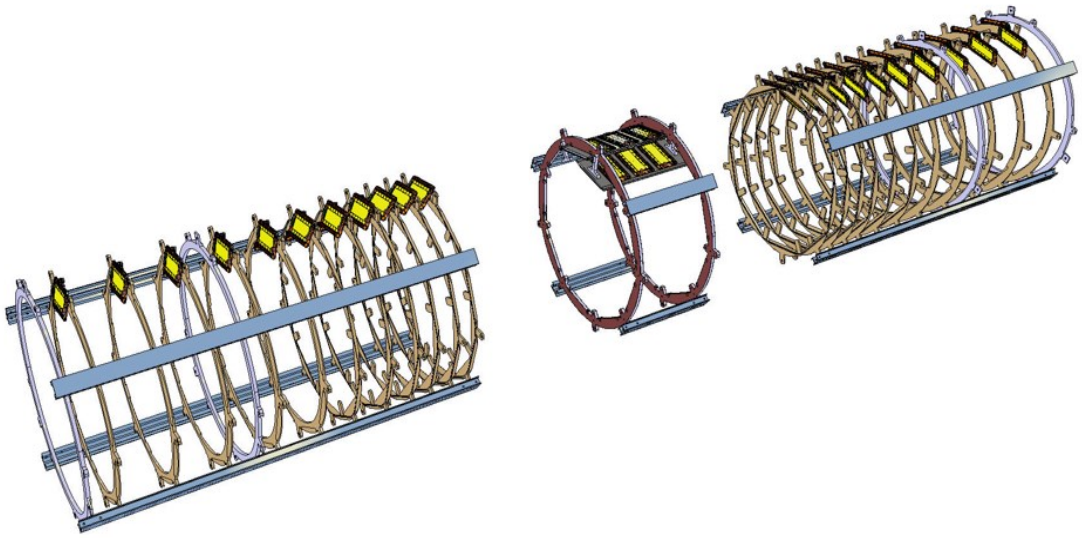

Figure 54. The tilted sections of each layer are first joined to the corresponding flat section. [40]

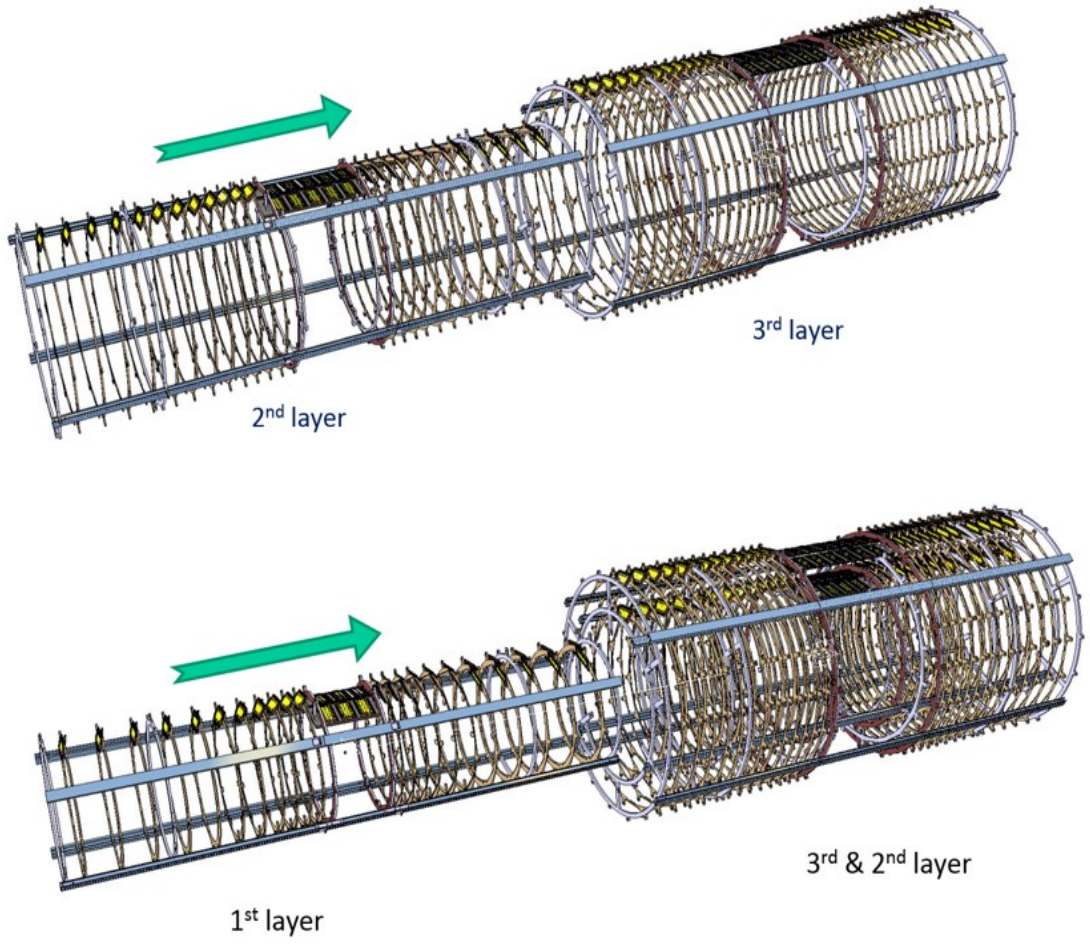

Figure 53. TBPS layers are attached together either starting from outside (shown here) or from layer 1 outwards. [40]

Placement of targets would be optimal if the same targets could be used as in the

measurement of the individual layers. However, the current proposal is to have the targets facing outwards from the layers, which would render photogrammetric image acquisition impossible from within the layers, if the assembly sequence is as shown in Figure 53. Thus, the alternative assembly order of attaching the layers on top of each other would be preferable from a measurement point of view.

Image acquisition has to be done for each layer separately after placement, because of visibility restrictions through the layers. As the position of a previously measured layer cannot be assumed to remain stable after fixing another layer on it, the layers should have targets that are visible throughout the assembly that link the measurements of a layer to those targets. Such targets could be placed on the ring shown in Figure 55 in all layers, which is the ring used for fixing the layers together that is further away from the IP.

As described previously, measurement of the complete TBPS serves the purpose of making sure that the layers are attached together in their appropriate positions, and to provide useful positional data for the alignment algorithms. The positional relationship between the layers is not restricted by any functional requirements, but the complete TBPS must fit into the space allocated for it in the outer tracker. The more critical measurement to perform is how the tilted sections are positioned in relation to the flat sections.

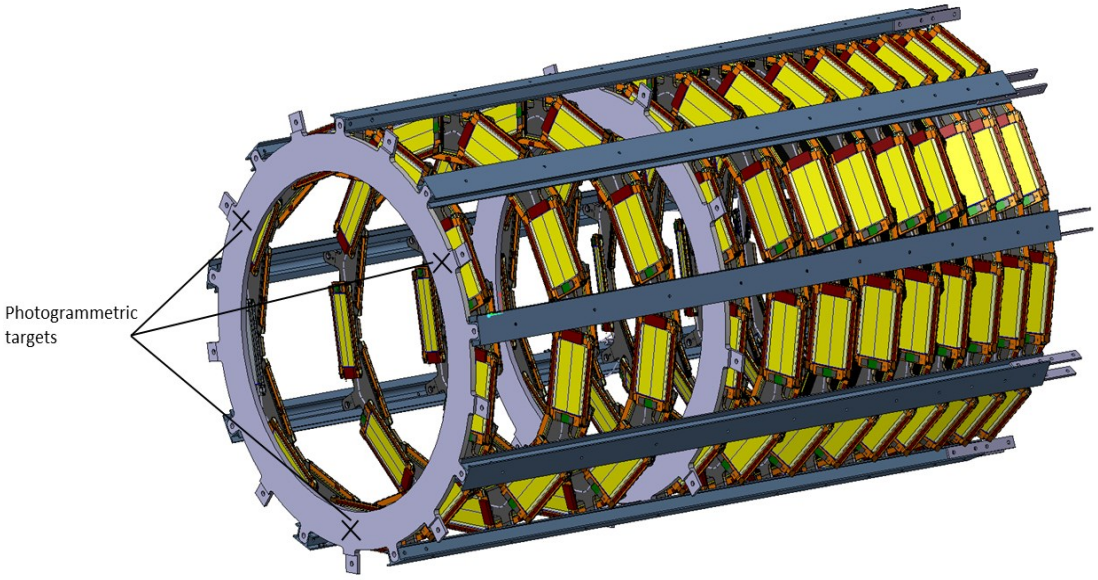

Figure 55. Placement of photogrammetric targets in layer 1 used as a reference for other measurements of the layer.

The tilted and flat sections are joined together as illustrated in Figure 56. Use of shims allows aligning this junction according to specifications. If the flat section will include visible photogrammetric targets, the quality of this junction can be measured with photogrammetry with an approximate accuracy of 30 µm (the tilted section will have targets on the beams, see 4.5.3).

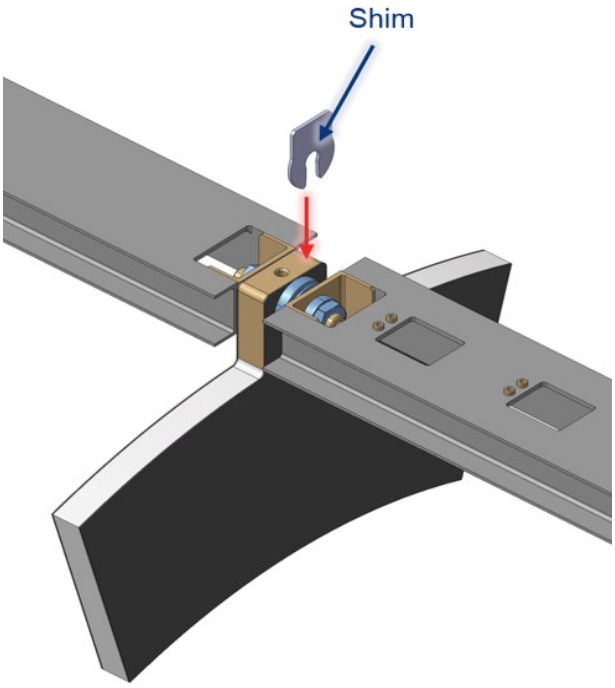

Figure 56. Flat - tilted section junction with the flat section on left-hand side, and the tilted sections on the right-hand side. [24]

In case there are no targets on the flat section, the z-dimension of the junction can be measured with an inside micrometer (see Figure 57). This measurement should be carried out either way, because it is more accurate than photogrammetry and fast to perform.

Figure 57. Inside micrometer by Mitutoyo. [25]

4.5 Dimensional measurement requirements of a TBPS layer

The rings of a tilted TBPS layer are attached to each other via longitudinal beams. To position the rings in relation to each other, they are "stacked" together as shown in Figure 58. The rings are placed one by one to form a complete assembly shown in Figure 59.

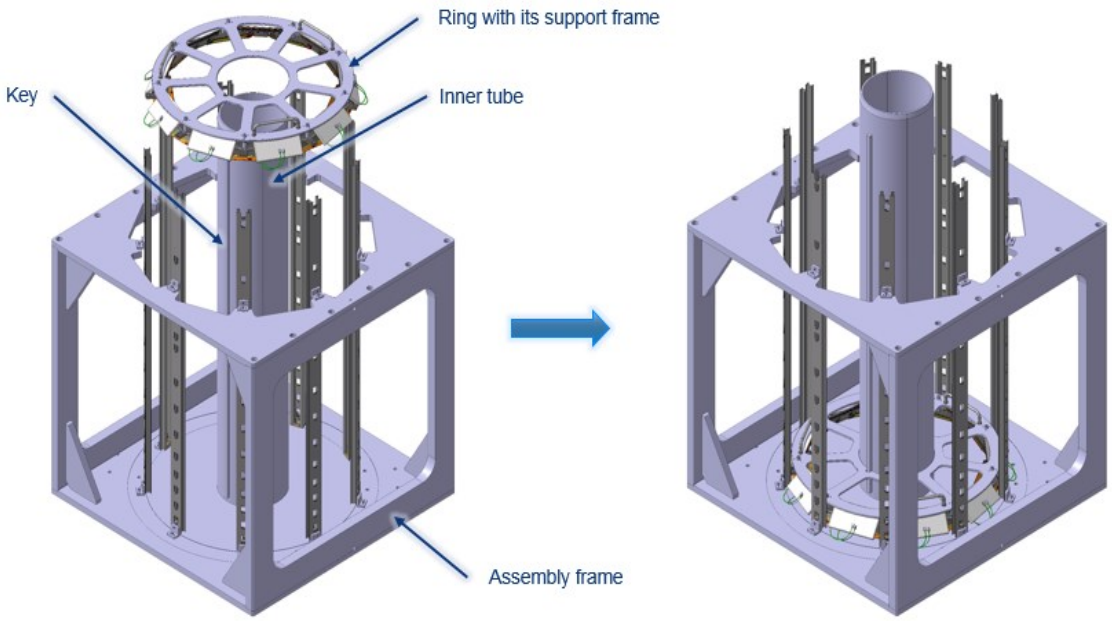

Figure 58. Stacking sequence of a tilted TBPS layer assembly phase. [41]

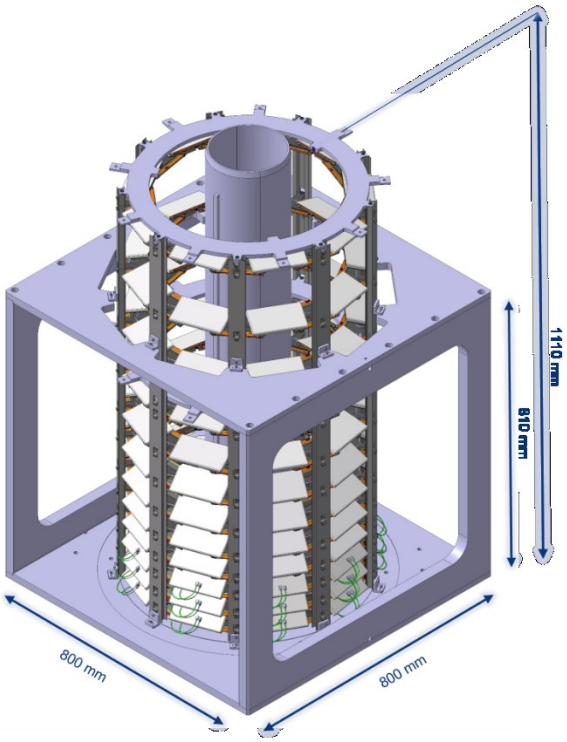

Figure 59. A completed assembly of a tilted TBPS section. [41]

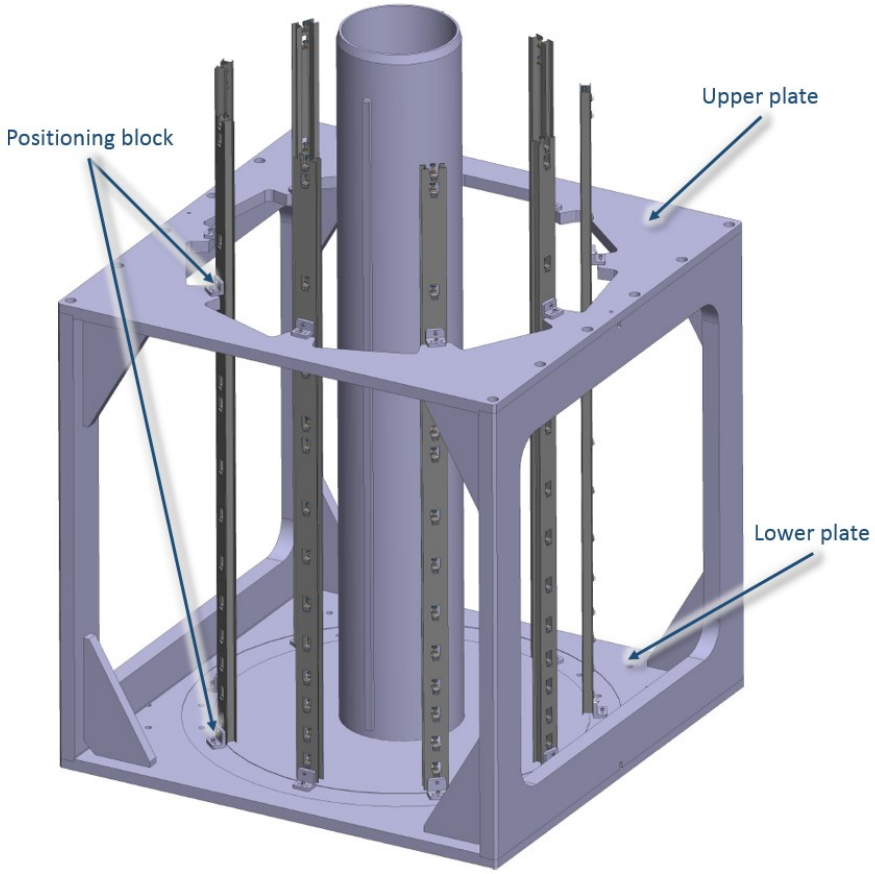

Figure 60. Tilted TBPS assembly frame.

The variation of the ring's positions in a layer depends largely on quality of the assembly frame. Thus, the dimensional measurements can be divided into the measurement of the assembly frame, and the measurement of the stack of rings.

Three of the beams are used as references for positioning the rings. Positioning of these beams is exceedingly important. The beams are located in the assembly frame by positioning blocks as shown in Figure 60.

Figure 61 displays a bracket that is used to attach a ring to the supporting beam. On the three reference beams, these brackets are mounted on precisely manufactured holes to guarantee correct positioning of the rings. The other six beams will have brackets that are adjustable.

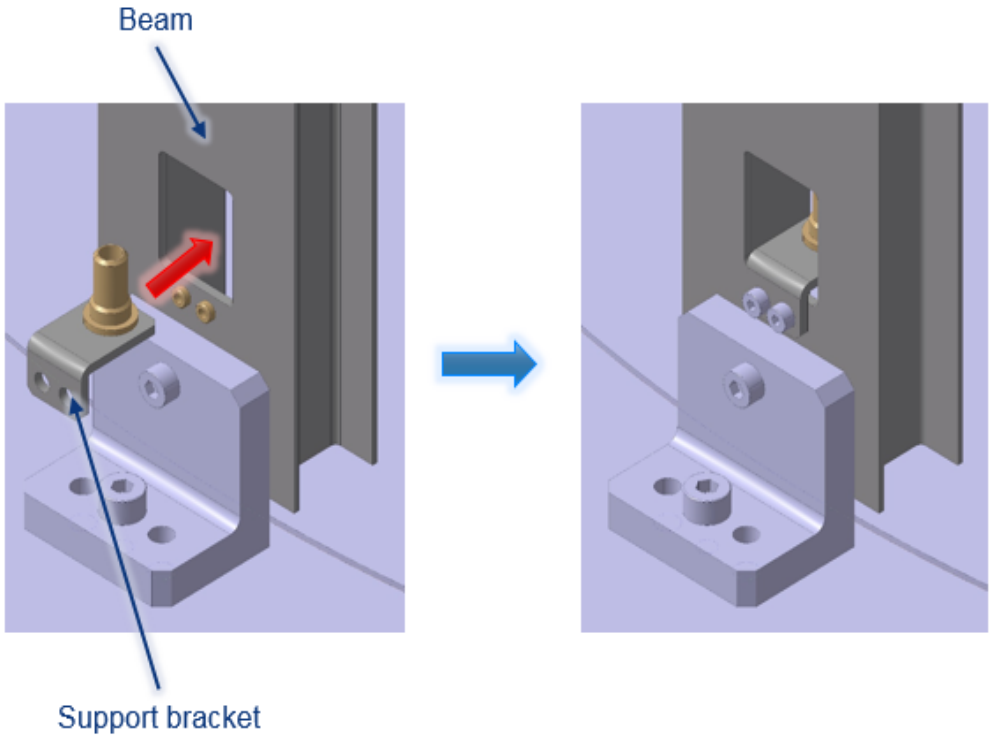

Figure 61. Support brackets used for attaching the rings on the beams. [41]

Table 14. Factors affecting the choice of measurement method for a tilted TBPS layer. Restrictive factors are shown in bold. Important but non-restrictive factors are displayed in brackets.

Factors affecting the choice of measurement method for tilted TBPS layer				
Group	Task requirements	Part restrictions	Environmental conditions	Other
Factors	**Accuracy** **Reliability** **Number of points** **Location of points** (Number of measurements)	**Dimensions** **Accessibility** (Material)	(Temperature) (Vibrations) (Available space) (Ambient lighting) (contamination)	(Price) (Ease of use)

Factors affecting the choice of measurement method for a tilted TBPS layer are displayed in Table 14. The measurement object is demanding, because of the combination of a relatively high accuracy requirement and large dimensions. The number and location of measurement points become restrictive when optical measurement methods are considered. As mentioned before, these systems require mounted targets for measuring points, and their possible locations are not very flexible in this assembly.

4.5.1 Task requirements

The accuracy and reliability requirements for TBPS layers dimensional measurement result from the tolerances associated with positioning the rings. A more definitive value for these tolerances can be given after prototypes of the rings have been measured, but the tolerances can roughly be expected to be in the range of 100 μm – 500 μm.

The accuracy of the measurement system should be chosen so that measurement uncertainty is within reasonable margins when measurements indicate that a dimension is at its tolerance limits. For example, if the accuracy of a measurement system is 30 μm and a 50 mm dimension with a tolerance of ±100 μm is measured to be 50.10 mm, the impact of the dimension actually being 50.13 mm has to be evaluated.

Small uncertainties of module positioning in the tracker volume can result in minor losses of hermeticity, rather than a catastrophic failure of the tracker. Because of this, the loss of accuracy in a magnitude described above can only have a marginal effect on overall tracking capability.

The quality of the tilted TBPS assembly frame depends mostly on the planarity of the lower and upper plates and the position and size tolerances of the holes related to the positioning blocks of the reference beams. As for the reference beams, the most important dimension are the positioning of the beam inserts that join the beam to the positioning blocks of the frame, and holes to which the ring support brackets are fixed. Of course, the dimensions of the positioning blocks and support brackets are crucially important as well.

The quality of the assembly frame, positioning blocks, supporting brackets and beams is crucial for the successful assembly of a tilted TBPS section. Fortunately, such components can be manufactured relatively easily with high dimensional accuracy. The measurement accuracy of these components should reflect this, and using a CMM for their dimensional quality control seems to be the best choice.

However, when assembling the layer it would be beneficial to measure the position of each ring after it has been inserted into the frame. This requires that the measurement is done at the assembly site. Transporting the assembly into a metrology laboratory for a CMM measurement after each ring insertion is quite unpractical, risky and time-consuming and can therefore be ruled out.

4.5.2 Part restrictions

The dimensions of a TBPS tilted sections and the frames used to assemble them vary between the layers. The dimensions shown in Figure 58 and Figure 59 are for layer 1; the frames for layer 2 and 3 have not been designed yet. The restriction that the frame and layer dimensions can impose is whether they can be measured in an available CMM or not.

The dimensions of layer 1 assembly frame are 800 mm x 800 mm x 810 mm in x-y-z, and the radius of a ring in the first layer is approximately 600 mm. As the radius of a ring in layer 3 is approximately 1150 mm, it can be assumed that the assembly frame of layer 3 will have dimensions in the range of 1350-1500 mm x 1350-1500 mm x 810 mm

in x-y-z. The measuring range of the larger Zeiss CMM at the CERN metrology lab is 1600 mm X 3000 mm X 1000 mm in x-y-z, so it can be concluded that the layers and their assembly frames can be measured with a CMM at CERN in terms of their dimensions.

Accessibility can be a restrictive factor when considering target placement for optical measurement systems. The targets would have to be placed so that their position can be linked to the position of the modules through measured dimensions of the rings. In addition, the targets need to be easily distinguishable; preferably from outside of the layer.

4.5.3 Measurement setup

As mentioned before, the positioning blocks, supporting brackets and beams will be made with high precision and they fit into the available CMMs. As such, the best option to measure them at CERN is with one of the available Zeiss machines. The detailed measurement process of these parts is rather unambiguous and not covered in this analysis.

Because the assembly frames dimensions are critical for assembling the layers accurately and because their dimensions allow it, the frames should also be measured with a CMM. The important measures to take are the relative positions and parallelism between the lower and upper plates, flatness of both plates and positioning block attachment hole dimensions and positions.

The most critical aspect of a layers assembly is how the rings are positioned in relation to each other. Quality assurance of the assembly frame is more of an auxiliary operation in the assembly, while ring insertion is the primary operation. Assuring that a ring has been placed properly after insertion can save time in comparison to just assuring the quality of the final assembly. Because utilizing a CMM is not a viable option, alternative systems have to be considered.

Two possible options remain for the measurement system: laser based systems and photogrammetry. As mentioned before, the accuracy requirement is approximately 30 μm and based on discussions with the CERN survey team, both of the options should fulfill this criterion. A laser based system would need several theodolites installed around the assembly frame for measurements, and would likely require expert availabilty for operation. Conversely, photogrammetry is easy to use and can be operated by the personnel assembling the layers. Because of these reasons, photogrammetry is the more viable option for measuring the TBPS layer during assembly.

Because successful photogrammetric measurements demand that multiple targets are seen in all images (at least three), the number of targets should be high. The targets should also be positioned such that their positions can be linked to the measurements of a ring and ultimately to the positions of the modules themselves.

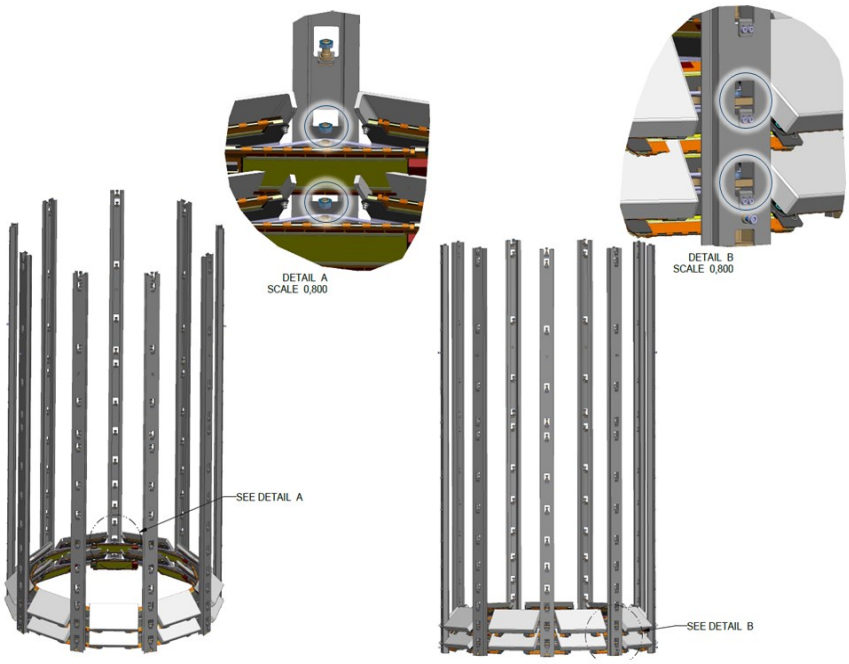

Figure 62. Suitable photogrammetry target positions shown encircled in a TBPS tilted section. Photogrammetric targets are placed in all 9 ring-fixing locations.

Suitable target locations are depicted in Figure 62. A fixture is inserted in place of the encircled nuts that protrudes through the beams and allows a target to be fixed so that it is "outside" the layer. Placing a target to each of these nine positions that fix a ring to the beams allows multiple targets to be seen in images captured around the layer. This has also the advantage that the target positions link directly to other dimensions of the ring and ultimately to the module positions, as the ring ear hole positions are measured in relation to other ring dimensions, when the quality of the ring is measured and recorded (4.6.3).

4.6 Dimensional measurement requirements of a single ring

The most important factors affecting the choice of a measurement system for a tilted TBPS ring are displayed in Table 15. Out of the three measurement objects,

Table 15. Factors affecting the choice of measurement method for a tilted TBPS ring. Restrictive factors are shown in bold. Important but non-restrictive factors are displayed in brackets.

Factors affecting the choice of measurement method for TBPS tilted ring				
Group	Task requirements	Part restrictions	Environmental conditions	Other
Factors	**Accuracy** **Reliability** (Number of points) (Location of points) (Number of measurements)	(Dimensions) (Accessibility) (Material)	(Temperature) (Vibrations) (Available space) (Ambient lighting) (contamination)	(Price) (Ease of use)

the measurement method choice of a ring is the least constrained by task requirements and part restrictions. While the stringent tolerances of the rings demand that the measurement system is highly accurate, the dimensions of the rings allow them to be measured with the available CMMs.

Quality assurance of TBPS tilted rings is critical because uncertainties in module positions on them stack-up to the assembly sequence of producing a layer and ultimately to the complete TBPS. As ring manufacturing and layer production both cause dimensional variation to the modules in z and r, a balance has to be found when setting tolerances for these two assemblies. Out of the two, the rings can be manufactured with a higher precision. As such, the tolerances of the ring can be expected to be in the range of 25 µm – 150 µm.

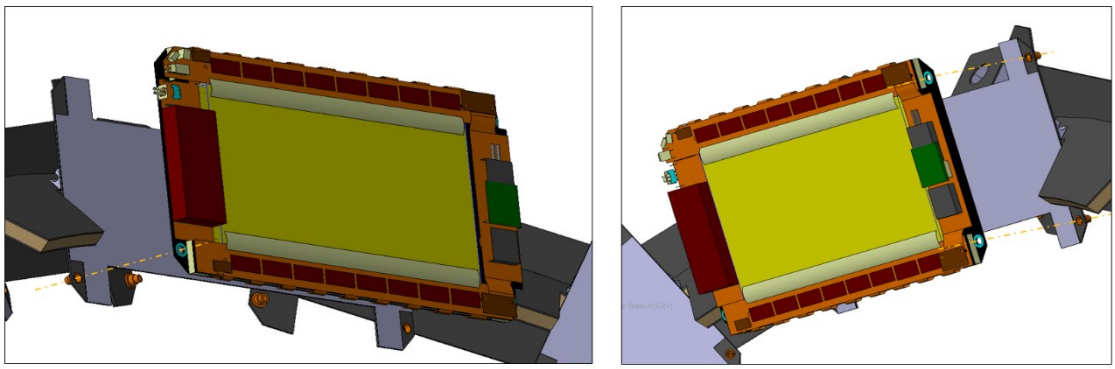

Figure 64. Module insertion to a tilted TBPS ring A module is located on the ring by three pairs of inserts and screws. One set is visible in the left image and the two others in the right image.

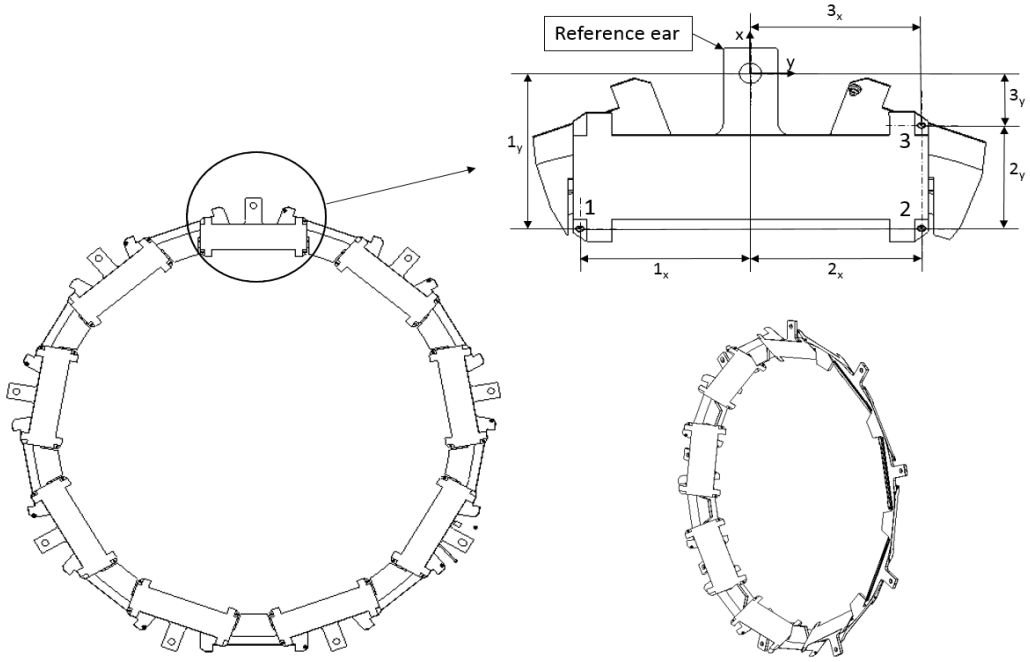

Figure 63. Dimensional measurement of three insert positions on a ring. The inserts are labeled with numbers from 1-3. Z-coordinate measurements not shown. The reference coordinate system is determined from three reference ear holes in the ring.

The modules will be mounted on the rings via three inserts and shoulder screws as shown in Figure 64. These determine the position of a module on a ring, while the ring's reference ears (see Figure 63) determine the ring's position in a TBPS tilted layer. Hence, the most important dimensions to measure are all of the inserts positions in relation to holes on reference ears (see Figure 63) and the three reference ear holes relative positions.

An important distinction about the quality assurance of the rings is that they will ultimately be manufactured at a location other than CERN. Because of this, the location where they will be manufactured at should have the capability to perform quality assurance similar to what is described in this chapter, which deals with measuring the prototypes of the rings. Consequently, the restrictions of measurement system selection are viewed from the perspective of methods available at CERN.

4.6.1 Task requirements

As mentioned before, precision in the range of 25 μm – 150 μm can be expected for the ring dimensions. This imposes a relatively strict requirement on the accuracy of the measurement system, which should optimally be an order of magnitude more accurate than the precision of the features it measures.

Other than the accuracy requirement, no strict task requirements can be identified for the ring. The number of measurement points and measurements should of course be high to increase reliability of the results, but this does not restrict the selection of a measurement system.

4.6.2 Part restrictions

The choice of a measurement system is also not that constrained by part restrictions either. The radii of the rings range from 600 mm to 1150 mm depending on which layer the ring is in. The rings should optimally be supported vertically for measurements, which might pose a restriction depending on if a CMM with such a measurement range is available. CERN's Zeiss CMMs described in 4.2.1 have large enough measuring ranges for the rings, the dimensions of the rings are therefore not viewed as a restrictive factor.

4.6.3 Measurement setup

Based on the task requirements and part restrictions, measuring the rings with a CMM is the best option. This section will describe how to perform the measurements in detail so that the rings quality can be assured according to the tolerance allocation in 3.6, and so that photogrammetric target positions can be related to other measurements of the ring.

To ensure accurate measurements, the rings can be fixed vertically on the CMM measuring volume so that both sides can be measured without turning the ring around. This requires a special fixture to which the rings can be attached.

Similar reference points can be used as in 3.6 to determine the measurements (see Figure 65). The ring reference center can be measured from a circle formed by the positions of the holes in the three reference ears. Similarly, the module reference centers

can be measured from the positions of the three module fixing insert holes on each cooling plate.

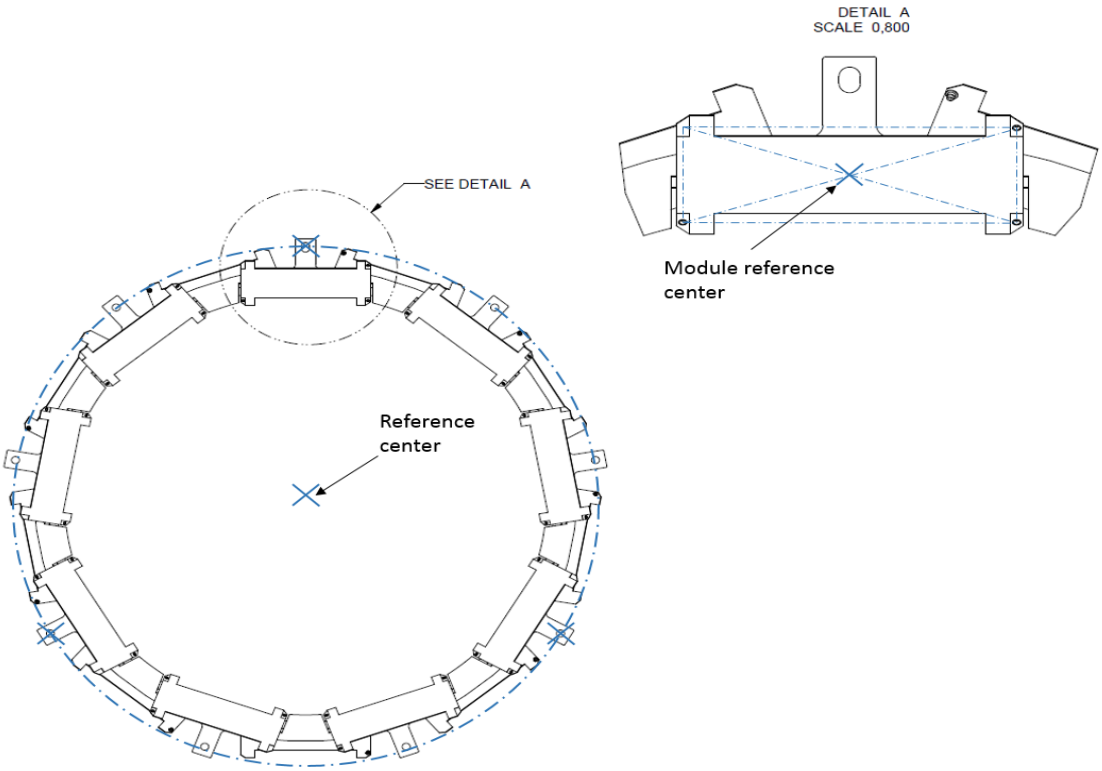

Figure 65. Ring reference center and module reference center.

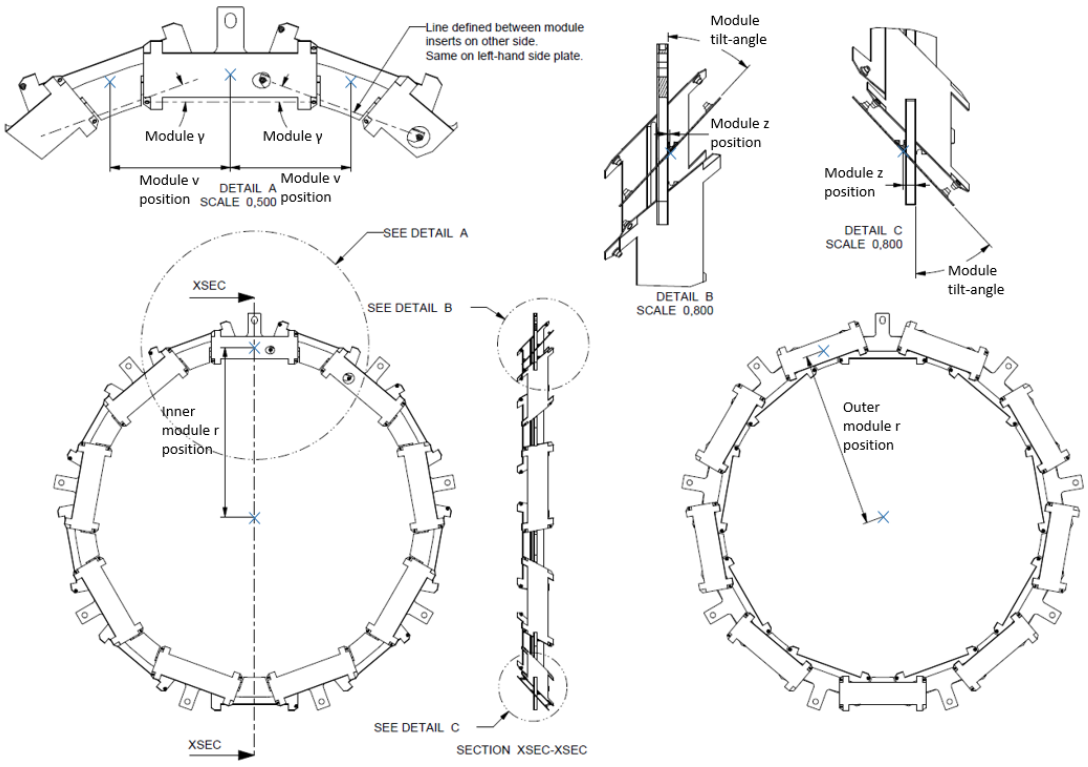

Figure 66. Detailed representation of ring measurements.

The detailed view of which measurements should be taken is shown in Figure 66. Inner and outer module positions in r should be measured as the distance between the

rings reference center and the module reference centers. The relative module reference center positions in v of successive cooling plates should be measured as shown in detailed view A. The module z positions can be measured as the distance between the module reference centers, and the defined plane of the ring, as shown in detailed views B and C. Note that this reference plane is defined from the three reference ears, not the physical, closest surface of the ring.

Cooling plate γ orientation should be measured as the angle between lines that are formed by lower (in the figure) module inserts of two consecutive cooling plates. Module tilt angles are to be measured as the angle between the plane of the cooling plate, and the defined plane of the ring. The cooling plate plane should be formed from measurements taken from the rigid center region of the plate that finally will be in contact with the detector module.

And finally, all the ring's ear holes should be measured with respect to the ring's reference ear holes. This is because photogrammetric targets may later be attached to any of these holes during the TBPS layer assembly phases, and used for measuring and monitoring of the geometry and possible deformations of the assembled TBPS sub-sections

5 Discussion

The most prominent findings of this thesis were the tolerance magnitudes and sensitivities of the sensor module positions in the TBPS sub-section, and the design of how to dimensionally measure the TBPS structure. Additionally, it was demonstrated that an abstracted feature based model of a particle trackers hermeticity can be used to allocated tolerances for the support structure of said trackers.

This is the first time that a tilted sensor module geometry is realized in a particle tracker, and no previous knowledge of best practices is available. This new tracker geometry will eventually save millions of euros when the upgraded CMS tracker is built, because of the smaller number of expensive modules used in the tracker volume. However, this geometry results in an exceedingly more complex mechanical support structure for the tilted modules, which contributes to more uncertainty in the trackers design.

Foremost, the allocated tolerance values for the TBPS support structure imply that the designed structure can be manufactured with reasonable methods so that tracker hermeticity is mostly retained. Secondly, the tolerance values give clear goals of what to aim for when manufacturing the parts of the structure, and provide a guideline for deciding on what is good enough and what must be scrapped.

Because the TBPS structure is still in its design phase, there are bound to be changes in the future that affect the tolerance values. For example, it might be found out through prototyping that a certain tolerance should be larger because of manufacturing issues, while some other tolerances could be tightened. This is where the results of the sensitivity analysis come into play. The sensitivity magnitudes offer designers guidelines on how to make future changes to the sensor positions or the tolerances of the sensor positions.

However, the allocation of tolerances is not enough. It must also be ensured that the manufactured structures conform to the allocated tolerances, which is achieved by dimensionally measuring the structures. While this process is quite unambiguous for small generic parts, larger structures need a more comprehensive analysis on which methods to use and how. For this purpose, a thorough plan was designed for the dimensional measurement of the TBPS in various assembly stages.

The abstracted feature based model that was constructed did not account for dimensional changes due to thermal effects in the support structure. While the structural material of the support structure (CFRP) exhibits a low coefficient of thermal expansion, it must be stated that the presented tolerance values are slightly warped in reality because of the 55 °C change in temperature that is imposed on the CMS tracker. Further research is needed on how this temperature change affects the dimensions of the TBPS support structure.

Additionally, the described perturbation method used a similar bias throughout a layer for dividing the tolerance space of a module between different degrees of freedom. A more sophisticated model would have adjusted this bias between the degrees of freedom for each module depending on the sensitivity magnitudes of dimensions exhibited on that module. This is evident for example in the allocation of tolerances of ring positions: a

general bias was initialized for allowing tolerances in z to be larger than tolerances in r. Because the trackers hermeticity was more sensitive to ring position changes in r in rings furthest away from the IP, this method resulted in quite stringent tolerances in r in those particular rings. Furthermore, the model treated module positioning tolerances acquired from φ-overlap analysis and ring positioning tolerances acquired from z-coverage analysis separately. It is evident that these two hermeticity requirements are linked not only through z-overlaps effect on φ-overlap, but also through the effect that module positioning in z and r has on z-coverage. For tolerance optimization purposes, a more sophisticated model should be devised, or the existing model improved.

6 Summary and Conclusions

In this thesis, a tolerance synthesis method was developed for the dimensional and geometrical tolerance allocation of a particle tracker's mechanical construction. A plan for corresponding dimensional measurements at various assembly stages was also presented. Based on a literature review of various tolerance analysis methods, an abstracted feature based model was selected as the most suitable method for this use-case. The model was developed using Matlab and utilized for calculating tolerance sensitivities and allocating tolerances for the support structures of the tilted TBPS sub-detector of the future CMS tracker at CERN. The tilted TBPS is a novel concept with detector modules inclined towards the proton-proton beam collision point. Such tilted arrangement is attractive for many reasons, but complex for the mechanics and such detectors have not been made before. Studying the dimensional quality requirements, and setting the mechanical tolerances appropriately is essential for this ambitious project.

The tolerance analysis was primarily based on the hermeticity requirement of the tracker. This functional requirement states that the neighboring silicon sensors in the tracker's layers must always have small overlap, so that a particle originating from a proton-proton collision in a region of ±70 mm around the nominal collision point cannot traverse any of the trackers layers without hitting at least one of the active silicon sensor areas. This functional requirement was shown to consist of two separate requirements: z-coverage and φ-overlap. Z-coverage is an entity that describes the distribution of collisions around the nominal collision point that are covered by the tracker's layers. This functional requirement was shown to dictate how individual rings must be positioned in relation to each other in the tilted TBPS. Conversely, φ-overlap is a measure of sensor overlap on a single ring in the tilted TBPS. While z-coverage dictates how rings are positioned in relation to each other, φ-overlap sets restrictions on the positions of the actual sensor modules on each ring.

The analysis of z-coverage revealed that ring translational tolerances in z and r correlated most strongly with the achieved z-coverage results. Variation in module tilt angle was shown to have a relatively small effect on z-coverage. The tolerance values related to z-coverage indicated that the functional requirement of z-coverage = ±70 mm could not be fulfilled in layer 3 of the TBPS tilted section. Results of lowering the z-coverage requirement to ±65 mm were shown: the tolerance values in this configuration were around 100 µm.

In terms of fulfilling the ±70 mm z-coverage requirement, the intersection between the TBPS flat section and tilted section also exhibits very tight tolerances. As a result, explicit care should be taken when designing the methods of precisely joining these two sections together. Even so, one may expect that the z-coverage requirement cannot be fully achieved between the flat and tilted sections.

Sensitivity analysis of tolerances related to φ-overlap indicated that module variation in γ contributed the most towards φ-overlap. Translational variation in z and r, and rotational variation in β also correlated with the end φ-overlap, but the magnitude of the correlation was much lower. Z-overlap's correlation to φ-overlap was significant in layers

where z-overlap was allowed to vary by a large magnitude. Rotational variation around the y-axis was shown to have little effect on φ-overlap. (The reader is referred to Figure 37 for explanations of the translational and rotational directions.)

A sample of tolerance values regarding module positioning on a ring were show. These tolerance values were calculated so that φ-overlap remained positive. While the values appeared to be quite strict in some rings, they should still be achievable as the rings are single glued units, manufactured with the help of jigs, which are machined with high precision.

Chapter 4 analyzed the requirements and restrictions related to the dimensional measurement system selection for various sub-assemblies of the TBPS. The factors affecting the choice were assessed based on the current state-of-the-art of large-scale metrology, and the systems available at CERN. The most suitable measurement systems were identified for the measurement of: the complete TBPS, a TBPS tilted layer and a single TBPS tilted ring. Accuracy and reliability were identified as restrictive factors in all of the measurement tasks.

Along accuracy and reliability, location of measurement points and object dimensions were identified as the most important restrictive factors for the complete TBPS measurement system selection. Because the dimensions of the object disqualified the use of a CMM, photogrammetry was identified as the best alternative option. The dimensional measurement plan for the complete TBPS was divided into two segments: the quality assurance of the tilted – flat section junction, and the quality assurance of attaching the complete TBPS layers together. The former of these was concluded as more critical, because of the tight tolerances associated with the transition from the flat section to the tilted sections. A mixed use of photogrammetry and an inside micrometer was determined to be the best solution for measuring this junction.

The accuracy with which the complete TBPS layers are attached together was not found to be affected by the functional requirements related to hermeticity. Rather, the dictating functional requirement for these junctions is that the complete TBPS does not exceed its maximum dimensions, so as to properly fit into the space allocated for it in the CMS tracker. Because of the relatively large dimensions of the complete TBPS, a photogrammetry based measurement setup was concluded as the best solution.

As for the TBPS tilted layer, a mixed use of a CMM and photogrammetry was determined to be the best solution for carrying out the measurements. The location of measurement points and ease of use were the primary factors affecting this choice, along with accuracy and reliability. The layers of the tilted TBPS are to be assembled in dedicated metallic assembly frames, which are machined with precision. It was concluded that these assembly frames should be measured with a CMM, to ensure high accuracy. The optimal method for measuring the layers was determined to measure the position of each ring in situ after it has been placed in the assembly frame. The use of CMM was identified as impractical for this purpose, and so a photogrammetric system was considered most suitable. An analysis of target placement in a TBPS layer was carried out to demonstrate how to achieve the needed accuracies via photogrammetry.

The tilted rings were not all that restricted by part attributes or task requirements. The most important factors for the measurement of the rings were accuracy and reliability. Fulfilling these requirements was shown to be possible by measuring the rings with the available CMMs at the CERN metrology laboratory. A comprehensive study on how the rings should be measured in a CMM was presented.

In the future, tolerance analysis for other parts of the CMS tracker can be done by integrating the developed perturbation-based model into the existing tkLayout tool, at CERN. Once tolerances have been allocated for other support structures, similar dimensional measurement plans should be developed for them as demonstrated here. The now proceeding prototyping of the tracker's sub-systems will be an important occasion to validate the mechanical tolerance requirements and update them where needed in view of the forthcoming final production phase.

References

[1] P. K. Singh, P. K. Jain and S. C. Jain (2003) "Simultaneous optimal selection of design and manufacturing tolerances with different stack-up conditions using genetic algorithms" *International Journal of Production Research,* vol. 41:11, pp. 2411-2429, DOI: https://doi.org/10.1080/0020754031000087328.

[2] ASME (2009) "Dimensioning and Tolerancing - Y14.5" American Society of Mechanical Engineers

[3] ISO (2011) "EN ISO 8015:2011" European Committee for Standardization

[4] Sigmetrix (2018) "What Is Tolerance Analysis?" [Online], Available: http://www.sigmetrix.com/what-is-tolerance-analysis/. [Accessed July 2018]

[5] K. W. Chase, J. Gao and S. P. Magleby (1995) "General 2-D Tolerance Analysis of Mechanical Assemblies with Small Kinematic Adjustments" *Journal of Design and Manufacturing*

[6] Z. Shen, G. Ameta, J. J. Shah and J. K. Davidson (2005) "A Comparative Study of Tolerance Analysis Methods" *Journal of Computing and Information Science in Engineering,* vol. 5, pp. 247-256, DOI: https://doi.org/10.1115/1.1979509

[7] Z. Shen, J. J. Shah and J. K. Davidson (2008) "Automatic generation of min/max tolerance charts for tolerance analysis from CAD models" *International Journal of Computer Integrated Manufacturing,* vol. 21, pp. 869-884, DOI: https://doi.org/10.1080/09511920802023004

[8] J. J. Shah, G. Ameta, Z. Shen and J. Davidson (2007) "Navigating the Tolerance Analysis Maze" *Computer-Aided Design and Applications,* vol. 4:5, pp. 705-718, ISSN: 1686-4360

[9] 3DCS (2018) "3DCS Variation Analyst - The Industry Leading Integrated Tolerance Analysis Software" [Online], Available: http://www.3dcs.com/tolerance-analysis-software-and-spc-systems/3dcs-software. [Accessed July 2018]

[10] Sigmetrix (2018) "CETOL 6sigma Tolerance Analysis Software" [Online], Available: http://www.sigmetrix.com/products/cetol-tolerance-analysis-software/. [Accessed July 2018]

[11] Siemens (2018) "Tecnomatix", [Online], Available: https://www.plm.automation.siemens.com/global/en/products/tecnomatix/. [Accessed July 2018]

[12] J. K. Davidson, A. Mujezinovic and J. J. Shah (2002) "A New Mathematical Model for Geometric Tolerances as Applied to Round Faces" *Journal of*

Mechanical Design, vol. 124, pp. 609-622, DOI: https://doi.org/10.1115/1.1497362

[13] J. Gao, W. K. Chase and S. P. Magleby (1998) "Generalized 3-D tolerance analysis of mechanical assemblies with small kinematic adjustments" *IIE TRANSACTIONS,* vol. 30:4, pp. 367-377, DOI: https://doi.org/10.1080/07408179808966476

[14] K. W. Chase, J. Gao, S. P. Magleby and C. D. Sorensen (1996) "Including Geometric Feature Variations in Tolerance Analysis of Mechanical Assemblies" *IIE TRANSACTIONS,* vol. 28:10, pp. 795-807, DOI: https://doi.org/10.1080/15458830.1996.11770732

[15] M. Marziale and W. Polini (2009) "A review of two models for tolerance analysis of an assembly: vector loop and matrix" *The international Journal of Advanced Manufacturing Technology,* vol. 43, pp. 1106-1123, DOI: https://doi.org/10.1007/s00170-008-1790-0

[16] A. Mujezinovic, J. K. Davidson and J. J. Shah (2004) "A new Mathematical Model for Geometric Tolerances as Applied to Polygonal Faces" *Journal of Mechanical Design,* vol. 126, pp. 504-518, DOI: https://doi.org/10.1115/1.1701881

[17] P. Lafond and L. Laperriere (1999) "Jacobian-based Modeling of Dispersions Affecting Pre-Defined Functional Requirements of Mechanical Assemblies" *Proceedings of the 1999 IEEE International Symposium on Assembly and Task Planning,* DOI: https://doi.org/10.1109/ISATP.1999.782929

[18] M. Marziale and W. Polini (2011) "A review of two models for tolerance analysis of an assembly: Jacobian and torsor" *International Journal of Computer Integrated Manufacturing,* vol. 24:1, pp. 74-86, DOI: https://doi.org/10.1080/0951192X.2010.531286

[19] J. J. Shah (2013) "Tolerance Map Models for Design and Manufacturing", *Arizona State University*, [Presentation]

[20] The CMS collaboration (2017) "The Phase-2 Upgrade of the CMS Tracker, Technical Design Report", CMS-TDR-17-001

[21] The CMS collaboration (2010) "Alignment of the CMS silicon tracker during commissioning with cosmic rays" *Journal of Instrumentation, vol. 5,* DOI: https://doi.org/10.1088/1748-0221/5/03/T03009

[22] A. Saltelli, M. Ratto, T. Andres et. al (2008) "Global Sensitivity Analysis: The Primer", [Print], Chichester: John Wiley & Sons Ltd, ISBN: 978-0-470-05997-5

[23] J. Gibbons and S. Chakraborti (1971) "Nonparametric Statistical Inference", [Print], New York: Marcel Dekker, Inc., p. 422, ISBN: 0-8247-4052-1

[24] Mitutoyo USA (2018) "CRYSTA-Apex EX 1200R Series 191-Revo Equipped 5-Axis CNC CMM", [Online], Available:

https://ecatalog.mitutoyo.com/CRYSTA-Apex-EX-1200R-Series-191-Revo-Equipped-5-Axis-CNC-CMM-C1841.aspx. [Accessed July 2018]

[25] The CMS collaboration (2014) "Alignment of the CMS tracker with LHC and cosmic ray data" *Journal of Instrumentation, vol 9,* DOI: https://doi.org/10.1088/1748-0221/9/06/P06009

[26] V. Karimäki, T. Lampén and F. P. Schilling (2006) "The HIP Algorithm for Track Based Alignment and its Application to the CMS Pixel Detector", CMS NOTE 2006/018

[27] I. Belotelov et al (2006) "Simulation of Misalignment Scenarios for CMS Tracking Devices," CMS NOTE 2006/008

[28] T. Lampén, J. Huotari (2018) *Interview about CMS Tracker alignment* [Interview]. 28 March 2018.

[29] R. Schmitt et. al, (2016) "Advances in Large-Scale Metrology – Review and future trends," *CIRP Annals - Manufacturing Technology,* vol. 65*,* pp. 643-665, DOI: https://doi.org/10.1016/j.cirp.2016.05.002

[30] Hexagon (2018) "DEA LAMBDA SP - The high-tech giant CMM,", [Online], Available: http://www.hexagonmi.com/products/coordinate-measuring-machines/gantry-cmms/dea-lambda-sp. [Accessed 8 May 2018]

[31] E. Savio, L. De Chiffre and R. Schmitt (2007) "Metrology of freeform shaped parts", *Annals of the CIRP,* vol 56:2, pp. 810-835, DOI: https://doi.org/10.1016/j.cirp.2007.10.008

[32] C. Schneider, M. Engelhardt (2004) "LaserTracer - A new type of self tracking laser interferometer" *AICON 3D Systems GmbH,* [Presentation]

[33] Nikon (2017) "iGPS - Factory-wide measuring, positioning and tracking system" [Online], Available: https://www.nikonmetrology.com/en-us/product/igps. [Accessed May 2018]

[34] W. T. Estler, K. L. Edmundson, G. N. Peggs and D. H. Parker (2002) "Large-Scale Metrology - An update," *CIRP Annals - Manufacturing Technology,* vol. 51:2, pp. 587-609, DOI: https://doi.org/10.1016/S0007-8506(07)61702-8

[35] Hexagon (2018) "AICON MoveInspect DPA", [Online], Available: http://aicon3d.com/products/moveinspect-technology/aicon-moveinspect-dpa. [Accessed May 2018]

[36] T. Luhmann (2010) "Close range photogrammetry for industrial applications", *Journal of Photogrammetry and Remote Sensing,* vol. 65:6, pp. 558-569, DOI: https://doi.org/10.1016/j.isprsjprs.2010.06.003

[37] Zeiss (2017) "ZEISS PRISMO Specifications", [Online], Available: https://www.zeiss.com/metrology/products/systems/coordinate-measuring-machines/bridge-type-cmms/prismo.html. [Accessed May 2018]

[38] Zeiss (2018) " ZEISS O-INSPECT", [Online], Available: https://www.zeiss.com/metrology/products/systems/optical-systems/o-inspect.html. [Accessed May 2018]

[39] A. Behrens (2018) "Surveyors work for CMS with mobile systems,", *Experiment metrology team - EN/SMM-ESA,* [Presentation]

[40] W. Cuypers et al (2008) "Optical measurement techniques for mobile and large-scale dimensional metrology," *Optics and Lasers in Engineering,* vol. 47:3-4, pp. 292-300, DOI: https://doi.org/10.1016/j.optlaseng.2008.03.013

[41] Hexagon Metrology (2013) "LEITZ PMM-C LINE Ultra high accuracy coordinate measuring machines", [Online], Available: https://www.hexagonmi.com/products/coordinate-measuring-machines/bridge-cmms/leitz-pmmc, [Accessed May 2018]

[42] K. Cichy et. al (2016) "Concept of a Tilted Barrel for the CMS Tracker Phase 2 Upgrade", [Presentation]

[43] A. Perez et. al (2018) "Assembly of the TBPS tilted sections, Option 3″, [Presentation]

[44] CERN (2014) "CMS", [Online], Available: https://home.cern/about/experiments/cms. [Accessed July 2018].

[45] CERN (2014) "About CMS", [Online], Available: https://cms.cern/detector. [Accessed July 2018].

[46] R. Tomas, G. Arduini, L. Medina and L. Rossi (2018) "HL-LHC: Machine upgrade plans," *ACES common ATLAS CMS electronics workshop for LHC upgrades*, [Presentation]

[47] Hexagon (2018) "Leitz PMM-G", [Online], Available: https://www.hexagonmi.com/products/coordinate-measuring-machines/gantry-cmms/leitz-pmmg. [Accessed August 2018]

Appendix A

The abstracted feature based model developed in Matlab can be found in: https://github.com/jannehuotari/TBPS_tilted_sensitivity_analysis.git.

To figure out the polynomial of a trajectory with the best z-coverage, while still fulfilling the stub finding requirement, we need to express the coordinates of points 1-8. From here on, the sensors will be expressed by their end points (the rightmost sensor in Figure 30 would be expressed as $sensor_{15}$) and points will be expressed as P1, P2 and so on.

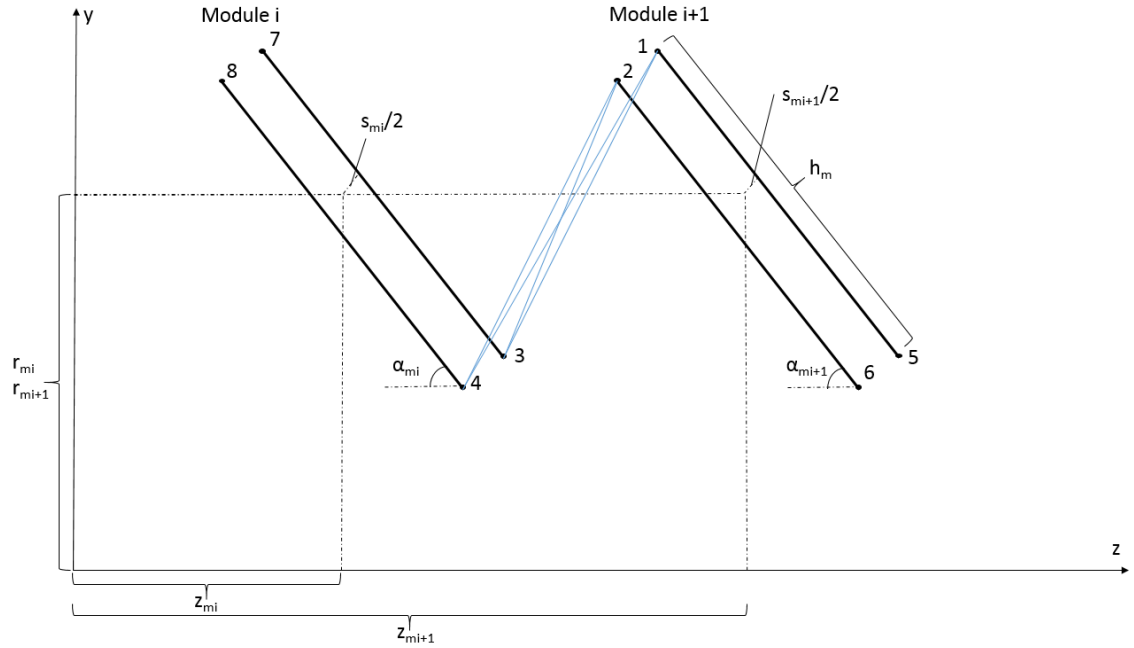

Figure A 1. Z-coverage requirements in more detail. Black lines depict sensors in a single module. Particle trajectories must hit both of the sensors on a module to enable stub finding. r_m = module position in y, z_m = module position in z, α_m = module tilt angle & s_m = module sensor spacing.

The center-points of the sensors are:

$$sensor_{15_z} = z_{mi+1} + \frac{s_{mi+1}*\sin(\alpha_{mi+1})}{2}, \quad sensor_{15_y} = r_{mi+1} + \frac{s_{mi+1}*\cos(\alpha_{mi+1})}{2}$$

$$sensor_{26_z} = z_{mi+1} - \frac{s_{mi+1}*\sin(\alpha_{mi+1})}{2}, \quad sensor_{26_y} = r_{mi+1} - \frac{s_{mi+1}*\cos(\alpha_{mi+1})}{2}$$

$$sensor_{37_z} = z_{mi} + \frac{s_{mi}*\sin(\alpha_{mi})}{2}, \quad sensor_{37_y} = r_{mi} + \frac{s_{mi}*\cos(\alpha_{mi})}{2}$$

$$sensor_{48_z} = z_{mi} - \frac{s_{mi}*\sin(\alpha_{mi})}{2}, \quad sensor_{48_y} = r_{mi} - \frac{s_{mi}*\cos(\alpha_{mi})}{2}$$

Coordinates of points 1-8 are:

$$P1_z = sensor_{15_z} - \frac{h_m * \cos(\alpha_{mi+1})}{2} \quad P1_y = sensor_{15_y} + \frac{h_m * \sin(\alpha_{mi+1})}{2}$$

$$P2_z = sensor_{26_z} - \frac{h_m * \cos(\alpha_{mi+1})}{2} \quad P2_y = sensor_{26_y} + \frac{h_m * \sin(\alpha_{mi+1})}{2}$$

$$P3_z = sensor_{37_z} + \frac{h_m * \cos(\alpha_{mi+1})}{2} \quad P3_y = sensor_{37_y} - \frac{h_m * \sin(\alpha_{mi+1})}{2}$$

$$P4_z = sensor_{48_z} + \frac{h_m * \cos(\alpha_{mi+1})}{2} \quad P4_y = sensor_{48_y} - \frac{h_m * \sin(\alpha_{mi+1})}{2}$$

$$P5_z = sensor_{15_z} + \frac{h_m * \cos(\alpha_{mi+1})}{2} \quad P5_y = sensor_{15_y} - \frac{h_m * \sin(\alpha_{mi+1})}{2}$$

$$P6_z = sensor_{26_z} + \frac{h_m * \cos(\alpha_{mi+1})}{2} \quad P6_y = sensor_{26_y} - \frac{h_m * \sin(\alpha_{mi+1})}{2}$$

$$P7_z = sensor_{37_z} - \frac{h_m * \cos(\alpha_{mi+1})}{2} \quad P7_y = sensor_{37_y} + \frac{h_m * \sin(\alpha_{mi+1})}{2}$$

$$P8_z = sensor_{48_z} - \frac{h_m * \cos(\alpha_{mi+1})}{2} \quad P8_y = sensor_{48_y} + \frac{h_m * \sin(\alpha_{mi+1})}{2}$$

We then fit polynomials between the points on the sensors 1-5, 2-6, 3-7 and 4-8, and the between the points of possible trajectories 1-3, 1-4, 2-3 and 2-4. Subtracting the coefficients of two intersecting polynomials and solving the root of this resultant polynomial gives us the z-coordinate of the intersection point.

We solve the intersection z-coordinate of trajectory polynomial 1-3 with sensor polynomials 2-6 and 4-8, trajectory polynomial 1-4 with sensor polynomials 2-6 and 3-7, trajectory polynomial 2-3 with sensor polynomials 1-5 and 4-8 and trajectory polynomial 2-4 with sensor polynomials 1-5 and 3-7. Intersection z-coordinate will be denoted as polynomial z polynomial from here on. For example, intersection between 1-3 and 2-6 would be 1-3 z 2-6.

For the polynomials to fulfill the stub finding requirements, they have to fulfill the following conditions:

1-3: (1-3 z 2-6 > $P2_z$) & (1-3 z 4-8 < $P4_z$)

1-4: (1-4 z 2-6 > $P2_z$) & (1-4 z 3-7 < $P3_z$)

2-3: (2-3 z 1-5 > $P1_z$) & (2-3 z 4-8 < $P4_z$)

2-4: (2-4 z 1-5 > $P1_z$) & (2-4 z 3-7 < $P3_z$)

The polynomial that fulfills these conditions, is chosen and its z-value is calculated at y=0, to get the z-coverage.

Table A 1. Complete z-coverage related tolerances for layer 1.

Ring positional r & z tolerances layer 1 [mm]												
Ring	1	2	3	4	5	6	7	8	9	10	11	12
Inner module z-tolerance												
+	8,671	0,888	1,194	3,063	2,418	2,577	2,424	5,110	3,294	3,630	4,602	6,094
-	0,888	1,194	3,063	2,418	2,577	2,424	5,110	3,294	3,630	4,602	6,094	0,000
Inner module r-tolerance												
+	1,190	1,160	2,300	1,460	1,265	0,970	1,695	0,920	0,845	0,895	0,990	0,000
-	15,367	1,190	1,160	2,300	1,460	1,265	0,970	1,695	0,920	0,845	0,895	0,990
Outer module z-tolerance												
+	0,000	1,026	1,230	1,653	2,460	2,493	2,187	2,409	3,180	3,354	4,143	5,446
-	1,026	1,230	1,653	2,460	2,493	2,187	2,409	3,180	3,354	4,143	5,446	0,000
Outer module r-tolerance												
+	1,340	1,190	1,235	1,485	1,230	0,890	0,810	0,890	0,785	0,810	0,895	0,000
-	0,000	1,340	1,190	1,235	1,485	1,230	0,890	0,810	0,890	0,785	0,810	0,895

Table A 2. Complete z-coverage related tolerances for layer 2.

Ring positional r & z tolerances layer 2 [mm]												
Ring	1	2	3	4	5	6	7	8	9	10	11	12
Inner module z-tolerance												
+	9,052	0,492	0,594	2,145	0,792	0,855	1,065	2,604	1,137	1,356	1,422	1,878
-	0,492	0,594	2,145	0,792	0,855	1,065	2,604	1,137	1,356	1,422	1,878	0,000
Inner module r-tolerance												
+	0,540	0,525	1,590	0,500	0,460	0,495	1,050	0,405	0,420	0,390	0,450	0,000
-	11,891	0,540	0,525	1,590	0,500	0,460	0,495	1,050	0,405	0,420	0,390	0,450
Outer module z-tolerance												
+	0,633	0,483	0,537	0,582	0,774	0,786	0,948	0,855	1,065	1,215	1,206	1,593
-	0,483	0,537	0,582	0,774	0,786	0,948	0,855	1,065	1,215	1,206	1,593	0,000
Outer module r-tolerance												
+	0,530	0,480	0,435	0,490	0,425	0,445	0,345	0,380	0,380	0,330	0,385	0,000
-	0,885	0,530	0,480	0,435	0,490	0,425	0,445	0,345	0,380	0,380	0,330	0,385

Table A 3. Complete z-coverage related tolerances for layer 3.

Ring positional r & z tolerances layer 3 [mm]												
Ring	1	2	3	4	5	6	7	8	9	10	11	12
Inner module z-tolerance												
+	8,974	0,000	0,018	0,033	0,090	0,183	2,043	0,042	0,072	0,132	0,276	0,354
-	0,000	0,018	0,033	0,090	0,183	2,043	0,042	0,072	0,132	0,276	0,354	0,000
Inner module r-tolerance												
+	0,000	0,015	0,025	0,065	0,115	1,140	0,025	0,035	0,055	0,105	0,120	0,000
-	11,086	0,000	0,015	0,025	0,065	0,115	1,140	0,025	0,035	0,055	0,105	0,120
Outer module z-tolerance												
+	0,000	0,000	0,009	0,000	0,027	0,099	0,123	0,015	0,015	0,045	0,162	0,207
-	0,000	0,009	0,000	0,027	0,099	0,123	0,015	0,015	0,045	0,162	0,207	0,000
Outer module r-tolerance												
+	0,000	0,000	0,000	0,020	0,065	0,070	0,010	0,010	0,020	0,060	0,075	0,000
-	0,000	0,000	0,000	0,000	0,020	0,065	0,070	0,010	0,010	0,020	0,060	0,075

Appendix B

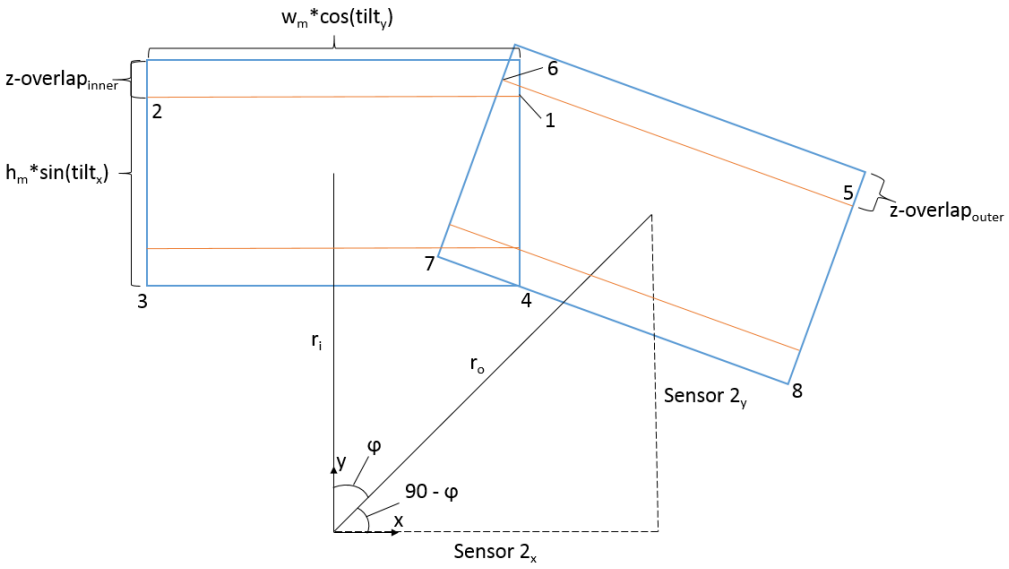

Figure B 1. General view of two consecutive modules in a ring. w_m is the width of a sensors active area, h_m the height of a sensors active area, r_i the inner modules back-side sensor position in r, r_o the outer modules front-side sensors position in r, $tilt_x$ the sensors rotation around the x axis (tilt angle) and $tilt_y$ the sensors rotation around the y-axis.

This first part of Appendix B will explain the calculation of points 1, 2, 4 and 6 positional coordinates. We know the values of r_i and r_o in Figure B 1, as well as values for the sensors positions in z, which we will denote as z_i and z_o (see appendix A).

The coordinates of points 1, 2 and 4 according to Appendix A are:

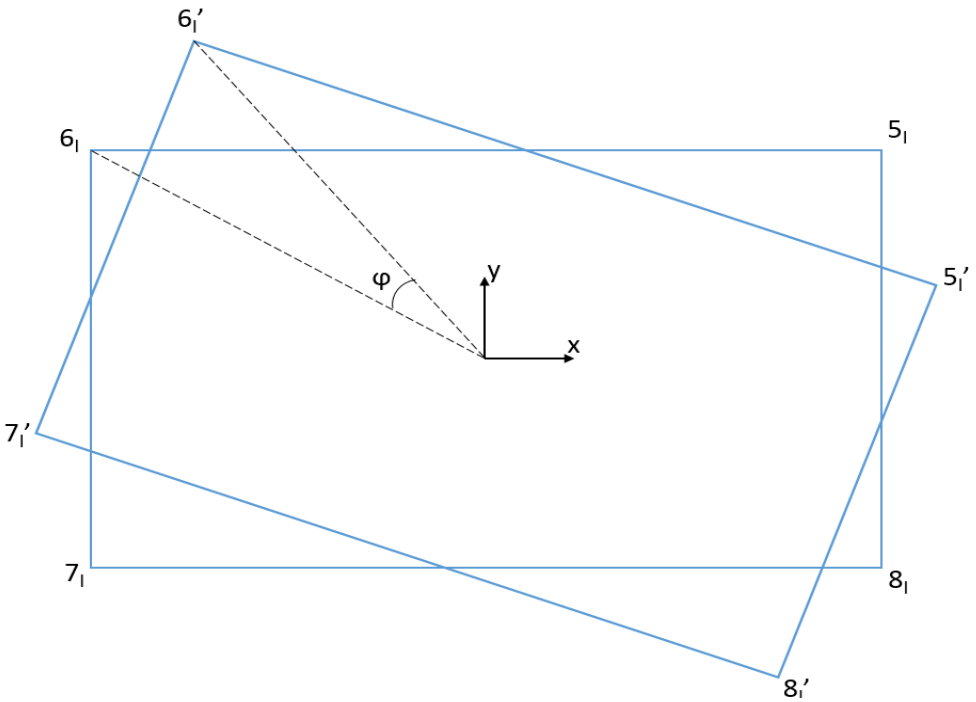

Figure B 2. Detailed view of right-side sensor.

$$P1_x = \frac{w_m}{2} * \cos(tilt_y)$$

$$P1_y = r_i + \left(\frac{h_m}{2} - zoverlap_{inner}\right) * \sin(tilt_x)$$

$$P1_z = z_i - \left(\frac{h_m}{2} - zoverlap_{inner}\right) * \cos(tilt_x)$$

$$P2_x = -\frac{w_m}{2} * \cos(tilt_y)$$

$$P2_y = r_i + \left(\frac{h_m}{2} - zoverlap_{inner}\right) * \sin(tilt_x)$$

$$P2_z = z_i - \left(\frac{h_m}{2} - zoverlap_{inner}\right) * \cos(tilt_x)$$

$$P4_x = \frac{w_m}{2} * \cos(tilt_y)$$

$$P4_y = r_i - \frac{h_m}{2} * \sin(tilt_x)$$

$$P4_z = z_i + \frac{h_m}{2} * \cos(tilt_x)$$

We can calculate the coordinates of point 6 by first figuring out its coordinates in the sensors local coordinate system (Figure B 2, 6_l') by utilizing a clock-wise rotation matrix for point 6_l:

$$\begin{bmatrix} x' \\ y' \end{bmatrix} = \begin{bmatrix} cos\varphi & sin\varphi \\ -sin\varphi & cos\varphi \end{bmatrix} \begin{bmatrix} x \\ y \end{bmatrix}$$

$$x' = x * cos\varphi + y * sin\varphi$$

$$y' = -x * sin\varphi + y * cos\varphi$$

The x and y coordinates of point 6_l have of course been adjusted according to z-$overlap_{outer}$. Using these local coordinates, we can describe the coordinates of point 6 in the coordinate system of Figure B 1:

$$P6_x = r_o * \cos\left(\frac{\pi}{2} - \varphi\right) + P6_{l_x}'$$

$$P6_y = r_o * \sin\left(\frac{\pi}{2} - \varphi\right) + P6_{l_y}'$$

$$P6_z = z_o - \left(\frac{h_m}{2} - zoverlap_{outer}\right) * \cos(tilt_x)$$

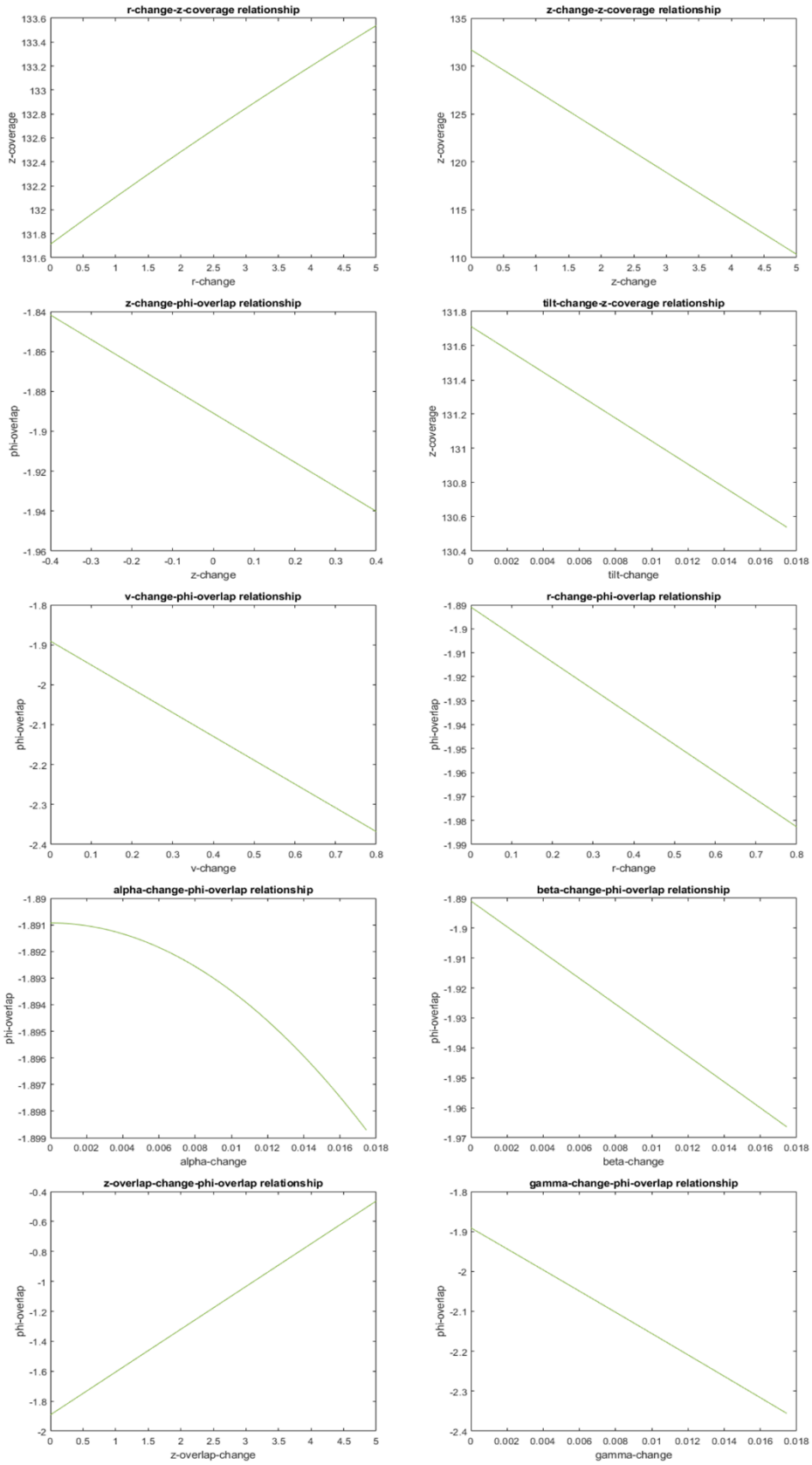

Figure 67. Parameter linearity comparison to results. All correlations seem to behave linearly, except for α change. In principle, this would mean that Pearson's linear correlation coefficient should not be used in case of this parameter, but as we can see from the results, α change has only marginal effect on φ-overlap. Values used for changes are the same as used for sensitivity analysis.